Heat Transfer in Two-Stroke Diesel Engines for Large Ship Propulsion

Christiansen, Caspar Ask; Schramm, Jesper

Publication date:
2012

Document Version
Publisher's PDF, also known as Version of record

Heat Transfer in Two-Stroke Diesel Engines for Large Ship Propulsion

by
Caspar Ask Christiansen

Ph. D. Thesis

Department of Mechanical Engineering
Technical University of Denmark
DK-2800 Kgs. Lyngby
Denmark

Kgs. Lyngby May 2012

Preface

This PhD dissertation is submitted in partial fulfillment of the requirement for obtaining the degree of Doctor of Philosophy in Mechanical Engineering. The work was carried out in the period from April 2007 to November 2010 at the Technical University of Denmark in Department of Mechanical Engineering and supervised by Associate Professor Jesper Schramm. The PhD project was funded by the Technical University of Denmark, Institute of Mechanical Technology, the research school DCAMM and MAN Diesel & Turbo SE.

I would like to thank my supervisor Associate Professor Jesper Schramm and Stefan Mayer (head of basic research at MAN Diesel & Turbo SE) for support and valuable discussions throughout the study. Also, special thanks go to my good friend and fellow PhD student Michael Vincent Jensen for fruitful discussions on both general engine concepts and heat transfer and for keeping the spirits high at all times. Furthermore, thanks go to Hanne Hostrup Poulsen and Frank Jensen (MAN Diesel & Turbo SE) for help and support regarding engine experiments at the MAN Diesel & Turbo SE test site and Claus Suldrup Nielsen (DTU), Volker Wichmann and Dr. Jürgen Nocke (Lehrstuhl für Technische Thermodynamik, Uni. Rostock) for valuable help with the construction of electronics for the experiments and design and fabrication of special thermocouples, respectively. Lastly, I would like to thank Dr. Lyle M. Pickett for being a great mentor during my research stay at Sandia National Laboratories in California, USA, and all my colleagues at the Fluid Mechanics section and Energy Engineering section (DTU) and the people at basic research at MAN Diesel & Turbo SE.

Summary

Demands on reducing the fuel consumption and harmful emissions from the compression ignition engines (diesel engines) have been continuously increasing in recent years. To comply with this, better modeling tools for the diesel combustion process are desired from the engine developers. A very important aspect is determining the temperature distributions in and around the combustion chamber since they are important for determining the boundary conditions of the detailed computer models of the chemical and physical processes in the engine cylinder. Furthermore, the temperature information is very useful for validation of engine simulations.

In this work, a special designed thermocouple is used to measure surface temperatures. The design and fabrication of the special thermocouple is described, along with response tests and uncertainty estimates. A series of experiments at part load conditions (25%, 30% and 50% load) was performed on a MAN Diesel & Turbo SE test engine, which shows very promising results for further investigations of dynamic temperature and heat flux in large bore engines. Instantaneous heat flux is derived using both an analytical and a numerical model and compared. More specifically, the analytical method is based on a one-dimensional assumption and utilizes Fourier series. A 1-D numerical model based on finite differences in a Crank Nicholson time scheme is also used. The magnitude of the perturbations of the

temperature fields around the location of the thermocouples was investigated by computer simulations using a 3-D numerical finite volume model made in STAR-CD.

General trends are observed from the temperature measurements in the limited part load range. These include among others: local increase in mean surface temperature and mean surface heat flux with increasing load, increase in peak surface heat flux with decreasing load and possible indication of an increase in wall deposit layer thickness with increasing load.

Resumé (Summary in Danish)

Krav om at nedbringe brændstof forbrug og sundhedsskadelige emissioner fra forbrændingsmotorer har været støt stigende i de seneste år. For at imødegå disse krav, er det ønskværdigt for motorproducenterne at have forbedrede modeleringsværktøjer for dieselforbrændingsprocesserne. Et meget vigtigt aspekt i denne sammenhæng er, at bestemme temperaturfordelinger i og omkring forbrændingskammeret, eftersom de er yderst vigtige for at kunne bestemme grænsebetingelser i de detaljerede computermodeller af de kemiske og fysiske processer i forbrændingskammeret. Ydermere er denne information om temperaturfordelingen meget brugbar til validering af motorsimuleringer.

I dette studie blev anvendt en specielt designet temperaturføler til at måle dynamiske overfladetemperaturer. Design og fabrikation af det specielle termoelement er beskrevet, samt responstests og usikkerhedsestimater. En række eksperimenter blev udført ved del-last (25%, 30% and 50% last) i en MAN Diesel & Turbo SE forsøgsmotor og viser lovende resultater for videre undersøgelser af temperaturforholdene og varmeflux i store to-takts dieselmotorer. Varmeflux blev beregnet ved brug af både en analytisk og en numerisk metode og resultaterne blev efterfølgende sammenlignet. Mere specifikt kan nævnes, at den analytiske metode er baseret på en 1-D antagelse og benytter Fourierrækker til at løse varmetransportligningerne. En numerisk 1-D model baseret på ”finite differences” i

en Crank Nicholson tidsbeskrivelse blev også anvendt. Størrelsen af pertuberingerne af temperaturfelterne omkring placeringen af termoelementerne blev undersøgt ved brug af en numerisk 3-D beregningsmodel i STAR-CD.

Generelle trends er observeret fra temperaturmålingerne i det begrænsede del-last område. Disse indbefatter blandt andre: lokal stigning i middeltemperatur og middel overflade varmeflux som følge af en stigning i last, stigning i maximal varmeflux som følge af aftagende last og en mulig indikation af stigende tykkelse af aflejringer på overfladen som følge af en stigning i last.

Table of Contents

Nomenclature

Symbols:

ρ	density	$\frac{\text{kg}}{m^3}$
c_p	specific heat capacity	$\frac{\text{J}}{\text{kg K}}$
T	temperature	K
k	thermal conductivity	$\frac{\text{W}}{\text{K m}}$
α	thermal diffusivity	$\frac{m^2}{\text{s}}$
t	time	s
τ	characteristic time	s
A_n	fourier series constant	K
B_n	fourier series constant	K
n	summation index	–
N	number of summation terms	–
ω	angular velocity	$\frac{\text{rad}}{\text{s}}$
x_d	distance from surface	m

$\bar{T}_w$	averaged wall temperature	K
$T_b(\Delta x, t)$	bulk temperature	K
κ	ratio of specific heats	-
L_{Au}	thickness of gold layer	m
L_{Cr}	thickness of chromium layer	m
k_{Cr}	thermal conductivity of chromium layer	$\frac{\mathrm{W}}{\mathrm{K\,m}}$
k_{Au}	thermal conductivity of gold layer	$\frac{\mathrm{W}}{\mathrm{K\,m}}$
ΔT	temperature difference	K
TP_s	thermal product	
φ	phase shift	s
t_f	duration of one engine cycle	s

Abbreviations:

1-D	one-dimensional
2-D	two-dimensional
3-D	three-dimensional

ABDC	after bottom dead center
ATDC	after top dead center
BDC	bottom dead center
SOC	start of combustion
SOTR	start of temperature rise
STC	surface thermocouple
TDC	top dead center
VCVD	vacuum chemical deposition chamber

Chapter 1: Introduction

In recent years, the world has witnessed a still increasing focus on environmental issues, especially with regard to CO_2 emissions, but also a variety of other industrial related emissions, causing a potential health threat. In the context of internal combustion engines examples of such hazardous emissions are sulphur oxides (SOx) and nitrous oxides (NOx). Since the vast majority of the worlds goods are transported around the globe by means of large container ships it is clear that these contribute in large part to the total amount of human-caused emissions. Thus, even small improvements in the efficiency and engine operating conditions will have a significant impact on both fuel consumption and emissions.

In year 2008, the Marine Environment Protection Committee revised the limits and regulations for ship emissions, formulated in the so called Marpol Annex VI from 1997 and the associated NOx Technical Code. As a result, tighter regulations on especially SOx, NOx and particulate matter emissions will be effectuated in 2011 and 2016 (see [1] and [2] for more details). This fact, forces the engine manufacturers to develop new engine designs and apply new technologies to meet the requirements in the near future.

So how can these engines, which are already performing very well, be further optimized? Since it is extremely costly to build engines just for test purposes, the

recent year's progress in computer technology and software simulation tools has opened a possibility for simulating and predicting the performance of new engine designs and concepts. However, experimental validation is very important to test new models describing e.g. fluid flows, combustion and heat transfer mechanisms in the engine. An especially important factor in this context is the knowledge of temperature distributions in and around the combustion chamber. Temperature gradients are what drives the heat transfer and play a big role in the reaction kinetics in the gases primarily during and shortly after the combustion. All are factors that affect the engine performance and emission level. In this work, focus is directed towards methods to determine temperature and heat flux near the boundaries of the combustion chamber. This includes both experimental techniques to measure the temperature of the wall and the gases inside the chamber with a very high temporal resolution, and applying analytical and numerical methods to calculate relevant heat transfer.

However, the information available from the literature is very limited on this topic. In fact, no published material on the dynamic surface temperature variations exists for these large engines. The best attempt, so far, has been by the Internal Combustion Engines Lab at ETH in Zurich [3], who has measured the time-varying temperature and heat flux at a distance of 0.2 mm below the surface in an engine air starting valve. The engine was a two-stroke SULZER engine with a bore of 560 mm and a stroke of 1400 mm, which is similar in size to the two-stroke MAN test engine

used in this work (500 mm bore and 2200 mm stroke). Only two load conditions were tested on the SULZER engine, and the whole investigation was of a preliminary nature. However, from the reported tests, it is clear, that a lot of information about the surface temperature is lost when measuring below the surface, since all the rapid fluctuations in temperature are damped significantly, yielding a smooth and slowly varying temperature trace. Capturing these rapid fluctuations is crucial for determining the right peak values of the heat flux, thermal loading of the outer layers of the wall material, getting the true boundary condition information for simulation purposes of the engine chamber, and so on.

Fortunately, there has been significant progress in the automotive industry within the field of heat transfer in recent years. As a result, a lot of valuable information exists in the literature with regard to temperature measurement techniques and data acquisition systems for small engines (see e.g. [4], [5] and [6]). However, since pressures and temperatures often reach higher values in the large engines, it is not obvious if the measuring equipment used in small engine research can withstand the tough thermo physical conditions of the large engines. Furthermore, it is not unlikely that the significantly different timescales, geometry etc. which are influencing the nature of the heat transfer in the large engines can result in some effects not present, or at least of the same importance, as in the small engines.

In this work, a special designed thermocouple is presented for measuring the dynamic surface temperature. The sensor is tested at different part load conditions in a MAN Diesel & Turbo SE test engine (see Figure 1).

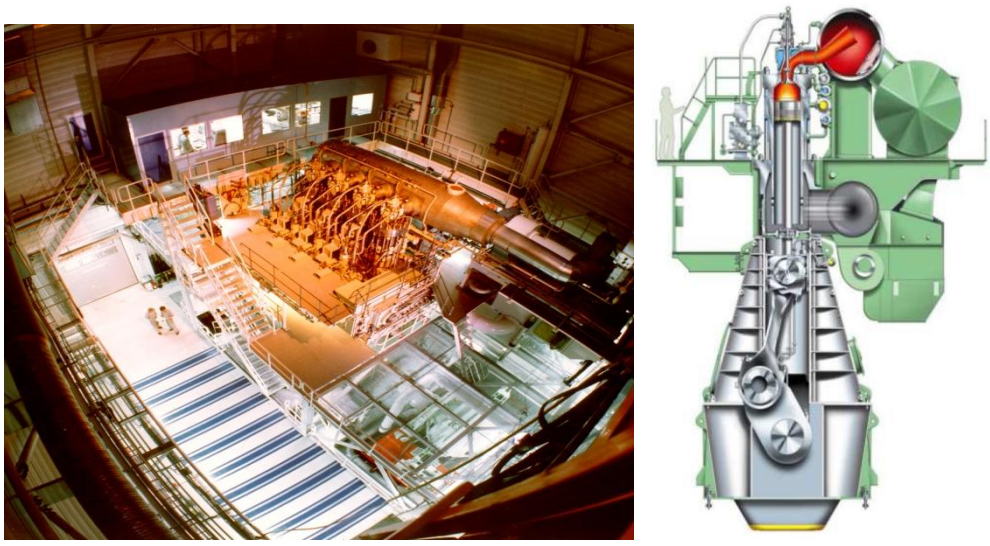

Figure 1: The picture to the left shows the engine test facility at MAN Diesel & Turbo SE. The sketch to the right shows a cross section of a large two stroke diesel engine.

Another part of the work has been to investigate the application of an optical non-intrusive method based on Rayleigh scattering to perform 2-D temperature and density measurements of the gases in a diesel engine type environment. If this method could be further developed and successfully applied to an engine with suitable optical access, it could potentially give a valuable insight to the temperature distribution in the gases close to the walls, including the boundary layers. This method is still in its infancy, but it shows promising results for the application in real engine experiments.

Before diving in to a more detailed review of the literature available on the topic of diesel engine heat transfer and experimental techniques relevant for the work presented in this thesis, the basic principles of the diesel engine work cycle will be briefly explained.

A schematic of the two-stroke diesel engine cycle is shown in Figure 2.

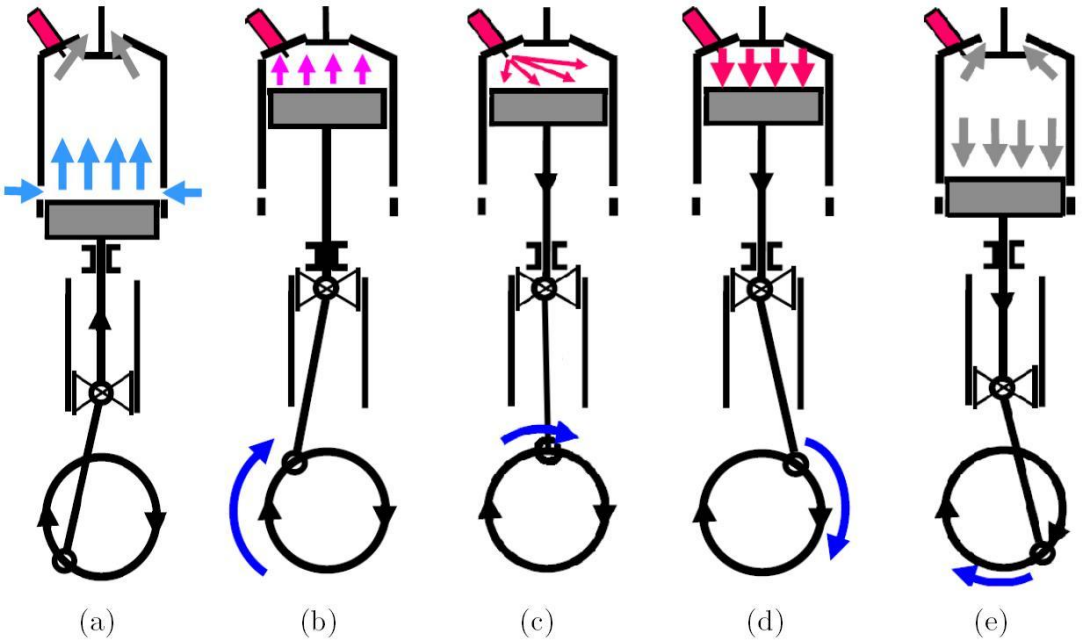

Figure 2: Diesel engine cycle. a) Scavenging b) Compression c) Fuel injection d) Expansion e) Exhaust valve lift [7].

In the first part of the first stroke, the piston top is below the cylinder intake ports, allowing for fresh air to enter the cylinder in a swirling, vortex like motion, and escaping through the open exhaust valve. This step serves both as a scavenging of combustion products from the previous cycle and as an introduction of a fresh oxygen rich and slightly pressurized charge. The charge is then compressed as the

piston is moving from the bottom dead center (BDC) to the top dead center (TDC), resulting in a rapid temperature and pressure rise. When the piston reaches TDC, the fuel is injected into the swirling air in the combustion chamber through several atomizers located in the head of the cylinder. Short after, the fuel atomizes and mixes with the air, which leads to a short premixed combustion followed by a longer period with diffusion driven combustion [8]. As a result of the combustion, heat is released and the temperature and pressure rise fast. This is the period where work is transferred from the piston to the crank shaft. At the end of the expansion phase, when the combustion is finished, the exhaust valve is opened again and a large part of the hot pressurized combustion products leaves the chamber and causes the pressure to drop to almost atmospheric conditions (aka. blowdown).

The entire cycle takes around half a second at normal operating speeds, so it is not hard to imagine that the complexity of the physics and chemistry involved can be very hard to handle from both a numerical and experimental point of view.

Outline of the thesis:

Chapter 1: Introduction and motivation for the work presented in this thesis.

Chapter 2: Literature review of large two-stroke diesel engine heat transfer measurements and relevant temperature measurement techniques.

Chapter 3: Description of the special designed surface thermocouple and the fabrication procedure. It includes response time measurements and uncertainty analysis. Furthermore a description of the equipment and the experimental setups is given.

Chapter 4: A detailed overview of the analytical and numerical methods used for computing temperature and heat transfer from the measurements.

Chapter 5: Results from the measurements of temperature and heat flux performed in the MAN Diesel & Turbo SE test engine.

Chapter 6: Numerical calculations of the perturbed temperature field around thermocouples using a 3D finite volume method.

Chapter 7: Suggestions for future work.

Chapter 8: Conclusions.

Bibliography: Formatted by using the ISO 690 style standard.

Appendix IV and V: During the PhD study several contributions were made to the academic society comprising oral presentations, poster sessions and published papers. Two selected papers can be found in the appendices.

Chapter 2: Literature review

Since the two-stroke Diesel engine was invented by Rudolph Diesel in the year 1892, great efforts have been made to improve engine performance and understand the fundamental processes that influence the engine efficiency. In this context, the field of heat transfer plays a particular important role [9]. This chapter serves as an overview of some relevant findings in the literature concerning local instantaneous temperature and heat flux measurements angled towards large two stroke diesel engines. Both results and measurement techniques will be reviewed. The description of well established heat transfer models that deal with overall engine performance, like e.g. the global thermodynamic models developed by Eichelberg [10], Woschni [11] and Annand [12], is not given here. Instead, instantaneous local temperature and heat flux measurements are the main focus areas.

Temperature and heat flux measurements

Measurements of surface heat flux in small automotive size engines show that surface heat flux values can change rapidly from zero to as high as 10 MW/m^2 and vary a lot from one measurement location to another (see e.g. [9], [13] and [14]). The two curves of measured surface heat flux in a diesel engine head shown in Figure 3 illustrate how the heat transfer can vary significantly between two locations. The test data is obtained from a small automotive size engine and

ensemble averaged over a statistical sufficient amount of cycles [13]. It is also important to note the sharp rise of the heat flux from the time of ignition to around

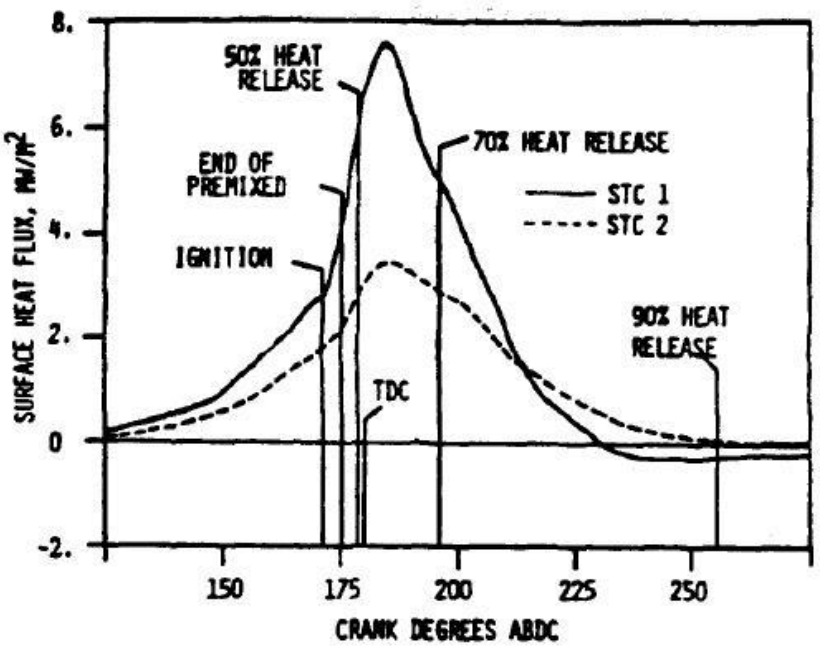

Figure 3: Surface heat flux measured at two different locations (STC1: over piston bowl and STC2: over piston squish area) in a diesel engine head [10].

180 crank angles after bottom dead center (ABDC). This feature stand in contrast to the typical behavior observed in the spark ignited homogenous charge engines where the sharp rise in surface heat flux is not present until the flame passes the measurement location [9],[15]. The most likely explanation for this phenomenon can be found in [16], where it is argued that heat radiation from the diesel flame contribute to the overall heat flux to almost the same extent as convection driven heat transfer. This is not the case for the spark ignited engine where radiation heat

transfer to the combustion chamber walls is small compared to the convection driven heat transfer [8].

While extensive amounts of experimental data are available in the literature for heat transfer in small engines, it is not the case for large two stroke diesel engines used for ship propulsion. In the work by [3], measurements of bulk wall temperature and heat flux are presented for a two stroke Sulzer experimental diesel engine with a bore of 560 mm and a stroke of 1400 mm. The temperature was measured in a special insert mounted in the starting air valve in the engine head at a distance of 0.2 mm below the surface. The time dependent temperature traces are shown in Figure 4 for two different inserts made of titanium and steel respectively, and for two distinct equivalence ratios.

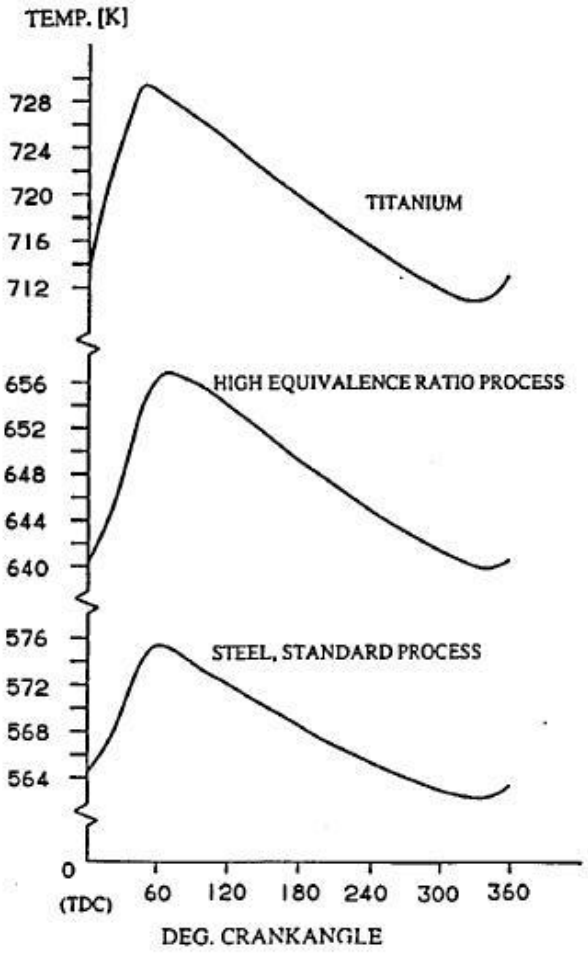

Figure 4: Measured time dependent wall temperatures at 0.2 mm below the surface in a large two stroke diesel engine [3].

Two additional thermocouples were placed at a distance of 7 and 20 mm below the surface such that the steady heat flux component could be deduced. The time dependent heat flux at the surface and 0.2 mm below the surface is shown on Figure 5. From both the temperature and heat flux traces it is clear that some of the dynamic behavior is captured with this measurement method. The peak values are

at the time around 50 CA after TDC during the combustion phase and the lowest values during scavenging and until the start of compression. However, one might expect that a lot of the small time scale temperature fluctuations present in the gas side boundary layer would also be observed in the surface temperature and heat flux values. This is possibly due to the dampening of the small time scale fluctuations translated through 0.2 mm of wall material which subsequently is filtered and smoothed out due to poor signal to noise ratio.

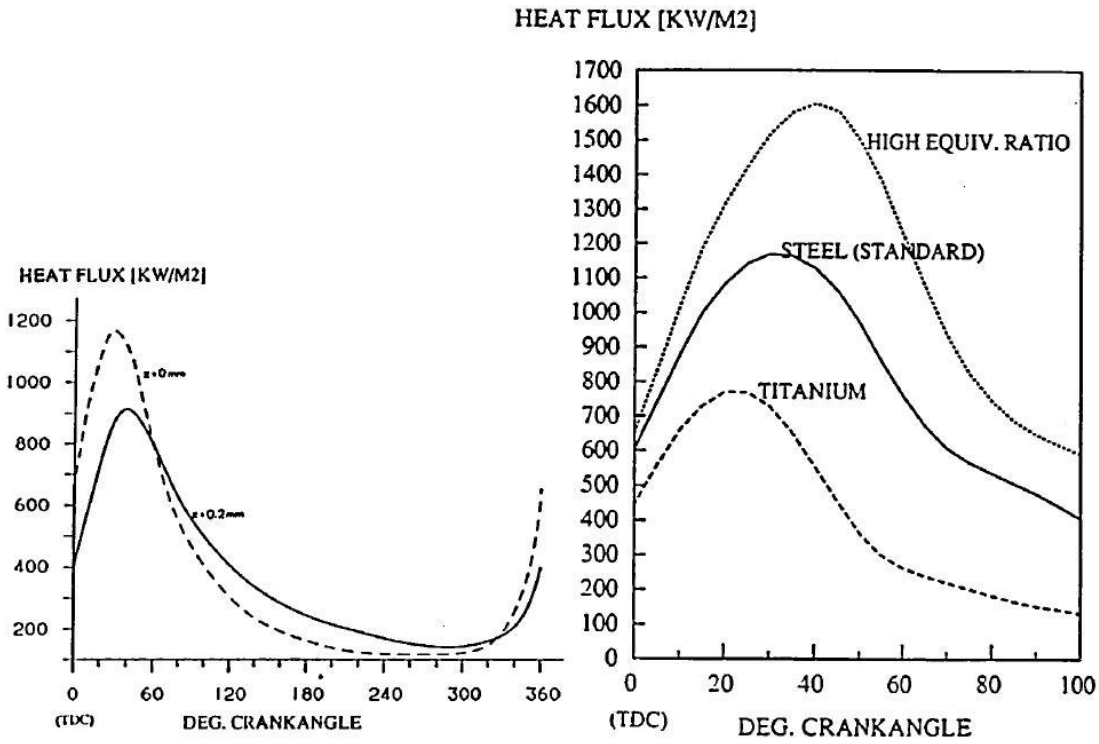

Figure 5: Time dependent heat flux deduced from measured wall temperatures [3]. Left: heat flux data from one entire cycle. The dashed line shows the surface heat flux and the solid line shows the heat flux 0.2 mm below the surface. Right: Surface heat flux for three different cases.

This might lead to wrong predictions of the surface heat flux, especially for periods with high temperature gradients, since the computed heat flux depends strongly on those [17]. Another noteworthy feature of the measured surface heat flux is the absence of negative flux. During the scavenging process where fresh air is used to clear the combustion chamber one might expect a reversal of the flux which is often observed in small engines. On the contrary, the flux stays slightly positive although it tends towards zero.

The results from [3] will be used later on for comparison with the results obtained in this study.

Temperature and heat flux equipment and techniques

A large variety of equipment and techniques exists for the measurement of temperatures and heat flux in all sorts of heat transfer problems. There is not one method that is superior for all types of applications, since each method has its advantages and disadvantages which make them appropriate for a specific application. It is not the aim to describe all existing methods in this section, but to provide an overview of the most relevant with respect to diesel engines.

The different types of methods can be divided into two main categories and four sub-categories [9]:

- Local wall heat transfer
    - Instantaneous surface temperature measurements
    - Bulk temperature measurements
- In-cylinder heat transfer in the working fluid
    - Non-intrusive optical temperature measurements
    - Intrusive temperature measurements

A description of equipment and methods of each category will be given in the following sections.

Instantaneous surface temperature measurements

As seen in the previous section, temperature values can change rapidly at the wall surface. Thus, a fast response, in the order of kHz, is needed to provide sufficient resolution. Moreover, the harsh environment inside the combustion chamber also sets strong limitations on the materials and structural design used for the temperature sensor. Some sensor types are commercially available, but in most cases ad hoc solutions are preferred.

The two most commonly used surface temperature sensors for small engines are the coaxial and pair-wire type thermocouples [9], [14], [18],[12]. All three types utilizes the so-called Seebeck effect [19], where a temperature difference between two connected dissimilar metals induces an electromotive force, which can be read out

as a DC voltage. The connection in one end is called the hot junction, which, in the surface temperature measurement application, is located at the surface of interest. The other connection is called the cold junction and is typically located some distance away from the hot junction where the temperature is well known and steady. The relation between temperature difference and voltage difference is generally non-linear and depends on the material properties and the temperature of the thermocouple wires. The conversion from voltage to temperature is mostly done by either the use of polynomial fits or piecewise linear approximations based on reference data available from both look up tables and online databases [20].

The coaxial and pair-wire type thermocouples have very similar characteristics, with only a minor difference in design. The hot junction are mostly made by vacuum depositing a thin metal film at the surface of interest, thereby establishing electrical contact between the two ends of the thermocouple legs. It is crucial that the size of the hot junction is sufficiently small such that a negligible temperature difference exists across the junction. The depositing of the thin film usually takes place in a vacuum chemical vapor deposition (VCVD) chamber, where the surface is exposed to a gaseous mixture of highly volatile precursors at very low pressure (preferably below 10^{-6} Pa) that will decompose and/or react on the surface at a controllable rate (typically in the order of nm per minute). This thin film technique produces a very strong coating with a low concentration of impurities and a high level of uniformity

[21]. However, not all metals are possible to deposit with the VCVD technique and can require the use of e.g. physical vapor deposition or electroplating [22].

In applications where temperature is measured at a surface subject to significant physical wear, like the contact interface of cylinder liner and piston rings, the µm shallow thin film junction will not last for long. However, the right choice of materials and design allows for the creation of a new hot junction, by means of abrasion, every time the surfaces slide against each other. This method was first demonstrated in an application where the transient inner surface temperature of a gun barrel was measured [23] and later applied to internal combustion engines [24], [25].

In some surface temperature measurements in engines, the entire thermocouple was made by depositing three different thin films directly on the surface on the surface of interest. This technique has the advantage that the thermocouple can be positioned at locations where external wiring access is too limited for other types of thermocouple installations [12]. Furthermore, this method also offers an advantage when measuring surface temperatures at engines with ceramic coatings on the chamber walls. However, the method requires that the entire engine part of should be fitted inside a VCVD chamber during the depositing procedure. This is not always realizable, especially for the large diesel engines, where e.g. the piston crown typically has a diameter between 0.5-1 m. In conclusion, either the coaxial or the pair-wire thermocouples seem to be the best choice for a versatile surface

measurement technique in the large diesel engines. The choice of materials depends on the chemical conditions that the surface will experience and the thermal load. The largest concern in this context is the oxidation of the hot junction and the thermocouple legs. Among the commercially available thermocouple materials, a k-type configuration seems most suitable, since the stable measuring interval is

ANSI Code	Alloy Combination	Maximum Temperature Range	mV Output
B	Platinum/Rhodium	0°C to +1700°C	0 to +12.426
E	Chromel/Constantan	–200°C to +900°C	–8.824 to +68.783
J	Iron/Constantan	0°C to +750°C	0 to +42.283
K	Chromel/Alumel	–200°C to +1250°C	–5.973 to +50.633
N	Nicrosil/Nisil	–270°C to +1300°C	–4.345 to +47.502
R	Platinum/Rhodium Platinum	0°C to +1450°C	0 to +16.741
S	Platinum/Rhodium Platinum	0°C to +1450°C	0 to +14.973
T	Copper/Constantan	–200°C to +350°C	–5.602 to +17.816

Table 1: List of commercially available thermocouple types, including temperature range, composition and voltage output range [52]. The American National Standards Institute (ANSI) code is also given.

approximately 0-1500 K [19],[26]. In a K-type thermocouple the legs are made of approximately 90% Ni and 10% Cr (called Chromel) and 95% Ni, 2% Al, 2% Mn and 1% Si (called Alumel). Other typical combinations of materials are shown in Table 1. Note that the type B and R can measure at even higher temperatures and thus seem as good candidates for high temperature applications. However, this comes with the

price of a lower voltage output which typically is more sensitive to electrical noise, thus increasing the error of the measurement.

The entire fabrication process of the surface thermocouple used in this work will be described in detail in the next chapter.

Bulk temperature measurements

The measurement of temperature below the surface is needed for determining the steady heat flux component through the material of interest. There are two commonly used approaches. The first is simply using a commercially available thermocouple as e.g. the K-type described in the previous section. The thermocouple can be mounted in a hole drilled from the backside of the engine part with a well defined depth [9]. Knowing the precise location of the hot junction is crucial for the determination of the heat flux, since the uncertainty of the distance is directly proportional to the uncertainty of the computed heat flux (See Chapter 4). The two main requirements for this method to work properly, is 1) the one dimensional heat flux assumption should be fulfilled (see Chapter 4) 2) both the surface and bulk thermocouple should not perturb the temperature field.

Another approach to measuring the heat flux through the wall is by the use of heat flux probes which essentially relies on the same principle as simply using two thermocouples. The main difference lies in the design, which typically consists of

two temperature sensors in close contact, embedded in a thermally insulated (only parallel to the heat flow) tube to preserve the one dimensionality of the heat transfer. The heat flux can then be derived from the temperature gradient based on the signal from the two adjacent sensors. However, the distance between the two sensors should ideally be infinitesimal for many of these probes to produce accurate measurements in unsteady high speed flow applications. For some of these probe designs where the two temperature signals can be read out separately, corrections can be made to the data to obtain a more accurate estimate of the transient heat flux. Because of these difficulties in determining unsteady heat transfer, the probes have mostly been used for the measurement of the steady heat flux component ([27],[28]). A second disadvantage of the heat flux probe is the more complex fabrication processes which make the costs exceed the price of the thermocouples significantly.

Non-intrusive optical techniques

Several different optical techniques have been employed in engine research to investigate both microscopic and macroscopic features of the fuel spray structure, gas velocities, temperature distributions etc. (see e.g. review paper [29]). This is a difficult task due to the limited optical access in an engine. Recent activities at MAN Diesel & Turbo SE [30] and Tampere University of Technology in Finland [31] have

proven that it is possible to gain optical access to the combustion chamber of a large two-stroke diesel engine. In the PhD thesis of Hanne Hostrup Poulsen [30], preliminary measurements of the soot temperature are presented. The optical access is gained by installing a sapphire window in a custom made insert placed in the start air valve. An optical method named 2-color pyrometry [32] is then utilized to obtain the 2-D temperature fields of the soot during the combustion. The method belongs to the group of passive techniques where the self illuminative nature of the soot is deployed in contrast to the active techniques where external excitation, typically by the use of a laser, is deployed. Since the latter involves an external source that usually needs a separate optical access and alignment procedure, the active techniques are often more complex to apply than the passive.

2-color pyrometry is a “line by sight” method that records the emission at certain wavelengths in a limited field of view. Since the intensity of the emitted light from the soot particles vary with temperature and concentration, these quantities can be derived from intensity measurements. However, determining the true temperature strictly requires a number of assumptions to be fulfilled. Among these are: the temperature of the surrounding gases must be at the same temperature as the soot particles, the emissivity of the soot is well approximated and the soot cloud must be homogenous along the line of sight. In practice, the error arising from these assumptions is hard to determine and thus care should be taken when drawing conclusions from these kinds of measurements. However, this method can be a

powerful tool when relative temperature rather than absolute temperature is being studied.

Ongoing efforts to expand the level of optical access in the large two-stroke diesel test engine at MAN Diesel & Turbo SE will hopefully soon allow for the application of more types of optical methods for combustion and flow characterization (for more details see the description of the 80 M€ budget Hercules project [33]).

During this PhD study an optical method based on Rayleigh scattering was investigated in detail at the state-of-the-art facilities at Sandia National Laboratories in California under the supervision of Dr. Lyle Pickett. Hence the remainder of this section will give a description of this specific method. The method can be used for high temperature measurements around atmospheric pressure in gases and plasmas from room temperature up to around 10000 K [19]. Extending the pressure range to the peak pressure inside a large two-stroke diesel engine combustion chamber at around 200 bar is theoretically possible but not well documented in the literature. The goal of the measurements carried out at Sandia was partly to assess the potential of this method to be applied to large two-stroke diesel engines with sufficient optical access in the future. For this purpose, the experimental setup sketched in Figure 6 was used. The green beams shows the path of the light pulse generated by the Nd:YAG laser and the direction of the Rayleigh scattered light collected by a CCD camera mounted with a narrow band filter. More details on the

Rayleigh scattering theory and the geometry and technical specifications of the setup can be found in [34] and [35].

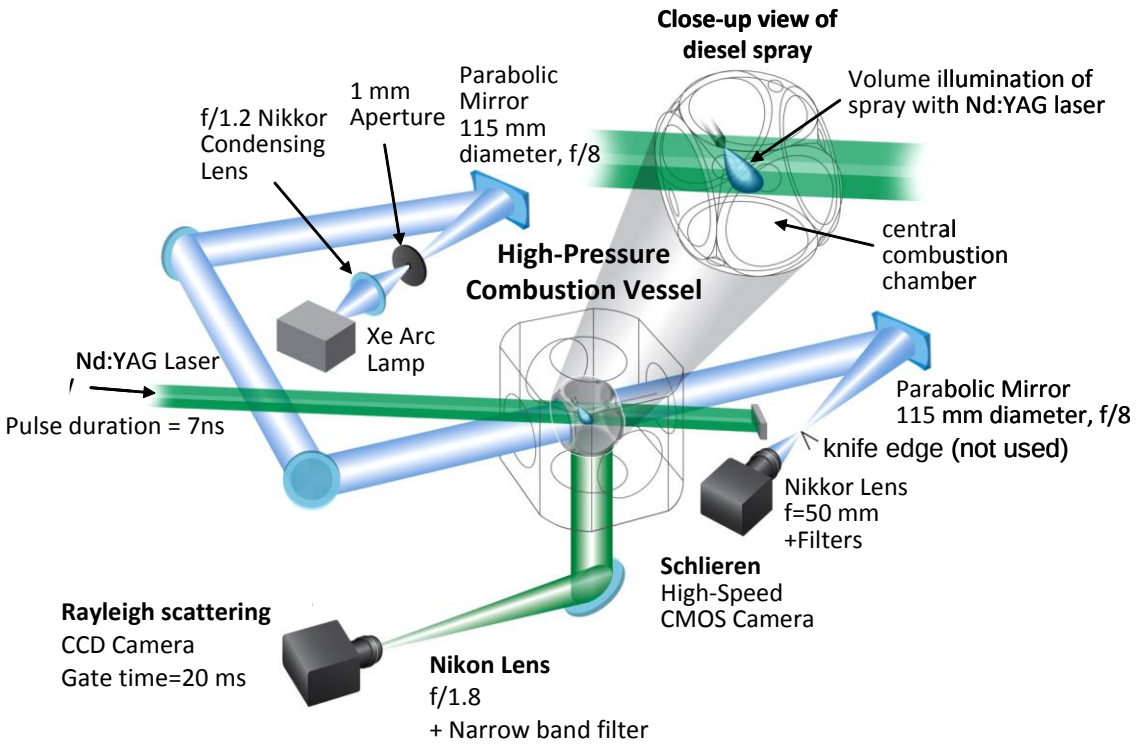

Figure 6: Sketch of optical setup (green beams) for Rayleigh scattering measurements in a diesel engine type environment [36].

A typical image obtained by Rayleigh scattering for a fuel spray in the combustion vessel is shown in Figure 7 (The picture to the right).

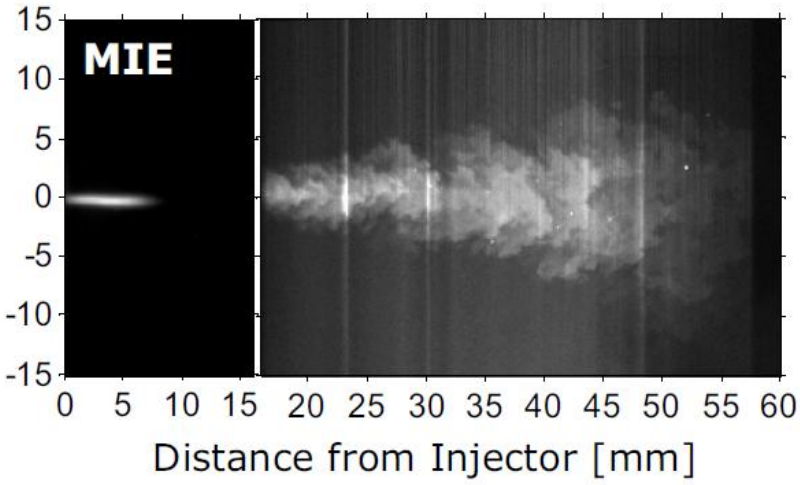

Figure 7: Fuel spray injected into the combustion vessel [35]. Left: Image obtained by MIE scattering[1], showing the liquid part of the fuel jet. Right: Image obtained by Rayleigh scattering showing the vaporized part of the fuel jet.

Since the absolute Rayleigh signal is proportional to the total number density (and the known Rayleigh cross-section and the laser intensity) the temperature can be deduced when the ambient gas and fuel is well characterized ([37] and [34]).

The initial temperature field inside the combustion vessel was measured by a custom made traversable and rotational metal rod mounted with five thin wire thermocouples (R-type) in a series of measurements before the Rayleigh measurements were carried out (see Figure 8). The reason why the Rayleigh scattering measurements and the thermocouple measurements were carried out separately was due to the intrusive nature of the thermocouple technique giving rise to unwanted scattering of laser light by the highly reflective metals.

[1] MIE scattering is the electromagnetic waves scattered by solid spheres with a circumference greater than the wavelength of the incident waves. As opposed to Rayleigh scattering where the wavelength is significantly larger than the size of the spheres [100].

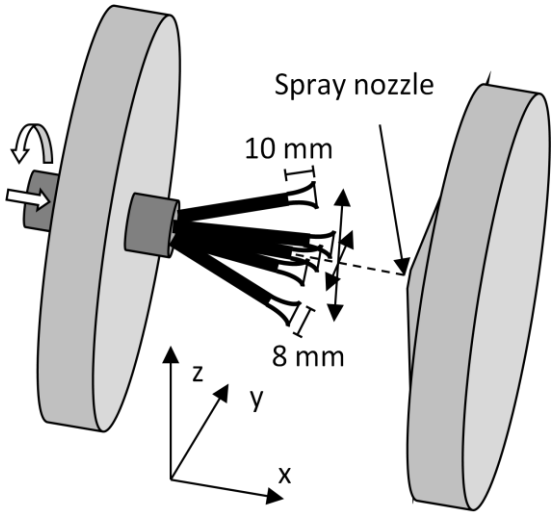

Figure 8: Schematic showing the traversable and rotational thin wire thermocouple probe.

In addition, Rayleigh scattering measurements were carried out in the heated and pressurized combustion vessel without injecting the fuel, showing good agreement with the results obtained from the thermocouple measurements.

In conclusion, the Rayleigh scattering technique seems to be a potential candidate for non-intrusive temperature measurements inside a large-bore engine cylinder of both the spray and the ambient. However, in this preliminary study only pressures up to 60 bar and temperatures up to 900 K were used. The increase of temperature and pressure may introduce new problems and possibly amplify the sources of error that are already present, like e.g. beam steering and birefringence [38].

Chapter 3: Thermocouple probe design, fabrication and preliminary tests

In this chapter we take a close look at the design and fabrication of the special surface thermocouple. A description of response characteristics and sources of error are also given. Furthermore, engine experiments are described in the last part of the chapter.

Thermocouple probe design and fabrication

Instantaneous surface temperature was measured using a special designed K-type thermocouple mounted flush with the surface of a spray atomizer dummy as seen on Figure 9. The spray atomizer dummy differentiates from the original spray atomizer in two aspects: it has no internal channels for fuel delivery (i.e. it is a solid body) and it is cut off flush with the inner surface of the engine head. A second standard K-type thermocouple was mounted 1.5 mm beneath the surface and 2 mm off axis from the fast response thermocouple.

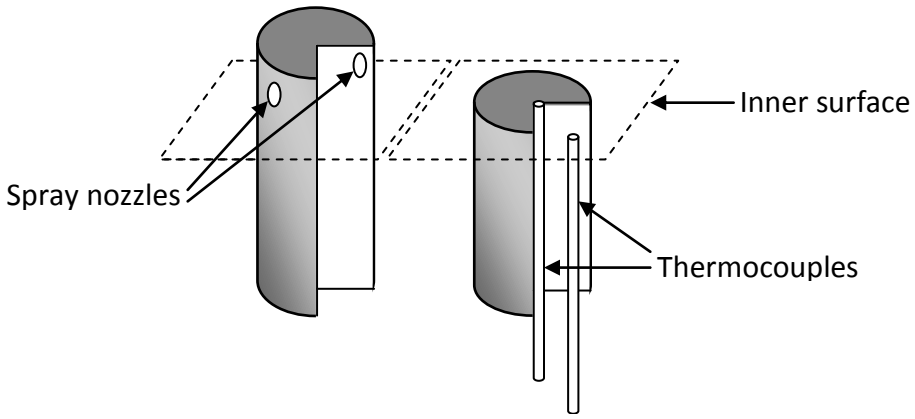

Figure 9: Conceptual sketch showing: Left: the original spray atomizer protruding from the inner surface of the engine head. Right: the modified spray atomizer dummy with two thermocouples mounted in holes drilled from the backside. The atomizer dummy is cut off flush with the inner surface plane.

The location of the atomizer dummy is shown on the sketch in Figure 10 along with a picture of the atomizer dummy removed from the engine head after the experiments had been conducted.

As mentioned in the previous chapter, the idea of measuring instantaneous surface temperatures in a small diesel engine with a modified pair wire thermocouple is not new. However, the description of the design and fabrication of such a thermocouple used for surface temperature measurements in a large two-stroke diesel engine has not been published to this author's knowledge.

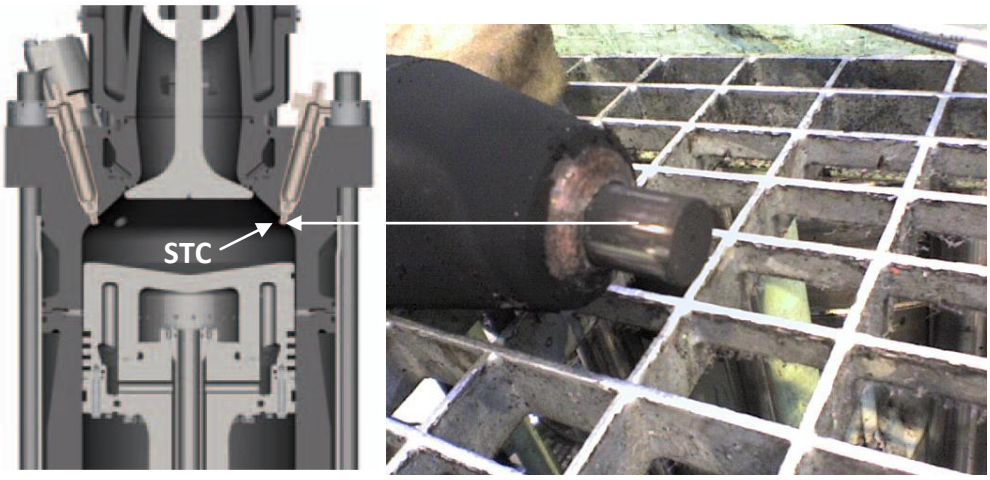

Figure 10: To the left is shown a sketch of the engine cross-section and the location of the surface thermocouple (STC). The picture to the right shows the tip of the (demounted) atomizer dummy after the engine experiments.

The surface thermocouple described in this section was made partly at the workshop facilities at the University of Rostock, and at the workshop facilities at the Technical University of Denmark. The design was discussed thoroughly with Professor, Dr. Jürgen Nocke at the University of Rostock, since his section has successfully applied a similar probe design on small engines in the past.

The surface temperature thermocouple was manufactured using a commercial available K-type thermocouple with a diameter of 1 mm embedded in a modified atomizer without any fuel supply and nozzles. The fabrication steps are shown in Figure 11. First, the thermocouple was pressure fitted in a drilled hole of 1 mm in the atomizer orthogonal to the surface such that the hot junction protruded out from the surface of the atomizer. During operation the thermocouple is held in place due to the thermal expansion of both the Nichrome and the thermocouple materials

as a result of the elevated temperature. In addition a very thin layer of thermally conductive epoxy was applied to the thermocouple and Nichrome interface to provide additional adhesion and fill unwanted air gaps. The hot junction was then cut off and polished until flush with the atomizer surface. The surface was then cleaned and prepared for the depositing of metals to form the new hot junction. First, a 0.5 µm layer of chromium was deposited on the surface using a chemical vacuum deposition chamber. Chromium was chosen since it is adhering excellent to all the materials exposed at the surface, even at high temperatures. Afterwards, a 0.5 µm layer of gold was deposited using the same technique as for the chromium. The gold serves as a protective layer that prevents the chromium from oxidizing, since gold itself is very oxidation resistant at high temperatures. Chromium is deposited since it is has a great bond strength on both oxides (like MgO) and metal (see e.g. [39] reporting bond strength greater than 50 MPa).

The chromium and gold which forms the hot junction has such a small size (low thermal mass) that the temperature difference across the junction is negligible and hence not contributing with any emf to the thermocouple circuit [40].

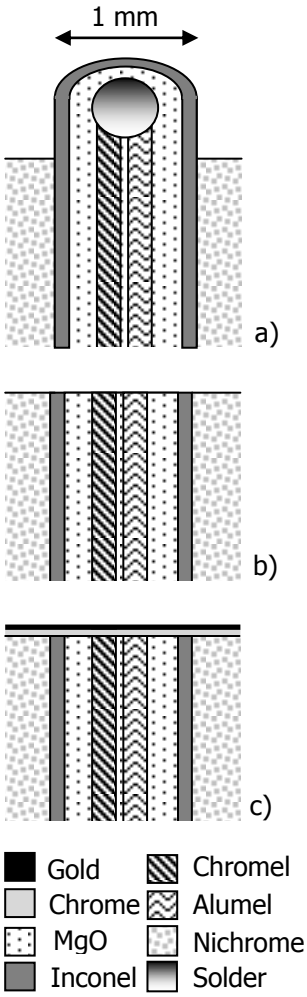

Figure 11: Showing the fabrication steps of the heat transfer probe, a) k-type thermocouple is mounted, b) original hot-junction is cut off, c) Chrome and Gold is deposited to form new hot-junction.

Signal conditioning and data acquisition

Since the voltage output of the thermocouples are in the range of mV, the signal is very sensitive to electrical noise which can easily be of the same magnitude if other non-shielded electrical equipment is present in the surrounding environment. Furthermore, the quality of the signal can be significantly reduced when travelling over long distances, and thus it is preferable to amplify the signal as close to the thermocouple location as possible. The amplification level was chosen such that the output signal from the amplifier would be within an interval of -10 to +10 V which matches the input range of the data acquisition system used for response tests, calibrations and engine measurements.

Both thermocouple signals were amplified using two separate custom made circuits based on an Analog Devices AD597A monolithic instrumentation amplifier with built-in cold junction compensation. The signal amplifier was located less than half a meter from the location of the thermocouples just outside of the cylinder. The purpose build signal conditioner box was placed on a shelf padded with vibration absorbing layers of foam. The connection between the thermocouples and the signal conditioner was done by means of high grade extension wires that were pair-wise spirally wound to reduce the influence of magnetic induction and noise.

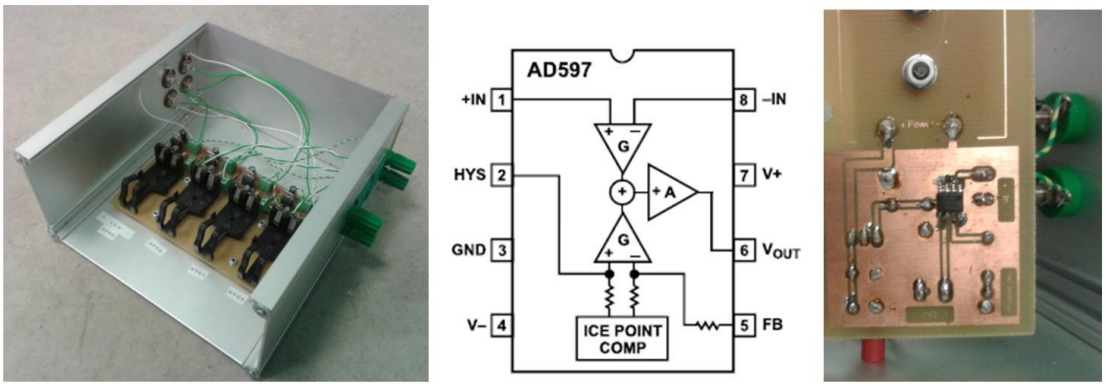

Figure 12: Signal conditioner. Left: Picture of the custom built signal conditioner box with four separate channels (shielded). Middle: Functional block diagram for the AD597A. Right: Picture of the print board with the AD597A connected.

Each circuit was electrically shielded and used each their separate DC voltage source comprised of a 9 Volt battery to reduce noise. The cut-off frequency of the amplifier was 10 kHz, which is sufficient to obtain a high temporal resolution even at the highest rpm values (at least one tenth of a CA which at 123 rpm (full load) equals 0.14 ms). In Figure 12 a picture of the signal conditioner is shown together with the functional block diagram of the AD597A monolithic instrumentation amplifier and a picture of the print board.

In the response tests and the calibration process, a 4-channel NI9215 100 kHz simultaneously sampling module installed in a CDAQ-9172 Compact DAQ chassis was used to sample the output signal from the specially build signal conditioner. The data acquisition was controlled by using Labview v. 8.6.

All data acquisition in the engine tests was controlled using an in-house program made by MAN Diesel & Turbo SE (MAN-DAQ Beta v. 5.04) in Labview that simultaneously sampled data from numerous channels.

Thermocouple response (water droplet test technique)

The response time of the surface temperature thermocouple is of integral importance when determining the true surface temperature. The response time is most often defined as the time it takes for the thermocouple hot junction to reach 63.2% of the true temperature. In this work, the aim is to measure the actual surface temperature of the atomizer dummy but since the thermocouple junction has a finite thickness, the actual temperature registered by the data acquisition system is an average of the total temperature field within the hot junction material (in this case the gold/chromium layer).

However, it can be argued that the hot junction is sufficiently thin to have an almost intrinsic uniform temperature field in equilibrium with the surface/gas interface on the timescale of interest such that the measured value is indeed the true surface temperature. Or in other words, the response time is sufficiently low to resolve surface temperature fluctuations at 10 kHz (corresponding to, at least, a resolution of one tenth of a crank angle degree at full engine speed). A detailed analysis of the impulse response of the hot junction subjected to a change in energy modeled by a step function proves that this assumption is true for our application [41]. In fact, the calculated response time for the extremely thin hot junction is theoretically around a few µs.

The assumption about the uniformity of the temperature field inside the hot junction can readily be estimated by using lumped mass analysis (electrical network analogy) [42].

Considering the two adjacent layers of chromium and gold, forming the hot junction, to be represented by two resistors in a series connection with the resistance given by the ratio of thermal conductivity and layer thickness, and subjected to a constant current represented by a steady heat flux of 1 $\frac{\mathrm{MW}}{\mathrm{m}^2}$ (typical value order of magnitude value for engine surface heat flux), the temperature difference across the thickness of the junction is:

$$\Delta T = q\left(\frac{L_{Au}}{k_{Au}} + \frac{L_{Cr}}{k_{Cr}}\right) = 1 \cdot 10^6 \frac{\mathrm{W}}{\mathrm{m}^2}\left(\frac{0.5 \cdot 10^{-6}\mathrm{m}}{270\frac{\mathrm{W}}{\mathrm{m}\cdot\mathrm{K}}} + \frac{0.5 \cdot 10^{-6}\mathrm{m}}{27.4\frac{\mathrm{W}}{\mathrm{m}\cdot\mathrm{K}}}\right) \approx 0.02\mathrm{K} \quad (0.1)$$

which is clearly negligible in comparison with the overall accuracy of the measurements.

Even though the response time is considered to be sufficient from a theoretical perspective for our application, a series of experiments were conducted to prove the capability of the surface thermocouple to respond fast enough. A previous successfully demonstrated response test called the water droplet test technique [43] was used. It is very similar to the fluid bath plunging technique utilized successfully by e.g.[44] and[45]. Both techniques have the advantage that they are easy to set up and not very expensive in terms of material costs. The water droplet

method is able to prove response times in the order of 0.1 ms, limited by the convective nature of the heat transfer from the fluid to the hot junction of the thermocouple. Other techniques exist for proving even shorter response times, such as shock tube or laser pulse experiments (see e.g. [43] and [46]). However, the water droplet technique is sufficient, since a response time of 0.1 ms will be fast enough to yield the desired temporal resolution.

An illustration of the experimental setup used for the water droplet experiment is shown in Figure 13. A water droplet at room temperature (295.15 K) is created from a nozzle located above the thermocouple hot junction. An insulating plate is separating the droplet and heated hot junction (373.15 K) until the droplet is released from the nozzle. The droplet impacts on the hot junction causing a rapid decrease in surface temperature at the hot junction due to the fast exchange of energy.

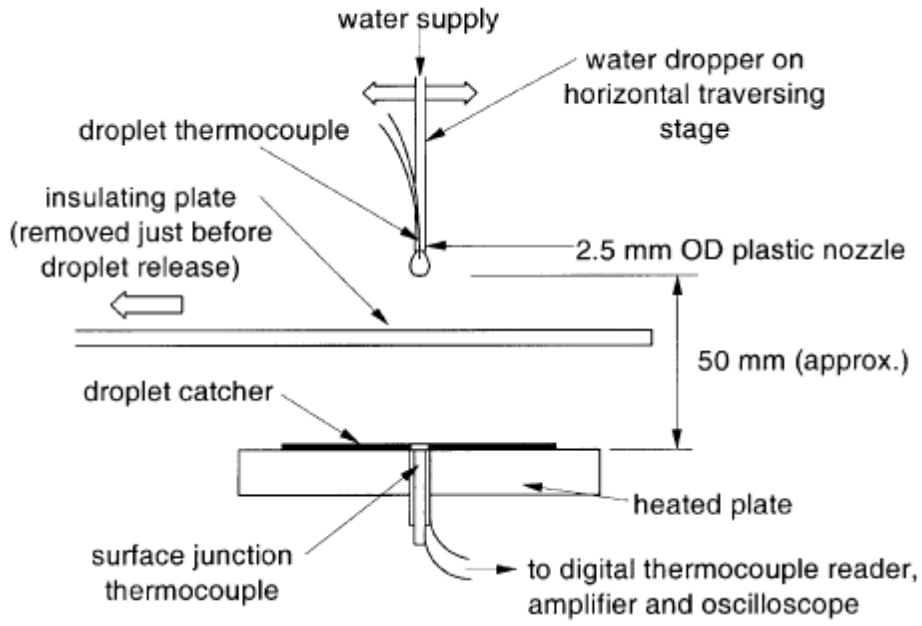

Figure 13: Water droplet experimental setup [43].

The temperature drop of the thermocouple hot junction due to the impact of the water droplet is shown in Figure 14. The desired response time of just around 0.1 ms is clearly seen. A series of 50 experiments were carried out to confirm repeatability. The result is in agreement with previous studies of similar surface thermocouples designs (see e.g. [43]).

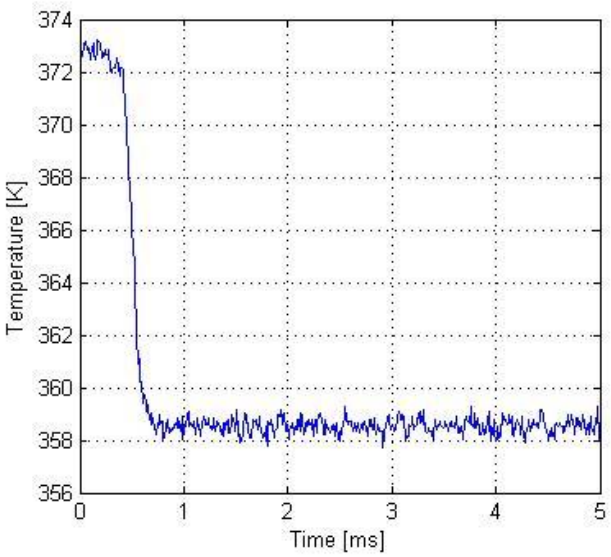

Figure 14: Sensor response using the drop test method

In addition to verifying the fast response time, the method can also be used to determine the so called thermal product, $TP_s = \sqrt{\rho c_p k}$, of the hot junction, which play an important role in the heat transfer analysis (see e.g. eq. (0.15)). The thermal product is related to the measured temperatures in the following way (see [43] and [44]):

$$\frac{T - T_s}{T_w - T_s} = \frac{TP_w}{TP_w + TP_s} \tag{0.2}$$

where T_s is the initial temperature of the thermocouple, T_w is the temperature of the water droplet before impact, T is the temperature of the hot junction after impact, TP_w is the water droplet thermal product and TP_s is the thermal product of the thermocouple hot junction. Unfortunately, the current experimental setup is only able to heat the thermocouple up to 373.15 K which is the upper limit as long

as water is used as impacting liquid. Since the surface temperatures are expected to reach significantly higher values in the engine experiments, there is a need of modifying the setup. The limitation of 373.15 K when using water is due to an assumption in the deduction of eq. (0.2) where the temperature of the water droplet is assumed to be below the boiling point. Thus, if the thermal product has to be determined for higher temperatures, one has to use a liquid with a higher boiling point. Possible non-toxic and cheap candidates could be glycerol or olive oil with boiling points of 563.15 K and 573.15 K respectively. Even higher temperatures could be reached using toxic liquids such as mercury.

Measurement uncertainties

There are many ways to describe the uncertainty related to a certain measurement. A good overview of the different methods is given in [47].

Systematic uncertainties are introduced by e.g. input bias, TC mounting, shunting etc. and can result in offset and non-linearity effects on the measured signal. Often, these uncertainties are constant for the duration of a measurement and can be eliminated if correctly identified. The random uncertainty is sometimes also called the “precision”, and is not a constant source of error like the systematic but a distribution of measurement points around the true value characterized by the standard deviation (see [48], [49] and [50] for more detail). Manufacturers usually

don't state the confidence intervals of the uncertainties for their equipment (e.g. $\pm 2\sigma \sim \pm 95\%$, $\pm 3\sigma \sim 99\%$). Instead they mostly state the uncertainty as a percentage of the full scale value. Thus, a rigorous uncertainty analysis is rarely possible in these cases.

Potential sources of systematic errors are listed below:

- Drift in thermocouples due to changed material properties as a result of annealing and oxidation at elevated temperatures.
- TC connectors can contribute with an uncertainty equal to the temperature difference along the TC connector pins because the material used for the pins is most likely to have a Seebeck coefficient different from the TC wire.
- Low pass filter cutoff effects. There is no such thing as an ideal low pass filter, which means, that attenuation of the input signal will occur at frequencies around the actual low pass frequency value. In practice, this agitates for the use of a low pass filter with a frequency limit sufficiently larger than the highest frequency that should be captured. For this reason, the cutoff frequency was chosen to be 10 kHz (within a 3 dB bandwidth).
- Cold junction errors due to elevated ambient temperature. For the AD597A monolithic integrated circuit the total uncertainty at 303 K (room temperature at the location of the circuit during engine experiments) is 1.1 K [51].

Most of the systematic uncertainties were identified and eliminated by calibrating each channel of the signal amplifier with a reference DC voltage supply that mimicked the thermocouple output signal. These included offset and multiplier errors in the signal conditioner (for more details see [51] and [52]). Furthermore, the output of the modified surface thermocouple and the bulk thermocouple were measured before the engine experiments to make certain that no change was observed after the mounting procedure. This was done by placing the mounted thermocouples in an aluminum cylinder (to ensure temperature uniformity) together with three calibrated (by the ITS-90 standard) K-type thermocouples connected to a separate Fluke temperature calibrator. The recalibration showed good agreement, since the measured temperatures were within the range consistent with the proclaimed tolerances of class one K-type thermocouples of (+/-)1.5 K 300-650 K and (+/-)$0.004 \cdot T$ -1.093 K in the range 650-1200 K.

Due to the weak non-linear nature of the K-type thermocouple output signal as a function of junction temperature a tenth order polynomial fit was used for the conversion of voltage to temperature. The coefficients are available at the homepage of the National Institute of Standards and Technology [20].

No drift was observed during the engine experiments. Application of K-type thermocouples in non-hostile (non-oxidizing) environments are usually not influenced by drift in the temperature range 700 K to 900 K at short hours of operation (see Appendix III). However, the environment in the combustion chamber

is very oxidizing and hence the use of a standard K-type thermocouple would probably be disastrous. The reason why no drift is observed is due to the thin layer of gold at the (exposed) top of the thermocouple shielding it from the gases inside the combustion chamber.

An uncertainty estimate of the distance of the bulk thermocouple from the surface is given by the uncertainty in the measurement precision of the caliper used to measure this distance after drilling the hole. This results in an uncertainty when calculating the heat flux but not in the measured temperature. The uncertainty related to the distance is (+/-) 0.01 mm/1.5 mm ~ (+/-)0.7%.

To summarize, the total uncertainty of the temperature measurement method is strictly a function of the measured temperature. In the temperature range relevant for the STC the total uncertainty is around (+/-)2.3 K.

Engine experiments

The MAN Diesel & Turbo SE test engine is of the type 4T50ME-X which was originally designed and build for ship propulsion but is now solely used for test purposes. It is located at the MAN Diesel & Turbo SE facilities in Copenhagen at Teglholmen. Some selected specifications for the engine is listed in Table 2.

Characteristic	Data
Cycle	Two-stroke
No. of cylinders	4
Bore, [m]	0.50
Stroke, [m]	2.20
Max. power, [MW]	8
Max. speed, [rpm]	123
Max. pressure, [bar]	200

Table 2: Selected specifications for the MAN Diesel test engine [30].

As mentioned earlier in this chapter, the thermocouples were installed in an atomizer dummy which was installed in a fuel injector system without fuel supply. This location was chosen for a number of reasons:

- Easy access when mounting the thermocouples (i.e. short mounting time).
- The small size of the atomizer dummy made it relatively uncomplicated to embed the thermocouples in the existing engine part.
- Presumed high thermal load which would be a good “worst case scenario” test for the STC.
- Easy wiring from the thermocouples to the outside.
- No mechanical surface abrasion that could potentially damage the STC.
- The location was exposed to the working fluid during the entire engine cycle.

The experimental setup is shown on the sketch in Figure 15. The arrows show the direction of the data flow from the thermocouples to the PC.

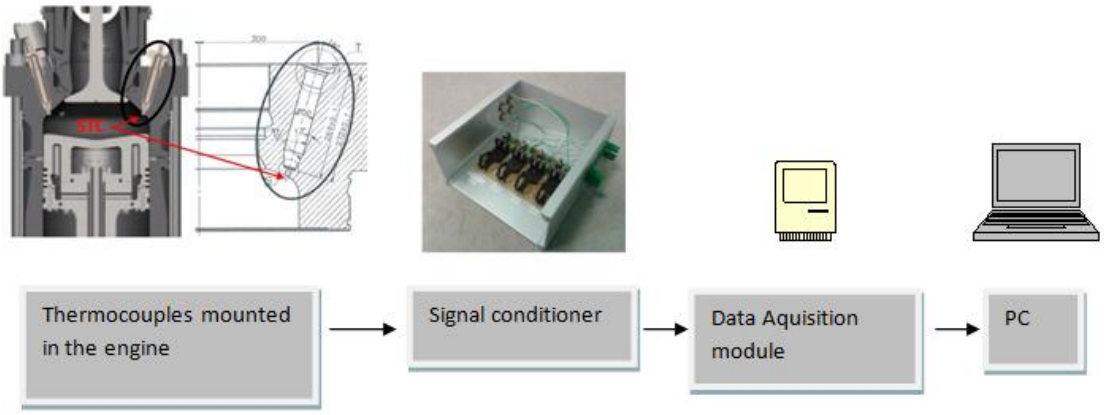

Figure 15: Sketch showing the experimental setup used in the engine tests.

Due to long delays in the fabrication process of the thermocouples and periods of rebuilding of the engine test facilities, only two test series were carried out. In the first test series, the sampled thermocouple signal had a very poor signal to noise ratio due to insufficient shielding of the wiring and signal conditioner circuits. Since no useable data was obtained, the thermocouple robustness was instead tested by long periods of full load operation. No apparent changes were observed in the installation itself. However, a sudden change in signal level was observed after continuous engine operation at full load for several hours, which suggest that the thermocouple was damaged somehow. Later the thermocouple was inspected under a microscope which showed a small lift-off of the hot junction in one end. Since this could easily be caused by a fault in the fabrication process, it was decided

to try with a new one. In the meantime a new improved signal amplifier design based on the existing chipset and circuit boards was constructed and tested in several electrical noisy environments, to resolve the problems with poor signal to noise ratio caused by electrical noise.

In the second and last engine test the new thermocouples were tested at 25% (77 rpm), 30% (82.3 rpm) and 50% (97 rpm) engine loads with a very good signal to noise ratio of approximately 250. In each case, the engine was operated for minimum an hour at constant load to obtain cyclic steady state. Before the first test case, the engine was operated for more than two hours to ensure proper warm up of the engine parts and the ambient.

At the end of the three measurement series the load was increased to 100%. After only a few minutes the STC thermocouple was suddenly ejected out of the atomizer dummy leaving behind only a couple of severely damaged wires. The test naturally stopped at this point.

The reason for this sudden ejection of the thermocouple is probably due to the increase in cylinder pressure at the 100 % load condition. A few suggestions on how to avoid this are given in Chapter 7.

The results obtained in this test are presented and analyzed in Chapter 5.

Chapter 4: Analytical and numerical heat transfer models

In this chapter, two different approaches to calculate the time dependent temperature distributions and heat flux profiles in the combustion chamber wall will be described. The reason why two different models are used is for comparing the results and thereby building confidence in the validity of the results. Furthermore, each model has different advantages. E.g. the analytical model clearly shows how the solution depends on various physical properties while the numerical model can be further developed to include temperature dependent material properties.

The models rely on the knowledge of both surface temperature and at least one temperature trace at a known location in the wall. These temperature traces should have a sufficiently high time resolution and good signal to noise ratio for the models to produce useful results. Moreover, there are a number of assumptions that have to be fulfilled, which will be described when appropriate. A description of the measurement equipment and the technique can be found in Chapter 3.

Since both models are based on the one-dimensional unsteady heat equation a description of the physical problem will be given first. Secondly, a solution method using a Fourier series representation of the known temperature trace to solve the relevant partial differential equation will be described in detail. Finally, a solution to

the same inverse problem will be given, using a numeric approach by applying a Crank Nicolson finite difference scheme. Both models were implemented in Matlab R2008a.

The one-dimensional unsteady heat equation

In this section, a mathematical formulation of the one-dimensional unsteady heat transfer through the cylinder wall is presented. Hence, this part of the heat transfer analysis will be restricted to the heat conduction inside the wall material and not the radiation and convection heat transfer in the interior of the cylinder. To be able to extend this model to include convection and radiation heat transfer from the gas inside the cylinder, one had to gain detailed knowledge of the complex flow fields of the gases inside the engine cylinder along with local thermo physical properties like density, viscosity etc. Such experimental data, or even simulated data, does not exist in the literature for large two stroke diesel engines – at least not to an extend where there is sufficient data to base a full heat transfer model on.

In this approach, the temperature fields within the wall are of primary concern. If these are determined, it is possible to compute derived quantities such as the instantaneous heat flux at the surface and inside the wall. This will be described later. The governing equation for this well known conduction problem (see [42]) is sketched in Figure 16:

$$\frac{\partial}{\partial x}\left(k\frac{\partial T(x,y,z,t)}{\partial x}\right)+\frac{\partial}{\partial y}\left(k\frac{\partial T(x,y,z,t)}{\partial y}\right)+\frac{\partial}{\partial z}\left(k\frac{\partial T(x,y,z,t)}{\partial z}\right) = \rho c_p\frac{\partial T(x,y,z,t)}{\partial t} \quad (0.3)$$

This is the general unsteady conduction heat equation in three spatial coordinates and time for a material with density ρ, specific heat capacity c_p and thermal conductivity k.

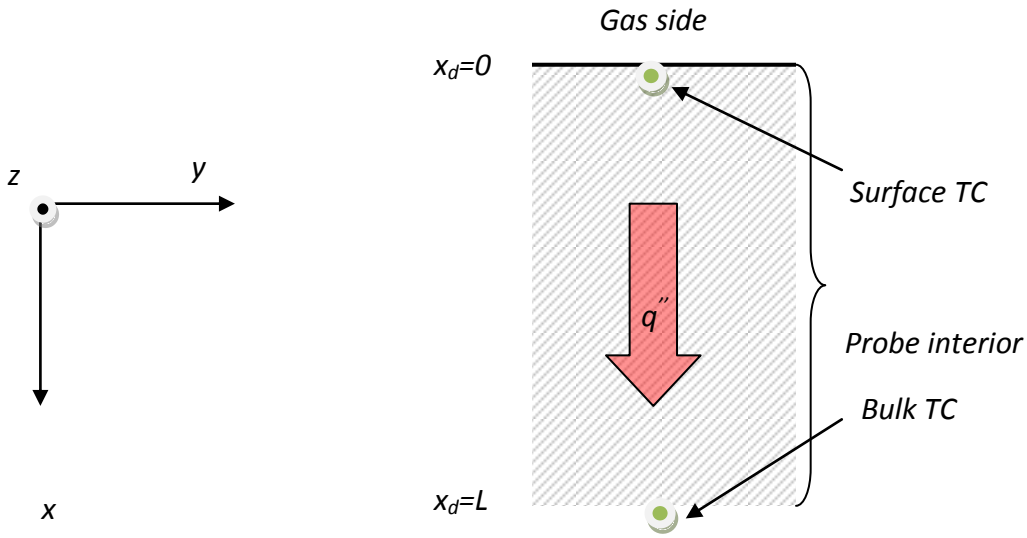

Figure 16: Sketch of the unsteady conduction problem.

Assuming that the heat transfer in the y and z direction is negligible compared to the heat transfer in the x direction the problem can be treated as being one-dimensional in the x-direction (i.e. perpendicular to the surface).

Thus, eq. (0.3) reduces to:

$$\frac{\partial T(x,t)}{\partial t} = \frac{1}{\rho c_p}\frac{\partial}{\partial x}\left(k\frac{\partial T(x,t)}{\partial x}\right) \tag{0.4}$$

Where the domain is given by:

$$0 \leq x \leq L, \;\; t \geq 0 \tag{0.5}$$

Treating the heat conduction as one-dimensional in the x-direction, the possible non-uniformities in the temperature field in the y and z-direction are neglected. This is a fair assumption considering the fact that the two measurement locations (the physical location of the thermocouples) are relatively closely spaced when comparing the timescale of heat conduction with the distance to the heat sources and sinks that are most likely to have an influence on the local temperature field. However, a detailed numerical 3-D model including the entire engine and the surroundings has to be made to properly validate this assumption. Variation in material properties could also affect the temperature field but due to the high degree of material uniformity these are considered negligible (see Chapter 5 for a parameter variation study of material properties).

If the thermal conductivity *k* is assumed to be constant, eq. (0.4) can be rewritten to:

$$\frac{\partial T(x,t)}{\partial t} = \alpha\frac{\partial^2 T(x,t)}{\partial x^2} \qquad 0 \leq x \leq L, \;\; t \geq 0 \tag{0.6}$$

Where α is the thermal diffusivity of the wall material defined as:

$$\alpha = \frac{k}{\rho c_p} \tag{0.7}$$

Solving eq. (0.6) in the given domain requires two known boundary conditions. In this context, one boundary condition (at $x = 0$) is given by the measured surface temperature and the other one (at $x = L$) by the measured bulk temperature as a function of time.

Fourier series method

Due to the time wise periodic nature of the boundary conditions of eq. (0.6) it can be assumed that the solution to eq. (0.6) will be periodic. Hence, one obvious way of representing the solution will be by the use of a series of trigonometric functions that obeys the boundary conditions. In this way, the solution can be formulated in terms of continuous functions even though the boundary conditions are measured data and therefore discrete in nature.

Thus, the boundary condition at $x = 0$ (the surface temperature of the wall) can be represented by the Fourier series [53]:

$$T_w(t) = \bar{T}_w + \sum_{n=1}^{N} [A_n \cos(n\omega t) + \mathrm{B_n} \sin(n\omega t)] \tag{0.8}$$

where $\bar{T}_w$ is the mean wall temperature, A_n and $\mathrm{B_n}$ are Fourier constants and ω is the angular frequency. The Fourier constants are determined by fitting to the measured surface temperature trace. This was done by using the Fast Fourier Transform algorithm in Matlab.

The second boundary condition at $x = L$ is given by the measured bulk temperature T_b. Generally, the bulk temperature should be treated as a function of time when it is measured close to the surface. However, if L is sufficiently large the bulk temperature will be invariant with respect to time. Then an analytical solution to eq. (0.6) can be obtained by using the technique called separation of variables along with a qualified solution guess. In this case, where there is one time dependent boundary condition composed of a Fourier series and one steady state boundary condition, a likely solution to the partial differential equation is expected to be on the form:

$$\begin{aligned} T(x_d, t) = \bar{T}_w - \frac{x_d}{L}(\bar{T}_w - T_b) \\ + \sum_{n=1}^{N} e^{-\varphi_n(x_d)}\left[A_n \cos\left(n\omega t - \varphi_n(x_d)\right)\right. \\ \left. + \mathrm{B_n}\sin\left(n\omega t - \varphi_n(x_d)\right)\right] \end{aligned} \tag{0.9}$$

Where $\varphi_n(x_d)$ is defined as:

$$\varphi_n(x_d) = x_d\sqrt{\frac{n\omega}{2\alpha}} \tag{0.10}$$

By insertion of (0.9) into eq. (0.6) it can be shown that this is indeed a solution to eq. (0.6) which satisfies the boundary conditions.

Note that the first term on the right hand side of eq. (0.9) is time independent but varies as a function of distance from the surface. The second term varies both with the distance from the surface and with time. The magnitude of the temperature fluctuations are attenuated by the exponential function when increasing the distance to the surface. To illustrate the attenuation of the time dependent term one can take a closer look at the exponential function in eq. (0.9) when considering only the fundamental frequency (i.e. for $n = 1$):

$$\chi = e^{-x_d\sqrt{\frac{\omega}{2\alpha}}} \tag{0.11}$$

To get a measure of how long a distance away from the surface is needed for the fluctuations to be negligible when compared to the steady term, a point $x = x_c$ is defined where the exponential function has decreased to 1% of its maximum value:

$$e^{-x_c\sqrt{\frac{\omega}{2\alpha}}} = 0.01 \tag{0.12}$$

Isolating x_c yields:

$$x_c = -\ln(0.01)\sqrt{\frac{\alpha t_f}{\pi}} \approx 0.56\sqrt{\alpha t_f} \tag{0.13}$$

Where t_f is the time it takes to complete one engine cycle ($t_f = \frac{2\pi}{\omega}$). This equation is very useful for different purposes. E.g. if the bulk thermocouple is located at a distance from the surface smaller than x_c it is of integral importance to sample the temperature signal with a sufficiently high frequency or assure that the temperature mean value is correctly obtained by other means. A few sampling points per cycle would give incorrect results.

For a heat conduction problem of this type the heat flux through the surface can be computed using Fourier's law [42]:

$$\left.\frac{\partial q(t)}{\partial t}\right|_{x=0} = -k \left.\frac{\partial T(x,t)}{\partial x}\right|_{x=0} \tag{0.14}$$

Applying Fouriers law by inserting eq. (0.9) into eq. (0.14) an expression for the heat flux through the surface is obtained:

$$\frac{dq(t)}{dt} = \frac{k}{L}(\bar{T}_w - T_b) + k\sum_{n=1}^{N}\sqrt{\frac{n\omega}{2\alpha}}\left[C_n \cos(n\omega t) + D_n \sin(n\omega t)\right] \tag{0.15}$$

Where the constants $C_n = A_n + B_n$ and $D_n = B_n - A_n$.

Of course, it is also possible to find the heat flux at any given distance from the surface by simply performing the differentiation in eq. (0.14) but without setting $x = 0$. However, the maximum heat flux is observed at the surface since the temperature gradients are larger than further away from the surface, and thus the surface heat flux is of great importance when choosing the right materials for the combustion chamber parts (with regard to thermal wear).

An alternative analytical approach to calculate the surface heat flux utilizing Laplace transformation is presented in Appendix I.

Finite Difference model (Crank Nicolson)

In the previous sections it was described how it is possible to calculate both temperature and heat flux analytically when assuming that the boundary conditions and the solution itself can be expressed by using Fourier series. In this section another approach is used to calculate the surface heat flux and the temperature fields inside the wall material. It is still assumed that the problem can be treated as one-dimensional but instead of using a convolution of continuous trigonometric functions to solve the governing partial differential equations the method of finite differences is utilized (see e.g. [54],[55]).

The method is numerical and instead of working with continuous functions the governing partial differential equation is formulated as a discrete approximation. In other words, the solution is only known at a finite number of points in the physical domain. Several numerical methods exist (see e.g. [56]) varying in complexity and with different advantages. For this purpose, the Crank Nicholson scheme is a good choice since it is unconditional stable and offers a better temporal truncation error than other simpler schemes like the “Forward Time Centered Space” and “Backward

Time Centered Space" schemes ([57],[58]) with only slightly more complexity in the implementation procedure.

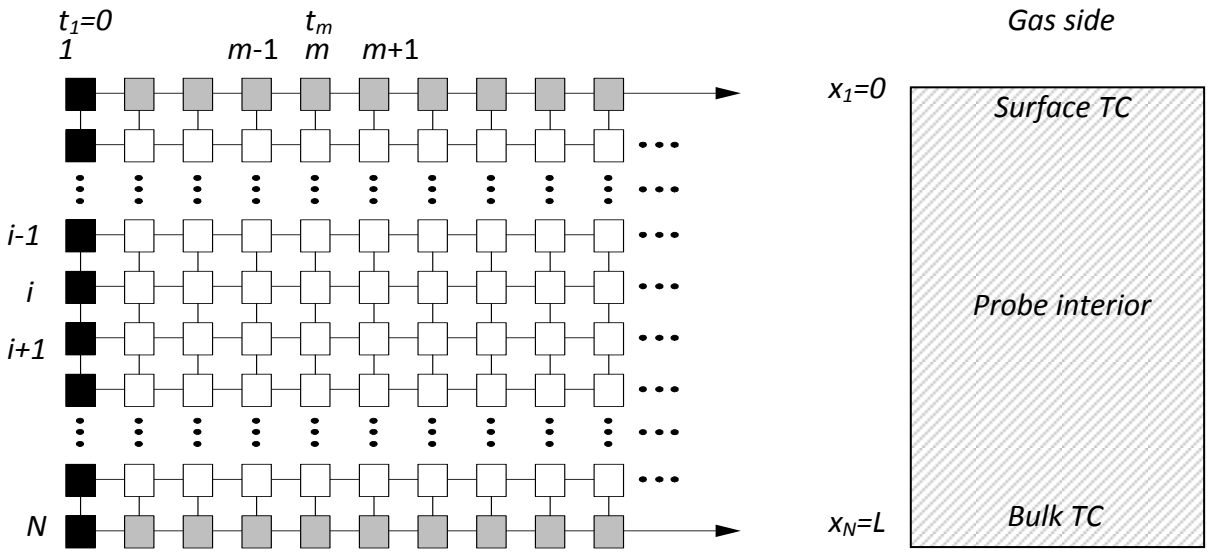

Figure 17: Mesh used to solve the one-dimensional heat conduction equation using the numerical method of finite differences. To the right is shown a sketch of the physical problem in the engine. The black squares in the mesh indicate location of the initial condition, the grey squares indicate the location of the boundary conditions and the white squares indicate the location of the interior points in the wall where the finite difference approximation is computed.

The location of the solution points in the domain are shown in the graphical representation in Figure 17. This type of schematic is called a mesh and the solution points are called nodes. The black squares in the mesh indicate the location of the initial condition, the grey squares indicate the location of the boundary conditions and the white squares indicate the location of the interior points in the wall where

the finite difference approximation is computed. The spatial positions, x_i, are uniformly spaced in the interval $0 \leq x_i \leq L$ such that

$$x_i = (i-1)\Delta x \qquad i = 1,2,\dots N \tag{0.16}$$

where Δx is the local distance between adjacent points in space and *N* is the total number of spatial nodes. The discrete points in time, t_m, are defined in a similar fashion and are uniformly distributed in the interval $0 \leq t_m \leq t_{max}$

$$t_m = (m-1)\Delta t \quad m = 1,2,\dots M \tag{0.17}$$

where Δt is the local distance between two adjacent time steps and *M* is the total number of time steps.

The principal idea of the method of finite differences is to replace the continuous derivatives in the heat equation (Eq. (0.6)) with discrete approximations formulated in terms of the locally known solution values, ϕ_i^m. The Crank Nicholson scheme uses the following approximation for the time derivative called "backward difference" ([59]):

$$\left.\frac{\partial T}{\partial t}\right|_{t_{m+1},x_i} = \frac{\phi_i^m - \phi_i^{m-1}}{\Delta t} + O(\Delta t) \tag{0.18}$$

Where $O(\Delta t)$ is the truncation error which in principal is not known exactly unless the true analytical solution is known. However, the dependence of the user defined parameter Δt on the truncation error can theoretical be shown to decrease linearly with increasing Δt (see e.g. [59] and [60]). Approximating the second order derivate

in space in the heat equation is slightly more complicated. Adding the two Taylor series expansions for ϕ_{i+1} and ϕ_{i-1} defined as:

$$\phi_{i+1} = \phi_i \ + \Delta x \frac{\partial \phi}{\partial x}\bigg|_{x_i} + \frac{\Delta x^2}{2}\frac{\partial^2 \phi}{\partial x^2}\bigg|_{x_i} + \frac{\Delta x^3}{3!}\frac{\partial^3 \phi}{\partial x^3}\bigg|_{x_i} + \cdots \tag{0.19}$$

$$\phi_{i-1} = \phi_i \ - \Delta x \frac{\partial \phi}{\partial x}\bigg|_{x_i} + \frac{\Delta x^2}{2}\frac{\partial^2 \phi}{\partial x^2}\bigg|_{x_i} - \frac{\Delta x^3}{3!}\frac{\partial^3 \phi}{\partial x^3}\bigg|_{x_i} + \cdots \tag{0.20}$$

yields:

$$\phi_{i-1} + \phi_{i+1} = 2\phi_i \ + \Delta x^2 \frac{\partial^2 \phi}{\partial x^2}\bigg|_{x_i} + \frac{2\Delta x^4}{4!}\frac{\partial^4 \phi}{\partial x^4}\bigg|_{x_i} + \cdots \tag{0.21}$$

Solving for the second order derivate gives:

$$\frac{\partial^2 \phi}{\partial x^2}\bigg|_{x_i} = \frac{\phi_{i-1} - 2\phi_i \ + \phi_{i+1}}{\Delta x^2} + \mathrm{O}(\Delta x^2) \tag{0.22}$$

where the left over terms from the Taylor expansions are collected in the $\mathrm{O}(\Delta x^2)$ term which represents the truncation error with a quadratic dependence on the user defined parameter Δx.

Eq. (0.22) is called the "central difference approximation" and is sometimes used directly on this form as a replacement for the second order derivate in the heat equation. However, the model can be improved by simply taking an average of two second order derivatives at two consecutive times (and dropping the truncation error):

$$\frac{\partial^2 \phi}{\partial x^2}\bigg|_{x_i}^{m} = \frac{1}{2}\left[\frac{\phi_{i-1}^{m} - 2\phi_i^{m} + \phi_{i+1}^{m}}{\Delta x^2} + \frac{\phi_{i-1}^{m-1} - 2\phi_i^{m-1} + \phi_{i+1}^{m-1}}{\Delta x^2}\right] \tag{0.23}$$

Inserting eq. (0.18) and eq. (0.23) into the heat equation and rearranging yields the following recurrence formula:

$$-\frac{\alpha}{2\Delta x^2}\phi_{i-1}^{m}+\left(\frac{1}{\Delta t}+\frac{\alpha}{\Delta x^2}\right)\phi_i^m-\frac{\alpha}{2\Delta x^2}\phi_{i+1}^{m}=\frac{1}{\Delta t}\phi_i^{m-1}-\frac{\alpha}{2\Delta x^2}\phi_{i-1}^{m-1}+\left(\frac{1}{\Delta t}+\frac{\alpha}{\Delta x^2}\right)\phi_i^{m-1}-\frac{\alpha}{2\Delta x^2}\phi_{i+1}^{m-1} \quad (0.24)$$

It is evident that the Crank Nicolson scheme is implicit since ϕ_i^m depends on both ϕ_{i-1}^m and ϕ_{i+1}^m. Hence a system of equations needs to be solved. To see the system of equations more clearly we can bring eq. (0.24) on matrix form:

$$\begin{bmatrix} b_1 & c_1 & 0 & 0 & 0 & 0 \\ a_2 & b_2 & c_2 & 0 & 0 & 0 \\ 0 & a_3 & b_3 & c_3 & 0 & 0 \\ 0 & 0 & \ddots & \ddots & \ddots & 0 \\ 0 & 0 & 0 & a_{N-1} & b_{N-1} & c_{N-1} \\ 0 & 0 & 0 & 0 & a_N & b_N \end{bmatrix}\begin{bmatrix} \phi_1 \\ \phi_2 \\ \phi_3 \\ \vdots \\ \phi_{N-1} \\ \phi_N \end{bmatrix}=\begin{bmatrix} d_1 \\ d_2 \\ d_3 \\ \vdots \\ d_{N-1} \\ d_N \end{bmatrix} \quad (0.25)$$

where the coefficients of the interior nodes are defined as:

$$a_i=-\frac{\alpha}{2\Delta x^2}$$

$$b_i=\frac{1}{\Delta t}+\frac{\alpha}{\Delta x^2}$$

$$c_i=-\frac{\alpha}{2\Delta x^2}$$

$$d_i=\frac{\phi_i^{m-1}}{\Delta t}+a_i\phi_{i-1}^{m-1}+(a_i+c_i)\phi_i^{m-1}+c_i\phi_{i+1}^{m-1},\ \ i=2,3,\dots,N-1$$

The truncation error of the Crank Nicolson scheme is $\mathrm{O}(\Delta x^2)+\mathrm{O}(\Delta t^2)$, i.e. the numerical error decreases linearly with a decrease in Δt^2 and Δx^2.

Chapter 5: Engine surface temperature and heat flux measurements

Running experiments on the MAN Diesel & Turbo SE test engine is very expensive due to the high fuel consumption and the amount of required man power to control the engine. The test data presented in this chapter was acquired parallel with the testing of some new engine equipment and hence the amount of experiments was limited.

Measurements at three different engine part load conditions were successfully carried out. The load conditions were 25 %, 30 % and 50 %, corresponding to engine speeds of 77 rpm, 82 rpm and 97 rpm respectively. At these test points, values for the cylinder pressure, and atomizer surface and bulk temperature were recorded trough a common data acquisition interface at a sampling speed of around 3 kHz. At each test point a measurement series consisting of 500 consecutive engine cycles were recorded. This was done in order to obtain an ensemble of the data which is an effective way of minimizing the influence of the noise on the signal and quantifying the amount of random uncertainties by means of statistical data analysis.

The chapter is divided into two parts. The first part contains the surface temperature measurements for the three part load cases. In the second part, the surface heat flux derived from the measured temperatures is presented.

Comparisons of the results obtained using different analytical and numerical calculation schemes are also described.

In the following sections, all values in CA are with respect to TDC (TDC equals 0 CA) unless otherwise stated.

Surface temperature measurements

Surface temperatures were measured for three different engine speed and load situations in the 4T50ME-X test engine.

Due to the turbulent nature of the flow fields of the gases inside the combustion chamber, local instantaneous surface temperature measurements vary from cycle to cycle. However many of the features are generic.

To show the cycle to cycle variation, eight selected temperature traces are shown in Figure 18 to Figure 20 for each engine load case. It is clear that especially after the onset of combustion, shortly after TDC, the difference from cycle to cycle is greatest. Sometimes only one major peak is present and sometimes several peaks with varying heights are observed.

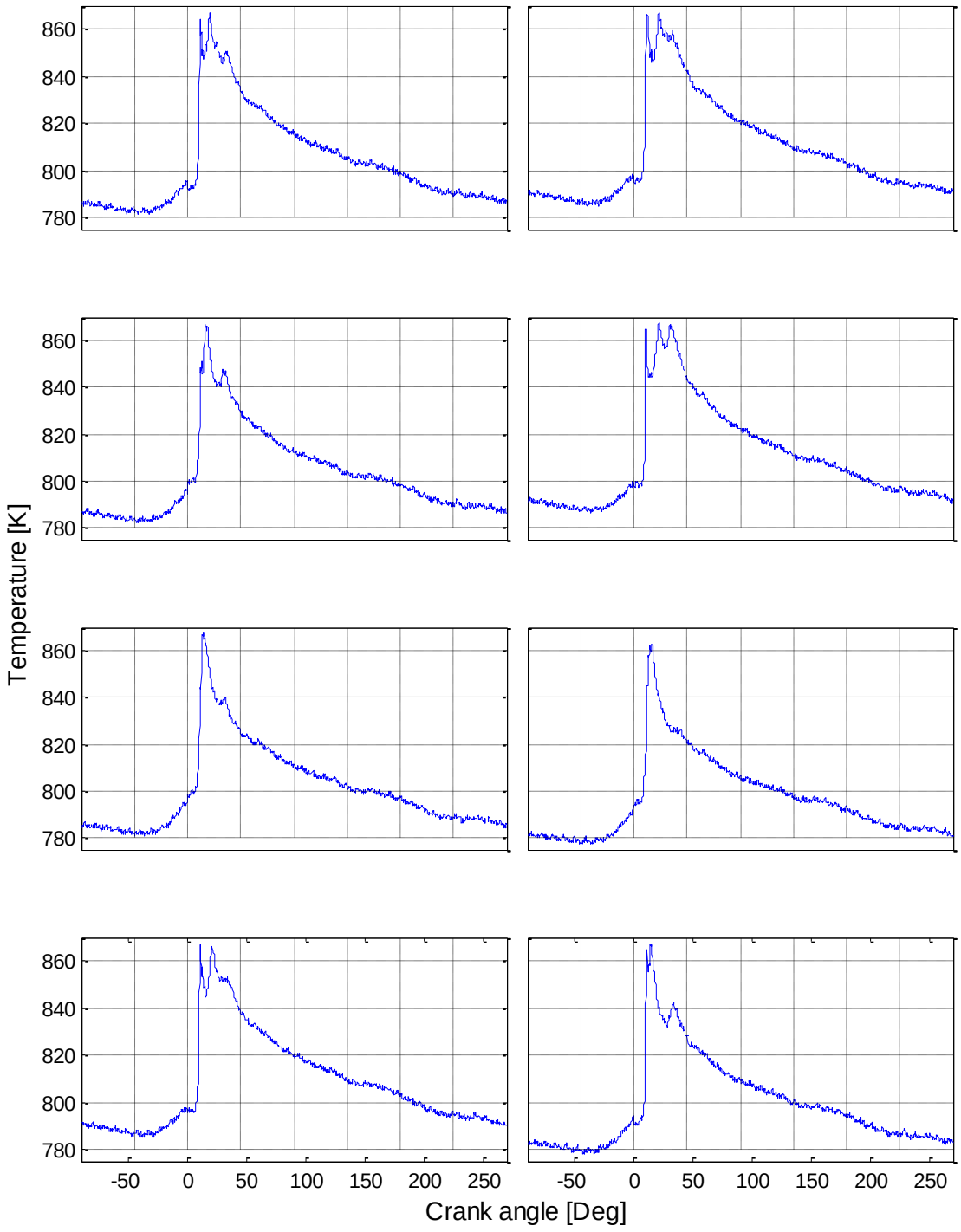

Figure 18: Eight selected surface temperature measurements as a function of CA. The engine load is 25 %. The graphs show some typical cyclic variations in the local surface temperature.

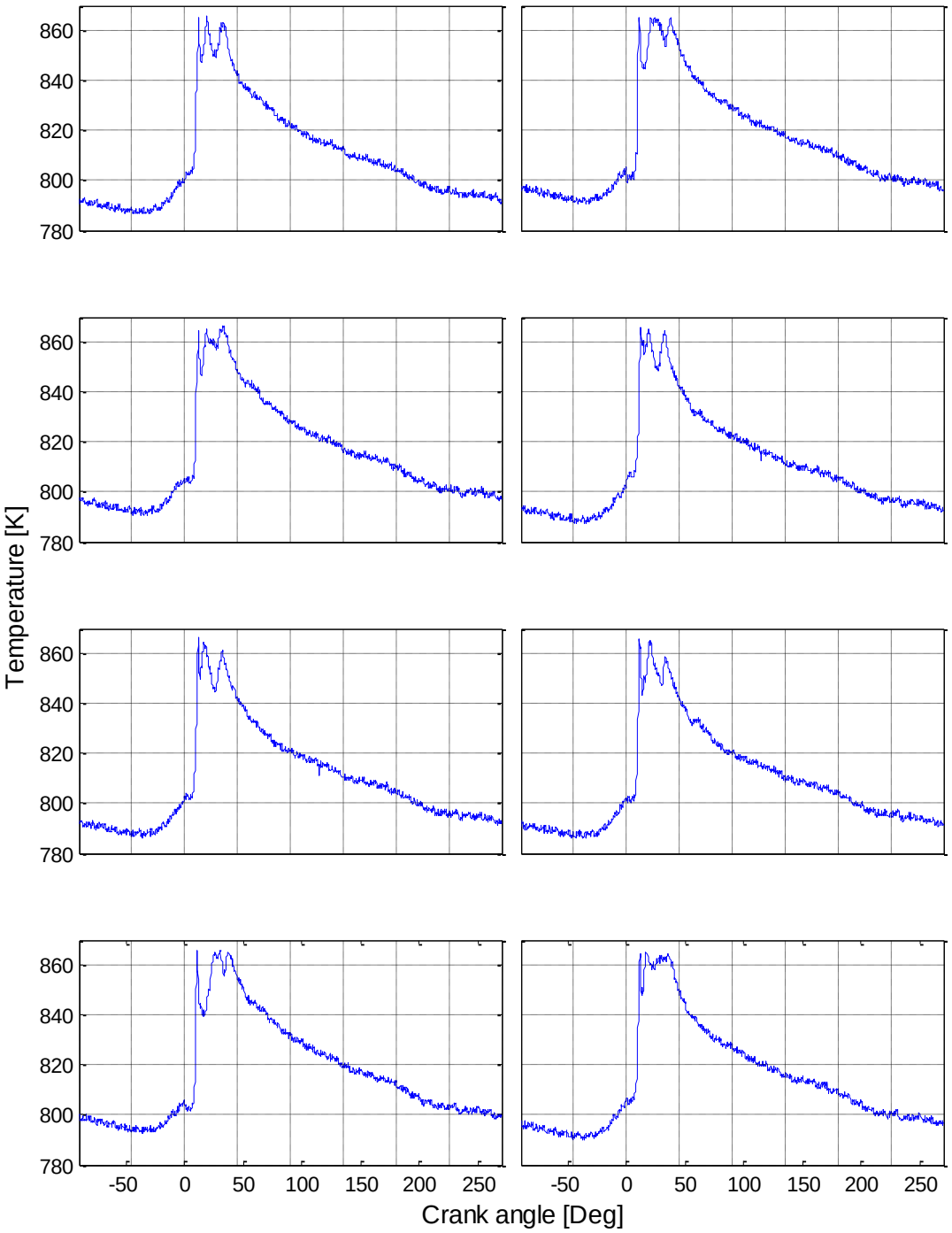

Figure 19: Eight selected surface temperature measurements as a function of CA. The engine load is 30 %. The graphs show some typical cyclic variations in the local surface temperature.

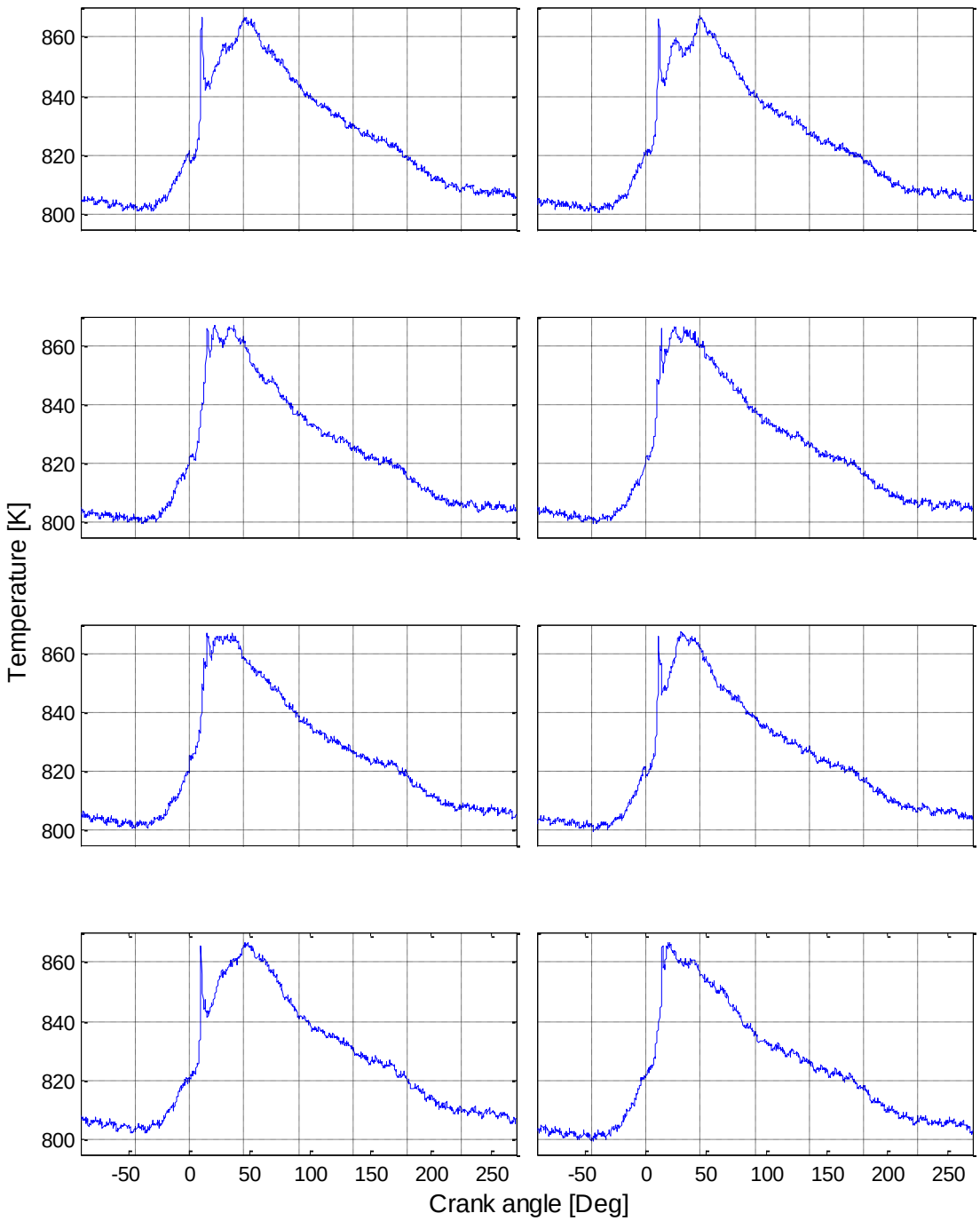

Figure 20: Eight selected surface temperature measurements as a function of CA. The engine load is 50 %. The graphs show some typical cyclic variations in the local surface temperature.

After around 50 CA no major peaks are present in any of the cycles, indicating that the main part of the fuel combustion is over. This agrees well with the measurements done by [30] on the MAN Diesel & Turbo SE test engine, where imaging of the combustion revealed a duration of roughly the same magnitude.

During the expansion (after ended combustion) and the compression part of the cycle, the shapes of the temperature traces are very similar. To make the general features more clear, and to get a representative graph for each load case the ensemble average of 500 cycles have been computed.

These ensemble averages are shown in Figure 21 to Figure 23 along with the respective normalized pressure traces in arbitrary units.

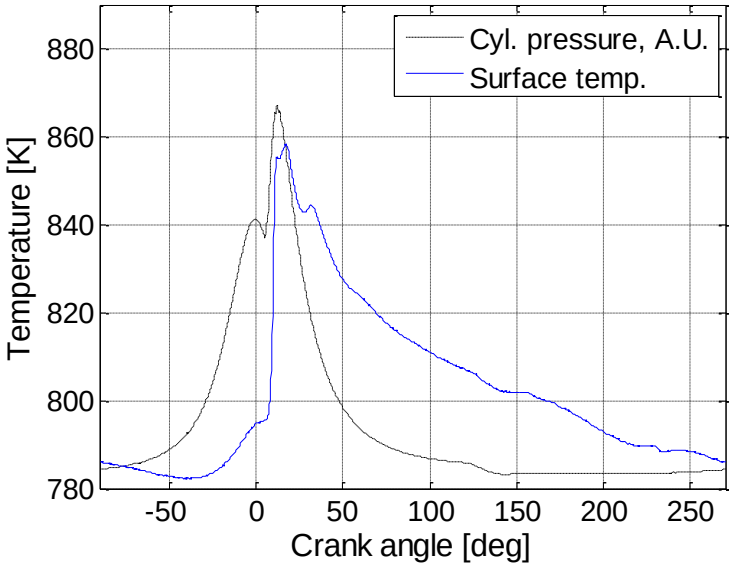

Figure 21: Surface temperature as a function of crank angle at 25 % load and 77 rpm. The dotted line shows the in-cylinder pressure in arbitrary units.

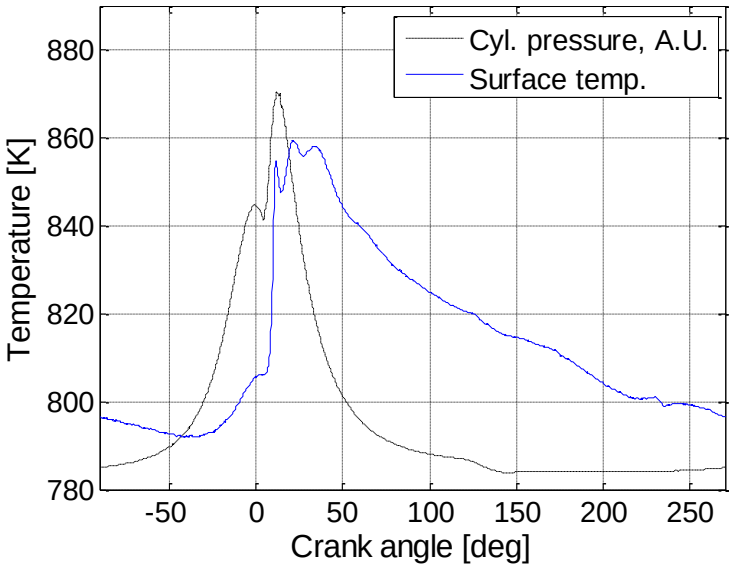

Figure 22: Surface temperature as a function of crank angle at 30 % load and 82 rpm. The dotted line shows the in-cylinder pressure in arbitrary units. TDC is at 0 CA.

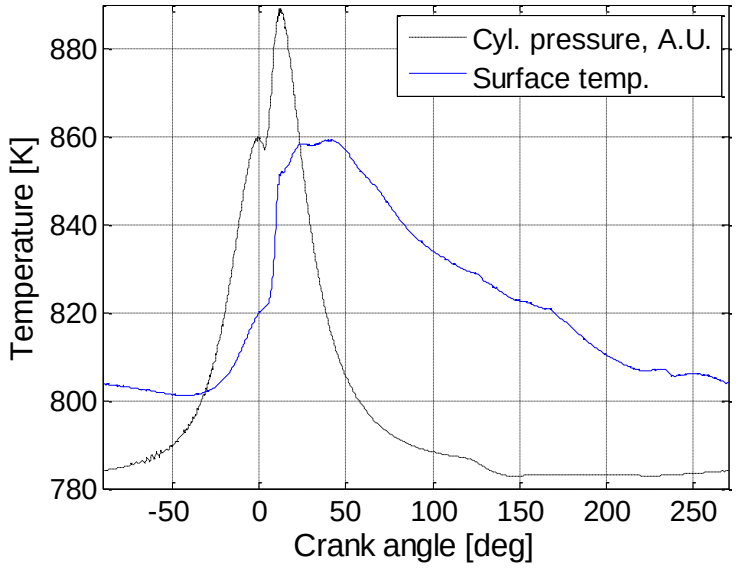

Figure 23: Surface temperature as a function of crank angle at 50 % load and 97 rpm. The dotted line shows the in-cylinder pressure in arbitrary units.

In all three load cases, the pressure and temperature traces are rising during the compression stroke and up until TDC. There is a small delay in the rise of the temperature, since the gases introduced into the chamber during scavenging are still cooler than the surface of the wall in the first part of the compression stroke. Short after the combustion starts, there is a very sharp rise in both the surface temperature and the cylinder pressure. It is interesting to note that the peak temperatures are almost the same in the three cases although peak pressures are significantly higher in the high load case. Unfortunately, the correct absolute values of the pressures were not measured in these tests due to the lack of calibration of the pressure transducer at the time of measurement. Since an increase in pressure

results in an increase of bulk temperature of the in-cylinder gases, one might expect that the peak surface temperature should also increase. Since output values of the signal conditioner was well within the input range of the data acquisition system it is not caused by a limitation of the equipment. This is also supported by the fact that there is a variation in peak temperature from cycle to cycle and no flattening of the temperature signal at the top of the peak. This might suggest that the actual flame, or at least hot combustion products, is arriving at the location of the STC, and that the temperature rise is not only a result of pressure induced increase of the temperature of the gases. In fact at the time of peak temperature the surface temperature might be dominated by the flame temperature. This could explain why there is no significant change in the peak temperature between the three different engine load cases. However, factors like slightly increased flame temperature due increased pressure, longer injection time, faster engine speed and load dependent deposit layer thickness may also influence the peak temperature.

Another interesting feature is the broadening of the temperature peak at increasing loads. Since more fuel is injected in the high load cases, this is to be expected.

During the following cool down of the wall a small bump is seen in the temperature trace immediately after the time of exhaust valve lift around 120 CA (fully opened around 150 CA) for all three load cases. Shortly after, the piston passes the intake ports (around 140 CA) and cool intake air is introduced into the chamber and escapes out of the exhaust valve. The effect of this is not so clear from the figures,

but it seems like the steepness of the temperature trace is slightly increased due to the increased convective cooling effect caused by the swirling intake air.

To further investigate the cycle to cycle variation, a statistical analysis was performed. In Figure 24 the surface temperature traces for each load case is shown along with their respective confidence intervals.

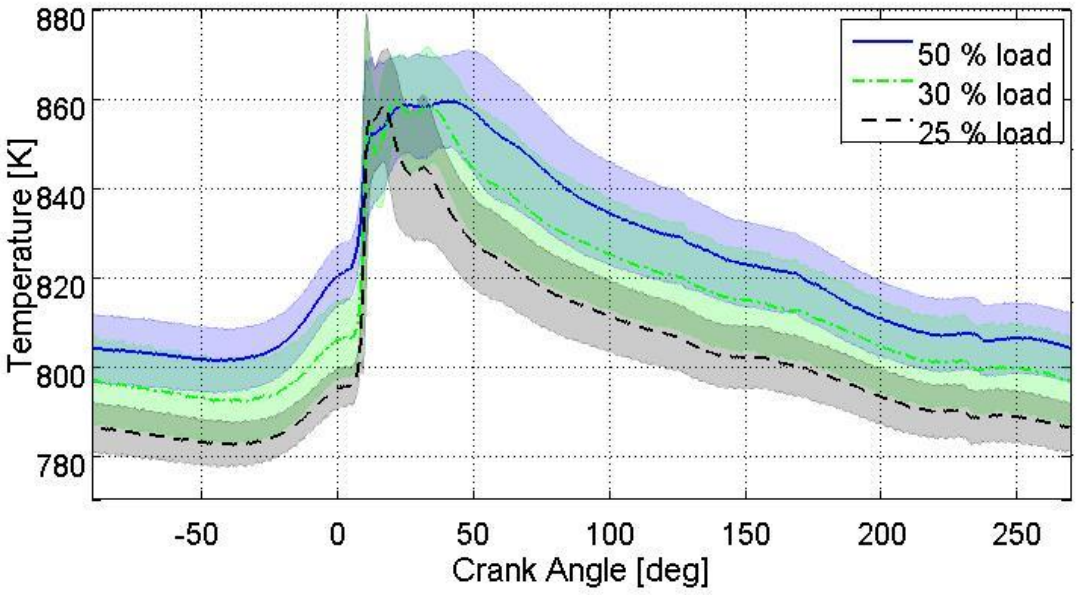

Figure 24: The top plot shows the temperature traces and their respective confidence intervals for three different load situations as a function of CA.

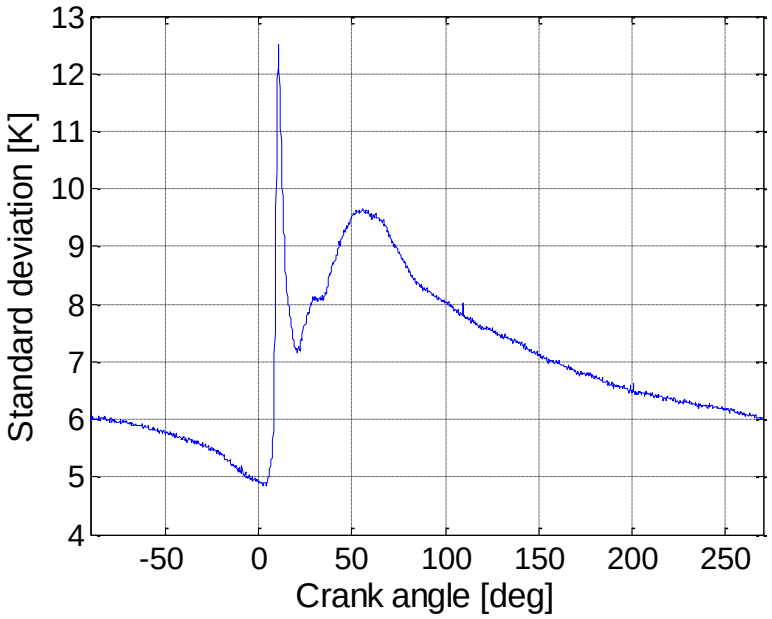

Figure 25: Standard deviation for the 50% load case.

In Figure 25 the standard deviation is shown for the 50% load case.

The 95 % confidence interval is obtained in the following way (see e.g. [61]):

$$Lower\ limit = \bar{T} - Z_{0.95} \cdot \sigma_M \tag{0.26}$$

$$Upper\ limit = \bar{T} + Z_{0.95} \cdot \sigma_M \tag{0.27}$$

Where $\bar{T}$ is the mean temperature, $Z_{0.95}$ is the number of standard deviations extending from the mean of a normal distribution required to contain 95 % of the population and σ_M is the standard deviation. When the amount of sampled data points exceeds around 100 points, the value for $Z_{0.95}$ is 1.96. If the amount of sampled data points were below 100, $Z_{0.95}$ should be estimated using the

leptokurtic “t distribution” rather than the normal distribution used here [61]. However, even though the number of cycles used in the statistical analysis exceeds 100, there could still be non-stochastic effects caused by e.g. thermocouple drift which means that the distribution is not strictly normal.

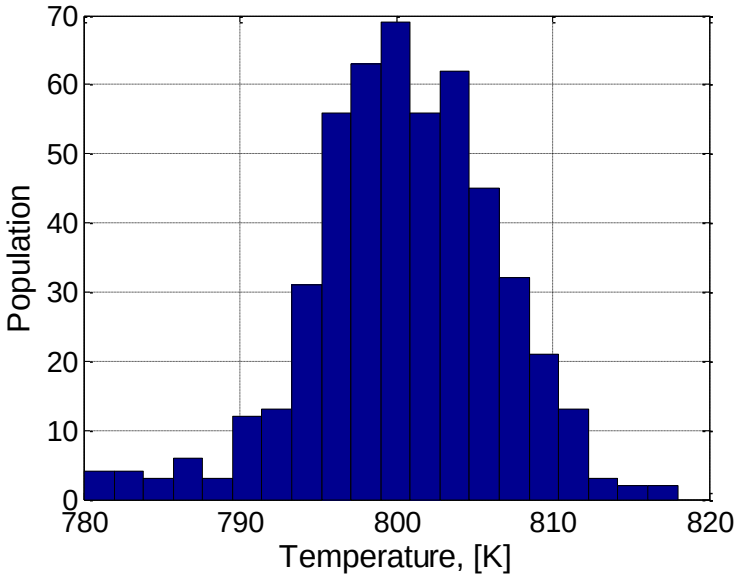

Figure 26: Histogram showing the distribution of temperatures for one selected CA for 500 consecutive cycles.

Thus, the third (skewness) and fourth statistical moments (kurtosis) of the distributions for each CA were evaluated. A typical histogram of the temperature values registered at one specific CA for 500 consecutive cycles is shown in Figure 26. The distribution looks like a normal distribution but with a slight kurtosis.

The kurtosis is a measure of whether the distribution is tall and thin or short and fat, when compared to a normal distribution with equal variance. The kurtosis of the measured data is very close to three, for the most part of the data (excluding the range from start of ignition to end of combustion), which means that there is no significant kurtosis.

The skewness of the measured data is slightly negative, indicating that the distribution has a long tail to the left of the mean (lower values) and the mass of the distribution is concentrated to the right of the mean (higher values). The degree of skewness varies from point to point in the cycle but is always negative and lies for the most part around a value of -0.1 (again excluding the range from start of ignition to end of combustion). This is not a high degree of skewness, but the negative value could suggest that either one or both of the two following effects could be present. If the thermocouple legs were exposed to oxygen at elevated temperatures, either from diffusion through the hot junction, or from cavities in the vicinity of the thermocouple, the characteristics could be slightly altered. For the materials used in the K-type thermocouple this leads to an increase of the Seebeck coefficient, meaning that higher temperature values would be read out compared to the true value. The other possible explanation of a slightly negative kurtosis is the buildup of deposits at the hot junction surface exposed to the working fluid inside the combustion chamber. The increase in deposits results in an increase of the absorbed radiation heat transfer due to the significant difference in emission properties of a

polished gold surface and the deposits. However, while this contributes to an increase in a positive heat transfer to the surface, mainly during the combustion phase, the convective heat transfer will be lowered due to the insulating effect of the deposits [62].

To see if it the negative kurtosis is actually caused by a slight increase in temperature values in time, the temperature at a given CA angle in the cycle is plotted as a function of cycle number. This is shown in Figure 27 along with a graph constructed by the summation of a whole range of CA (i.e. 500 measurement points during expansion) subtracted by an adequate value to bring it down to the same mean value as the single position graph.

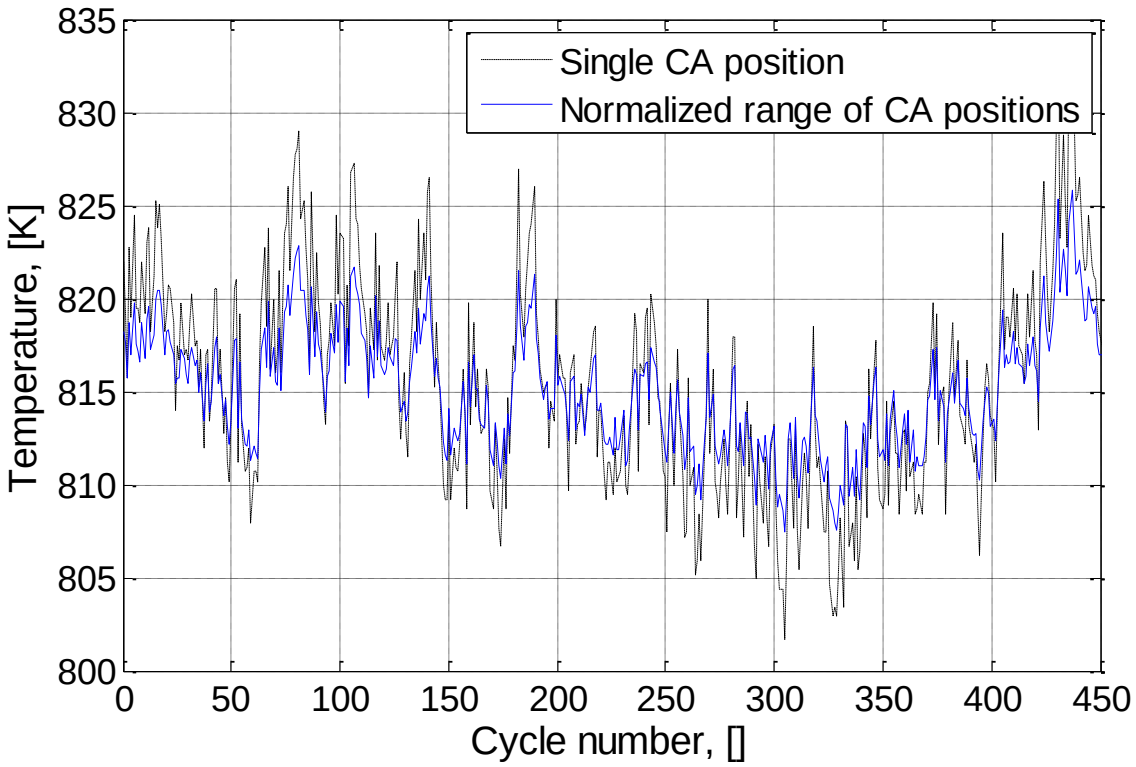

Figure 27: Surface temperature at one given CA as a function of cycle number. Also shown, is a summation of a whole range of CA (i.e. 500 measurement points during expansion) subtracted by an adequate value to bring it down to the same mean value as the single position graph.

The plot shows that there is no apparent drift in the signal during the 450 cycles shown here. Instead it seems as if long period fluctuations are present, presumably due to the aforementioned turbulent nature of the flow field that results in cyclic variations in surface temperature that are carried over from one cycle to the next.

Heat flux calculations

The calculations of the surface heat fluxes were done by using the two different approaches described in Chapter 4. Both methods produced the exact same result, which gives confidence in the validity of the computed fluxes. Both methods were implemented in Matlab. Routines for extracting the measured data and identifying and arranging the data belonging to each cycle for easier data handling, were also programmed in Matlab. Determination of the Fourier coefficients were done by utilizing the Fast Fourier Transform routine implemented in Matlab.

The computed surface heat fluxes are shown in Figure 28 for the three different load cases.

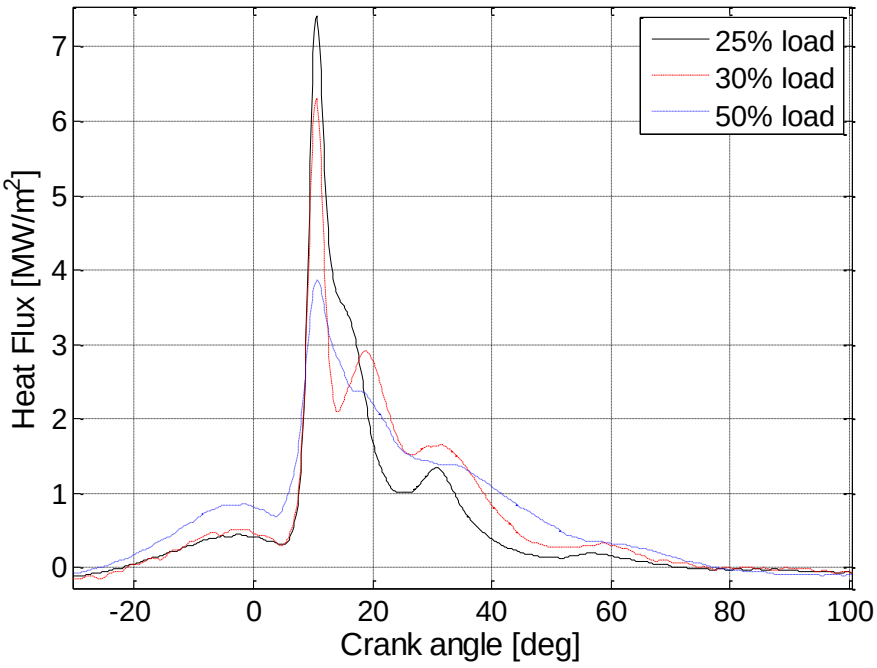

Figure 28: Surface heat flux as a function of CA for three different load cases.

As can be seen on the figure, there are significant differences in the size and shape between the three load cases. The peak heat flux is varying from 3.9 $\frac{\mathrm{MW}}{\mathrm{m}^2}$ (50% load) up to 6.3 $\frac{\mathrm{MW}}{\mathrm{m}^2}$ (30% load) and 7.4 $\frac{\mathrm{MW}}{\mathrm{m}^2}$ (25% load). It is not obvious what can cause this large difference. A possible explanation can be found in the next section regarding the determination of the phase shift and the effect of deposits on the surface of the STC. In brief, the amount of deposits is greater in the high load case and thus acts as a thermally insulating layer which dampens especially the rapid fluctuations. Furthermore, it is worth remembering that the measurements are only carried out at one location in the engine and is thus not necessarily representative for the

general surface heat flux. When the load and speed of the engine is changed it is very likely that flow patterns and the temperature distribution in the hot gases change considerably. This could result in delayed arrival of the flame at the location of the STC and affect the magnitude of the heat transfer from the gases to the STC. A study of these complex phenomena would require detailed optical studies of the flame development and progression throughout the engine cylinder. From the measurements done in this study it is not possible to tell whether the initial surface heat flux rise is caused by radiation, convection or a combination of the two. However, it seems likely that it is a combined effect considering the soot radiation estimates calculated in the last part of this chapter. These estimates show that it is possible to have heat radiation of the same order of magnitude as the convection heat transfer at certain periods in the engine cycle.

A literature survey of surface heat flux measurements in small diesel engines showed that there is generally no certain trend in the peak value as a function of load. The measurements presented in [63] is a good illustration of this, since they showed a peak heat flux of around 3.5 $\frac{\mathrm{MW}}{\mathrm{m}^2}$ at 40% load, 4.3 $\frac{\mathrm{MW}}{\mathrm{m}^2}$ at 80% load and 2.4 $\frac{\mathrm{MW}}{\mathrm{m}^2}$ at 100% load. As mentioned in Chapter 1, the literature is very limited on heat transfer in large two-stroke diesel engines. The only values for instantaneous surface heat flux published (to this author's knowledge) at a diesel engine of comparable size is the one described in [3]. However, the flux is not obtained through surface

measurements but through temperature measurements 0.2 mm beneath the surface. The results are shown in Figure 29.

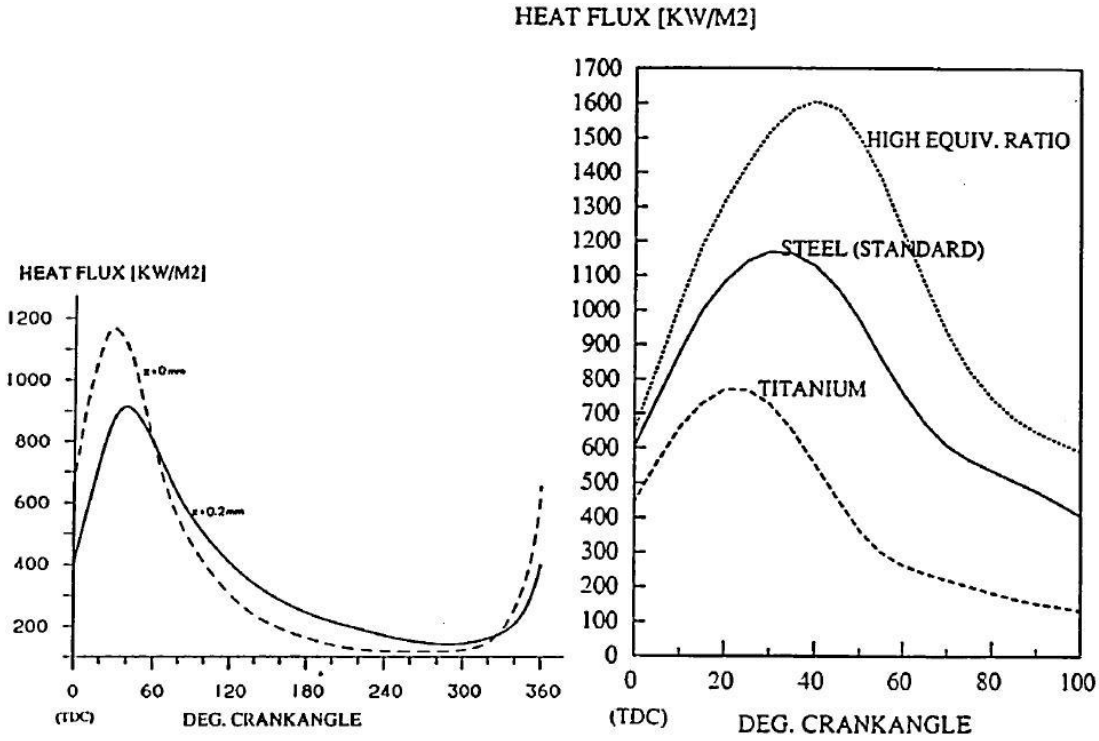

Figure 29: Time dependent heat flux deduced from measured wall temperatures [3]. Left: heat flux data from one entire cycle. The dashed line shows the surface heat flux and the solid line shows the heat flux 0.2 mm below the surface. Right: Surface heat flux for three different cases.

It is clear that the peak values of the surface heat flux are lower than the ones computed for the MAN Diesel & Turbo SE test engine, but within the same order of magnitude. Furthermore, no negative surface heat flux is observed which is in contrast to the results obtained for the MAN Diesel & Turbo SE engine. It seems quite unphysical that there is no negative flux during the scavenging process where

cool air is swirling through the cylinder but once again it is important to remember that these are only local measurements and thus not necessarily representative for the general heat transfer trends. Overall, the heat flux curves look rather smooth which could be explained by the very smooth bulk temperature profiles from which the flux is derived. Probably the results are better to compare with mean surface heat flux values. Those are reported to be: 366 $\frac{\mathrm{kW}}{\mathrm{m}^2}$ (for the steel mount at standard operation), 147 $\frac{\mathrm{kW}}{\mathrm{m}^2}$ (for the titanium mount) and 469 $\frac{\mathrm{kW}}{\mathrm{m}^2}$ (for the steel mount with high equivalence ratio). The mean surface heat flux values for the MAN engine at the location of the STC are: 99 $\frac{\mathrm{kW}}{\mathrm{m}^2}$ (25% load), 105 $\frac{\mathrm{kW}}{\mathrm{m}^2}$ (30% load) and 111 $\frac{\mathrm{kW}}{\mathrm{m}^2}$ (50% load). The relatively low heat flux values for the MAN engine could indicate that the cooling effect of the backside of the atomizer is low. The measured high surface temperature values support this theory since less cooling will result in elevated wall temperatures. Normally, there is a certain cooling effect from the fuel when it is injected through the nozzles. In these test the whole fuel system was demounted from and the backside of the solid atomizer was only cooled by natural convection.

Parameter variation of material properties

The material properties used for the computation of the surface heat fluxes can be found in Appendix II. Since the thermal conductivity and the specific heat capacity are functions of temperature, the assumption made in Chapter 4, with regard to constant material properties are not strictly true in practice. To show the magnitude of the error introduced by this assumption, a parameter study on the influence of the temperature dependent material properties on the surface heat flux was carried out. The material properties used in this study was based on the data presented in appendix II. The maximum, minimum and mean surface heat flux profiles are shown in Figure 30. The error is largest around the peak, where the maximum error is estimated to be 0.1 $\frac{\mathrm{MW}}{\mathrm{m}^2}$.

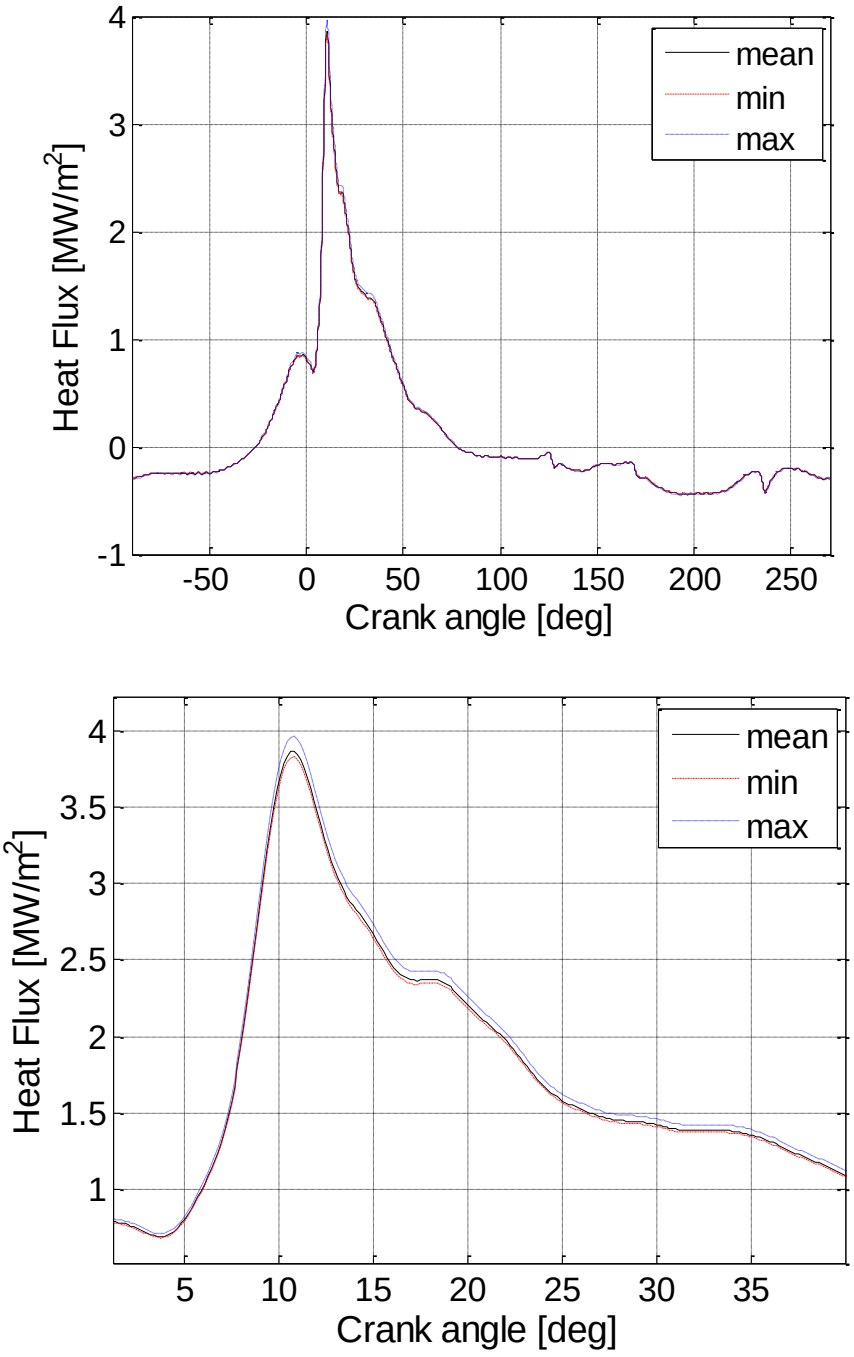

Figure 30: Surface heat flux as a function of CA (at 50% load). The three curves show the minimum, maximum and mean flux obtained from a parameter variation study on the temperature dependent material properties. The top figure shows the entire engine cycle and the bottom figure is a zoom in.

Phase shift due to deposits

In this section the effect of possible deposits on the surface of the STC will be

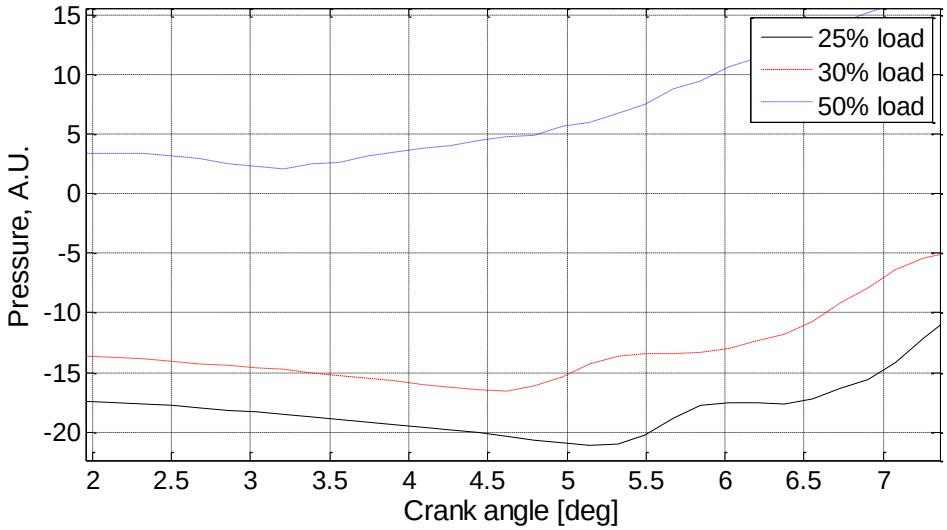

Figure 31: Cylinder pressure in arbitrary units as a function of CA for three load cases. The onset of pressure rise due to combustion is identified for each load case: 25%: 5.3 CA, 30%: 4.6 CA 50%: 3.2 CA.

investigated. When deposits build up at the surface they will act as a thermally insulating layer. This gives rise to a phase shift between the surface temperature of the soot exposed to the gas side and the surface temperature of the STC. The phase shift can to a first approximation be described by eq. (0.10) derived in Chapter 4:

$$\varphi_n(x_d) = x_d\sqrt{\frac{n\omega}{2\alpha}} \tag{0.28}$$

The first harmonic will be the first to arrive at the surface of the STC, thus, by setting n=1 in eq. (0.28) an expression for the shortest possible phase shift is found:

$$\varphi_1(x_d) = x_d\sqrt{\frac{\omega}{2\alpha}} \tag{0.29}$$

To determine the correct value for the thickness of the deposit layer, the thickness should somehow be measured in situ, since it might vary significantly during operation. However, this is not easy to do, and in fact no such method has been published, to this author's knowledge. Instead measurements have been carried out on the surface deposits after engine operation in a number of cases on small engines (see e.g. [64], [65] and [66]). Other studies also show that deposits will build up over time and reach an equilibrium thickness for constant speed and load operation (see e.g. [9], [67]). Furthermore, it has been shown that engine speed and load have a significant impact on thickness. Various techniques are available for post operation studies of the deposit properties (see [64] for further details).

The thermal diffusivity presumably does not change significantly during engine operation at locations where the lubrication oil is not present, and thus this quantity can be determined fairly accurately through post operation analysis. The deposits in a diesel engine are primarily carbon, with a minor content of hydrogen as well, forming aromatics [64].

In Figure 32 the phase shift is shown for three possible elements that could make up the deposit layer. Since the properties of the deposits in the MAN Diesel engine has not been measured in this work, the figure only shows some rough indications of what to expect.

Even though values for the thickness and thermal diffusivity are not available for the MAN engine, an estimate of the phase shift can still be calculated on the basis

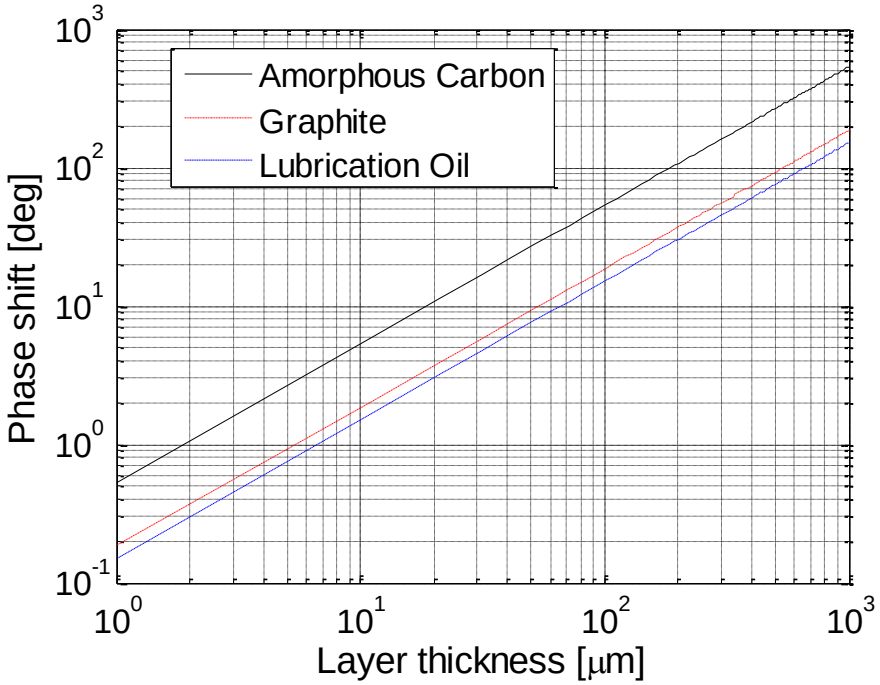

Figure 32: Phase shift of the deposit/metal interface temperature as a function of deposit layer thickness and type in a 50 % load case (material property data from [53], [54] and [55]).

of pressure and temperature traces. The start of combustion (SOC) is often determined from the onset of the cylinder pressure rise (equivalent to start of heat release) shortly after the start of fuel injection [30]. Assuming that the start of combustion immediately influences the deposit surface temperature, by means of a pressure rise induced increase in boundary layer temperature and radiation heat flux, the start of STC temperature rise (SOTR) can be used to determine the phase shift. This also requires that the increase in surface temperature of the deposits is large enough to result in a temperature increase at the deposit/STC interface that can be registered by the STC.

The SOC has been determined from the rise in the pressure traces shown in Figure 33 for three different load cases. The temperature rise at the surface of the STC has been determined from Figure 34. This was done by registering when the slope of curves becomes positive. For this purpose a numerical routine programmed in Matlab was used to compute the first order derivative. The results are collected in Table 3 along with the computed values of the phase shift simply by subtracting SOC from SOTR for each load case.

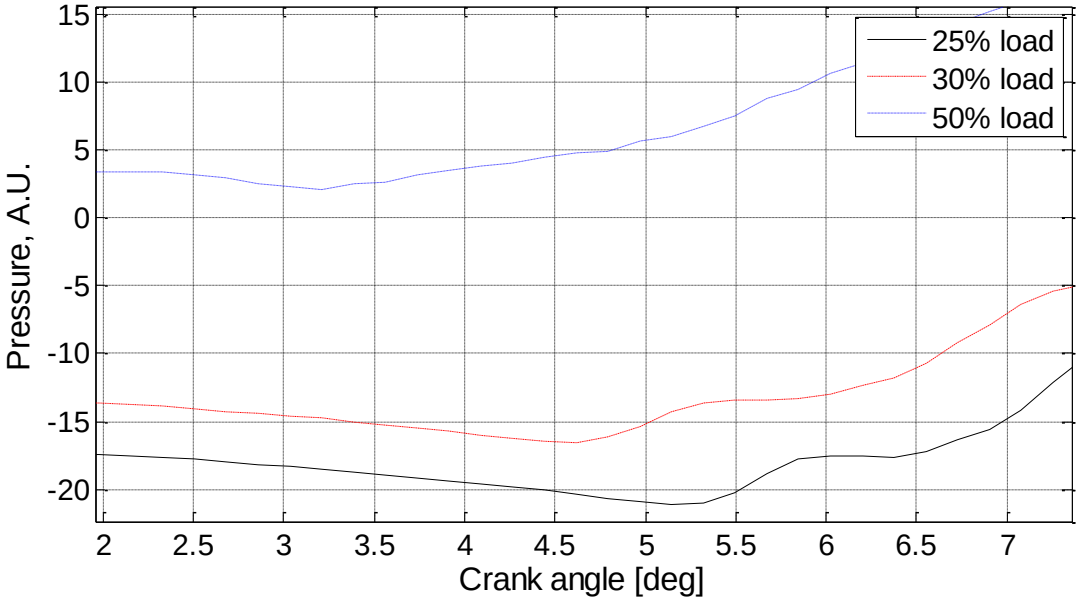

Figure 33: Pressure in arbitrary units as a function of CA for three different load cases.

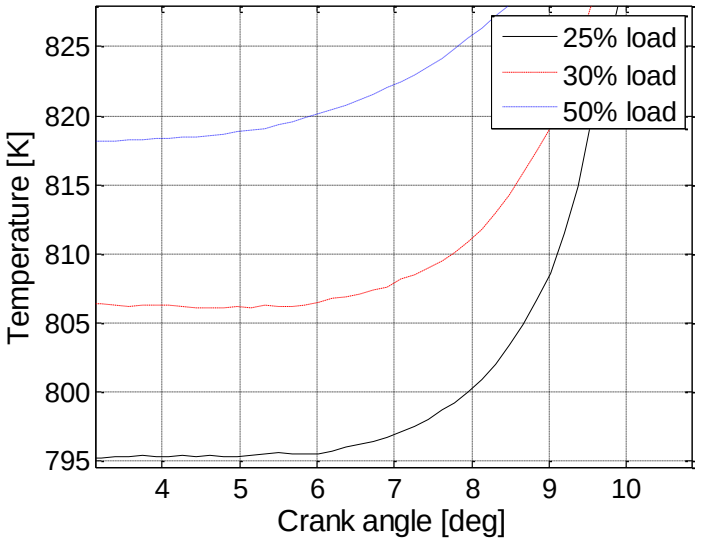

Figure 34: Surface temperature as a function of CA for three different load cases. The start of temperature rise (SOTR) due to combustion is identified for each load case: 25%: 6 CA, 30%: 5.8 CA 50%: 4.9 CA.

	SOC in CA, [deg]	SOC, [ms]	SOTR in CA, [deg].	SOTR, [ms].	Phase shift in CA, [deg]	Phase shift, [ms]
25% load	5.3	11.5	6	13	0.7	1.5
30% load	4.6	9.3	5.8	11.7	1.2	2.4
50% load	3.2	5.5	4.9	8.4	1.7	2.9

Table 3: SOC, SOTR and computed phase shift values for three different load cases.

As seen in Table 3, the phase shift increases with engine load. This increase can either be due to a decrease in thermal conductivity or an increase in deposition thickness. Since the phase shift is proportional to the square root of the thermal conductivity, it seems unlikely that the large increase in phase shift at higher load is caused solely by a decrease in thermal conductivity. On the contrary, there is reason to believe that changes in thermal conductivity with engine load are small at the

location of the thermocouple. In the work by [64] the composition of deposits in a diesel engine running on several different types of diesel fuel emulsions were analyzed in detail. Only small changes were detected in the composition, and in all cases the main content was carbon. However, only one engine speed was considered and the diesel fuel used was different from the diesel fuel used in the MAN Diesel engine test. In gasoline engines with a high amount of lubrication oil present in the combustion chamber, the thermal diffusivity has been shown to vary significantly with both engine load and different amounts of lubrication oil [65]. This could suggest that locations in the MAN test engine affected by the lubrication oil, e.g. the liner and piston rings, would probably have deposits with different thermal properties from load case to load case.

Assuming that the thermal conductivity does not change as a function of load, the observed difference in phase shift with load must be attributed to a change in the deposit layer thickness. The thickness is normalized by a factor of $\sqrt{\propto}$ and plotted as a function of load in Figure 35 to show how the thickness increases with load. Note that the relative increase is slightly different than the relative increase in phase shift with increasing load, since the angular frequency is different in each load case.

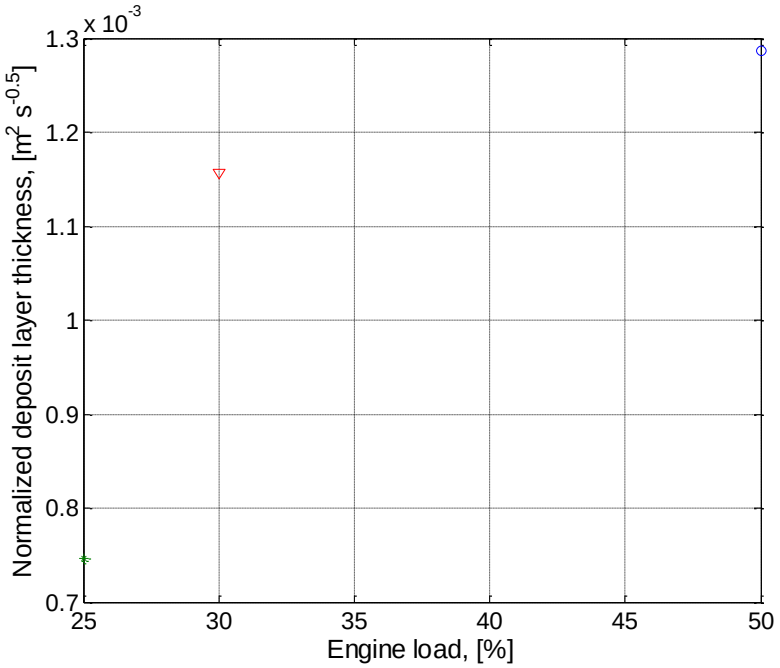

Figure 35: Normalized deposit layer thickness as a function of engine load.

Since the deposits act as thermally insulating layer that dampens the unsteady surface temperature from the gas/deposit interface, the STC receives a more smooth temperature signal than would have been the case if the deposit layer was thinner. This could explain why the first heat flux peak shortly after the start of combustion is shorter and broader in the 50% load case when compared to the 25% and 30% load cases (see Figure 28).

In this context, it is worth noting that according to eq. (0.9):

$$T(x_d,t) = \bar{T}_w - \frac{x_d}{L}(\bar{T}_w - T_b) + \sum_{n=1}^{N} e^{-\varphi_n(x_d)}\left[A_n \cos\left(n\omega t - \varphi_n(x_d)\right) + \mathrm{B_n}\sin\left(n\omega t - \varphi_n(x_d)\right)\right]$$

the phase shift term is also present in the exponential function in the unsteady term. Hence, for the summation terms referring to the higher harmonics the dampening caused by the exponential function is the greatest. This means that the rapid fluctuations, such as the steep increase in temperature at SOC, are more severely dampened than the lower frequency terms.

To illustrate how the deposit layer may affect the temperature registered at the STC when an abrupt change in the temperature at the gas side surface of the deposit layer occurs, a pulse response is considered. In Figure 36 the temperature at the deposit layer surface at the STC side is shown for a hypothetical situation where the gas side surface of the deposit layer is subject to a trapezoidal shaped pulse with a height of 60 K and a width of approximately 5 ms. It is clearly seen how the peak temperature is attenuated and how the shape of the applied trapezoidal pulse is changed significantly. Especially the “smoothing” of the corner at around 0.023 to 0.024 ms is important to note, since it has a large impact on the subsequently derived heat flux.

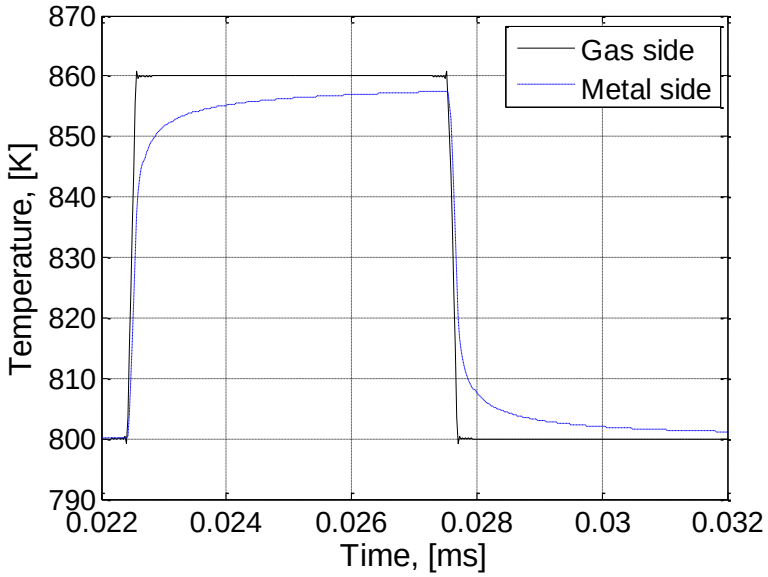

Figure 36: Surface temperature at the gas side and metal side (deposit/STC interface) of a deposit layer of amorphous carbon subjected to an approximately 5 ms wide and 60 K high pulse (at the gas side).

The heat flux at the metal surface is shown in Figure 37 for the case were the deposit layer is present and the case where no deposit layer is present and the temperature profile is simply given by the trapezoidal profile. Of course this is a hypothetical scenario since heat transfer to the surface is dependent on the physical properties of the surface (emissivity, roughness etc.) which are different for the clean metal surface and the deposit layer. However, it gives a good picture of the relatively large impact of the deposit layer on both the temperature and the surface heat flux. Especially the peak heat flux is strongly attenuated by the presence of the deposit layer even though the temperature profile seems fairly close to the applied trapezoidal pulse in magnitude.

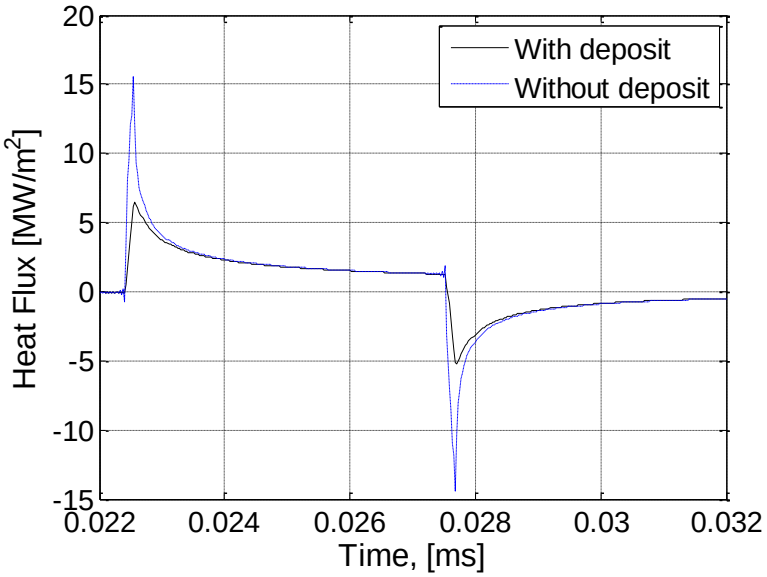

Figure 37: Surface heat flux at the metal surface with and without deposit layer (based on temperature data from Figure 36).

The power spectrum of the Fourier series for both temperature profiles are shown in Figure 38. The predicted behavior of strong attenuation of the higher harmonics due to the presence of the deposit layer is clearly observed. The diminishing of the higher harmonics is the reason for the smoothing of the temperature profile at the metal surface and the reason why the peak heat flux is attenuated so strongly.

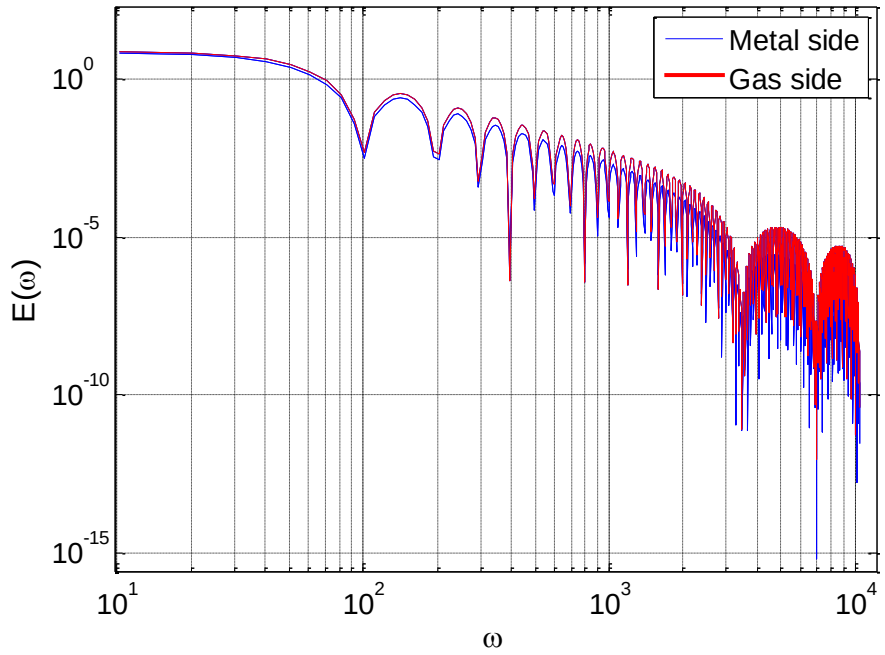

Figure 38: Power spectrum for the Fourier series representation of the surface temperature at the gas side and the metal side of the deposit layer.

Decoupling of radiation and convective heat flux

The surface heat flux computed on the basis of the thermocouple measurements is the total surface heat flux, consisting of a radiation and a convective contribution. In principle, there is interplay between these two different types of heat transfer, since both are affected by a change in surface temperature. E.g. if the surface temperature is raised due an increase in radiation heat flux from the sooty diffusion flame, the convective heat transfer is lowered at the deposit layer/gas interface

since the temperature gradient is decreased. Furthermore, due to the increase in surface temperature, the amount of radiation heat transfer emitted by the surface is increased. However, this flux emitted from the surface is negligible compared to both the incoming flux from the soot radiation and the convective heat transfer. Thus, it is possible to treat the radiation and convection heat transfer separately. Calculating the true thermal radiation inside the engine cylinder is a highly complex task that in principle requires exact knowledge of the local concentrations, temperatures and material properties of various compounds. Even though only the thermal radiation from soot is considered it is still not trivial to accurately compute the radiation. Different models to calculate soot radiation and scattering properties of soot have been developed over the past three to four decades focusing mainly on the amount, distribution and the shape of the particles and agglomerates [68] but only with limited success. An overview of some of the most widely used models is given in [68]. Since little is known about the amounts, shape and distributions of soot within large two-stroke ship diesel engines it makes it difficult if not impossible to apply any of these soot models to the MAN test engine at this stage. However, in an attempt to estimate the magnitude of the soot radiation arriving at the location of the STC and compare it with the measured total surface heat flux, a very simple approach based on Planck radiation from solid objects is chosen. It relies heavily on a number of more or less justified assumptions described in the following and the results should therefore be treated with great care.

Assuming that the radiation heat transfer to the surface of the STC from the soot during combustion can be described by the equation for a small convex object in a large cavity (a two-surface enclosure type problem) [42]:

$$q''_{rad}(t) = \sigma\varepsilon(T(t)^4_{flame} - T(t)^4_{wall}) \quad (0.30)$$

Where ε is the emissivity of the soot, σ is the Stefan-Boltzman constant and a viewing factor of 1 is assumed. The exact value of the viewing factor is hard to calculate since it depends on the location of the thermocouple surface in relation to the distribution of the soot which is changing dramatically during combustion (i.e. with time). Furthermore, the soot is assumed a perfect emitter that radiates continuously over the infrared spectrum (blackbody radiation). In addition to the soot radiation, different gases surrounding the flame will have absorbing and emitting features that might influence the radiation heat transfer between the soot and the STC. However, the soot radiation is assumed to be the dominating source of radiation and hence the gas radiation is assumed negligible in this first approximation approach.

The most difficult task is to determine the effective temperature of the soot. In the following, an estimate of the soot temperature will be made based on experimental studies on the MAN test engine.

In the work of [30] the flame temperature was measured in the MAN test engine by means of two-color pyrometry at 50% load. The averaged flame temperature deduced from averaging each color map for each CA for the entire field of view is

shown in Figure 39. In Figure 40 the images taken by the two-color pyrometry method is shown. Since the data in Figure 39 is computed by averaging the temperature values from the images in Figure 40, it yields a lower temperature than the maximum temperature of the radiating soot because some of the gases surrounding the flame front are significantly cooler than the soot.

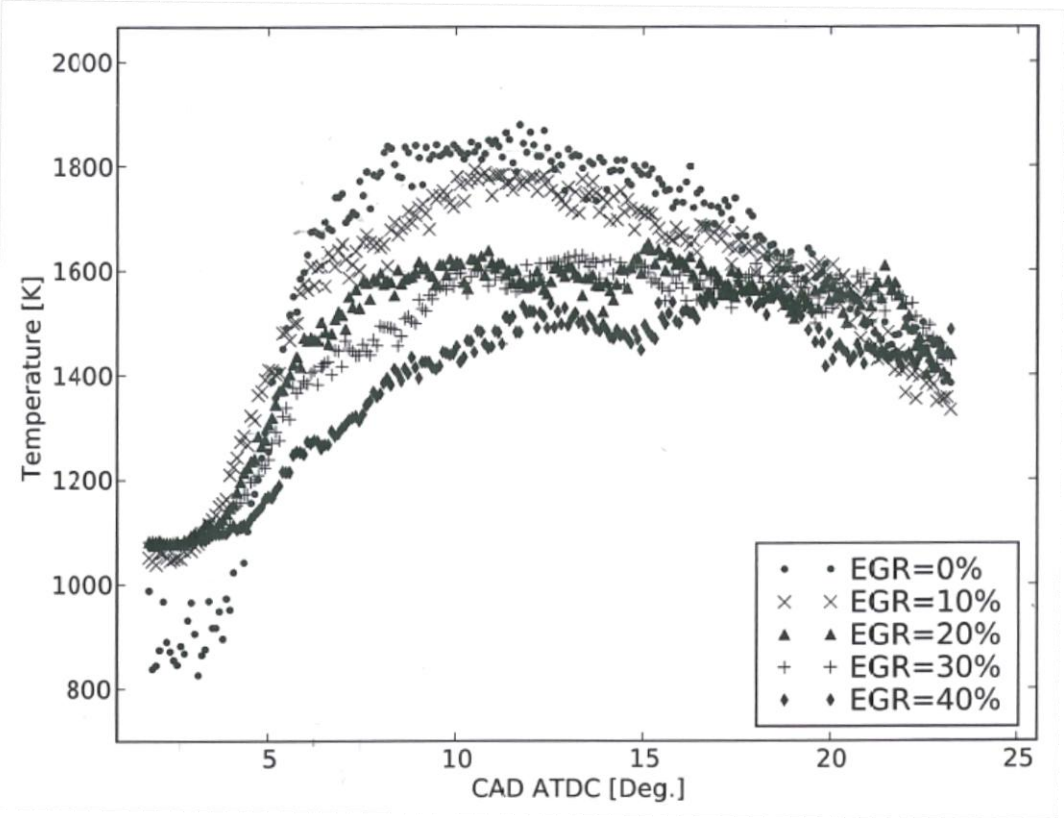

Figure 39: Averaged flame temperatures determined by two-color pyrometry for different levels of exhaust gas recirculation (EGR) at 50% load [30].

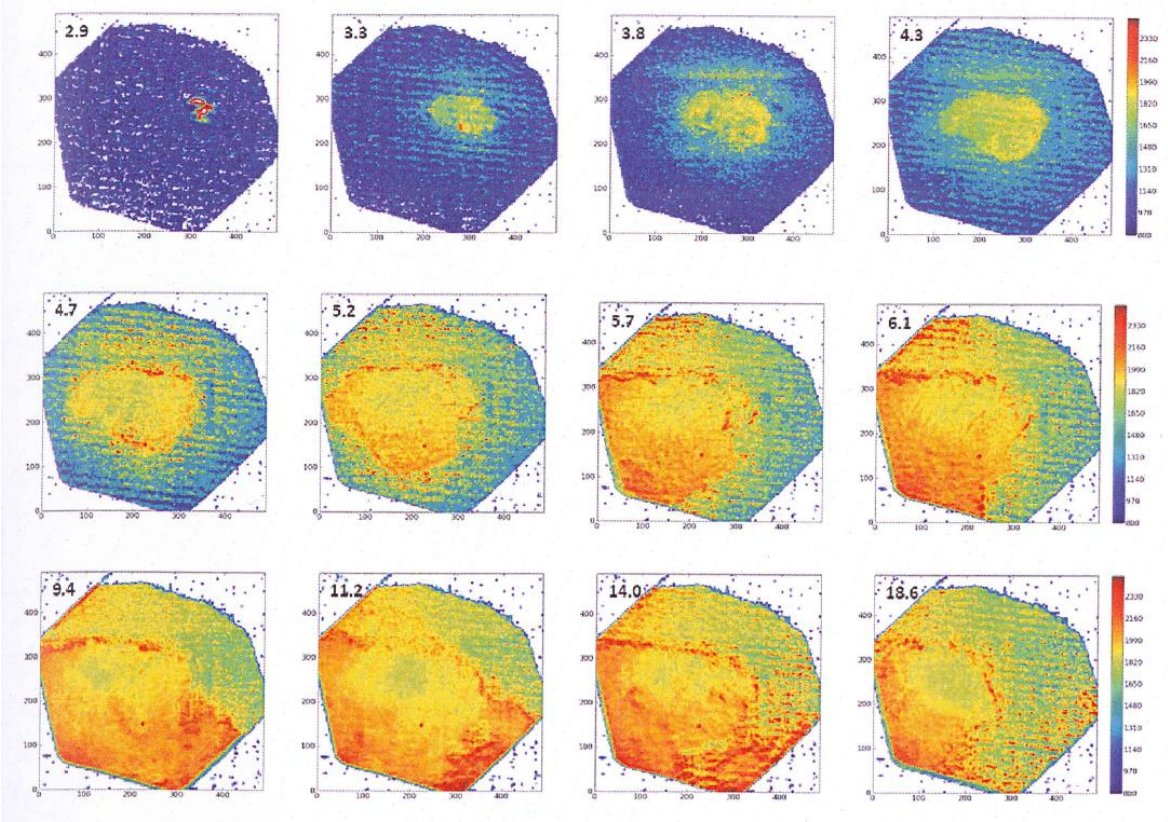

Figure 40: Two-color pyrometry images from selected points in the cycle. Numbers in the upper left corners of the pictures denote the CA. The scale on color bar starts at 800 K (dark blue) with increments of 170 K up to 2500 K (dark red) [30].

A very rough way of estimating the minimum and maximum temperatures of the radiating soot as a function of CA was done by simply picking discrete data points from Figure 39 and Figure 40. The points were then fitted with a shape preserving spline routine in Matlab. The result is shown in Figure 41.

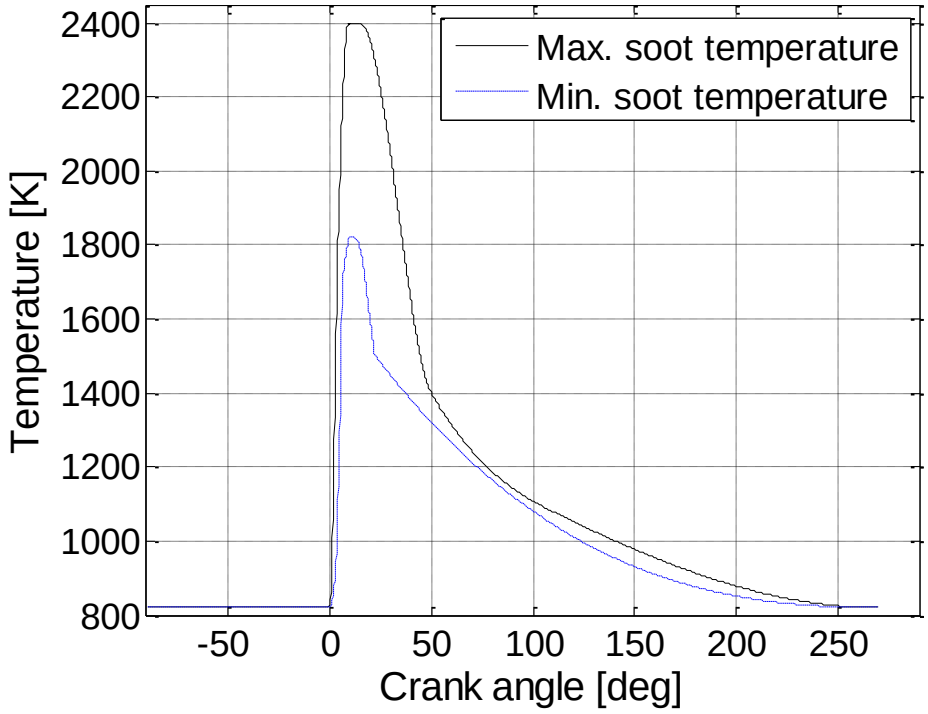

Figure 41: Maximum and minimum soot temperature as a function of CA. The data is based loosely on the reported values in [30] for only a part of the combustion. A shape preserving spline routine has been used for fitting.

Assuming an emissivity of 1 for the soot, a very rough estimate of the maximum radiation from the soot the surface was calculated using eq. (0.30). The wall temperature in the equation was determined by the surface temperature measured by the STC, even though the outer surface of the deposit layer has a higher temperature during the period of positive surface heat flux and a slightly lower value at the period of negative heat flux. Furthermore, the radiation heat flux was delayed 1.7 CA to account for the phase shift.

The computed maximum and minimum radiation heat fluxes are shown in Figure 42, along with the total surface heat flux with and without the subtracted radiation heat fluxes.

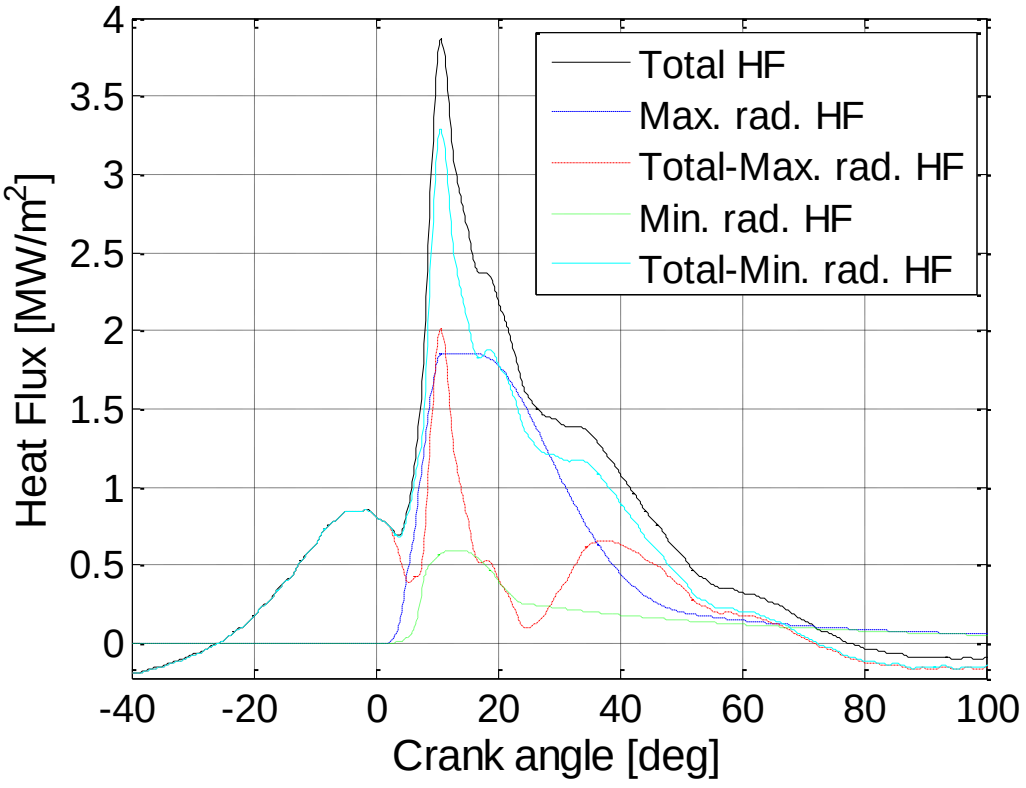

Figure 42: Heat flux (HF) profiles as a function of CA for the 50% load case.

This gives some indication of the possible magnitudes of the maximum and minimum convective and radiation heat flux contributions. For the estimated maximum value of the radiation heat flux, the peak value is almost half the peak value of the total heat flux. It seems that the maximum estimate is too high

(and/or for a too long period), since there is a significant drop in the convective heat flux curve around 15-35 CA. At least there is no obvious reason for a drop in convective heat flux at this period during the combustion phase. On the contrary, the minimum estimate is probably too low, especially around the start of combustion, where at least some positive radiation heat flux would be expected. This is most likely caused by the aforementioned averaging procedure used to calculate the average temperature of the field of view for the camera, where a relatively large part of the image is consisting of the surrounding gases with a significantly lower temperature than the flame. Thus the true amount of radiation and convective heat flux is probably lying somewhere in between the maximum and minimum estimates.

Chapter 6: 3-D Heat Conduction Calculation using the Finite Volume Method

Investigations of the one dimensionality assumption described in Chapter 4 have shown that it is not strictly justified in all cases when a thermocouple of slightly different material properties than the material properties of the wall [12]. Since the choice of materials, geometry etc. can differ from application to application, it is recommended that analysis of the perturbed temperature field at the location of the thermocouples should be carried out. For this purpose, two models were constructed and transient simulations were performed using the computational fluid dynamics (CFD) tool, STAR-CD from Adapco, version 4.12 (with patch 038). Even though the computational fluid dynamics software is originally developed primarily to solve the Navier-Stokes equation using different approaches and various transport equations for 3-D fluid flows, STAR-CD can also handle heat conduction problems in solids. In fact, it requires less computational power than employing a finite element method and also has the advantage that both solid structures and fluids can be part of the model if needed. Hence the models presented in this chapter could be further developed to include the gas flow and its interaction with the wall.

For further details on the finite volume method utilized by STAR-CD the reader is referred to the STAR-CD manual and [69].

Geometry and boundary conditions (model 1)

The dimensions of the STC, was determined by the use of a microscope and an optical grid scale. The model sketch is shown in Figure 43.

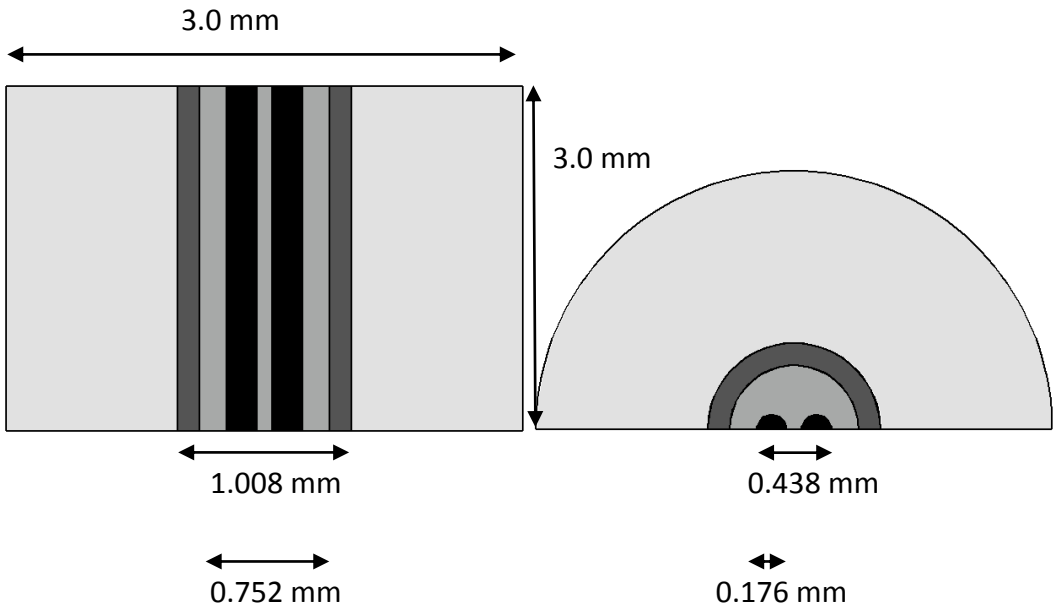

Figure 43: Sketch of the atomizer with the installed STC used for generating the mesh in STAR-CD.

The model only consists of half the cylinder as shown on the sketch, since there is a symmetry plane passing through the center of the two thermocouple legs. Thus computational time can be reduced by only simulating half of the cylinder. The time varying STC data (for the 50% load case) was used to impose the boundary condition at the top. 40 cycles of the ensemble averaged STC temperature profile was put into a table file in STAR-CD, and these points were then used to set a fixed temperature for the top surface for every iteration.

A fixed wall temperature boundary condition was imposed at the bottom such that it matched the computed heat flux through the wall (presented in the previous chapter). Symmetry plane boundary conditions were imposed at the remaining outer boundaries. The material properties used were based on the values presented in Appendix II. Star-CD has the ability to work with temperature dependent material properties but since the parameter variation study presented in the previous chapter showed a negligible impact of varying material properties it was decided to use constant values in this model as well.

A polyhedral mesh consisting approximately 300,000 cells was then constructed, with improved refinement at the top of the STC. The mesh is shown in Figure 44. Grid independency was checked using two polyhedral meshes consisting of 50,000 and 100,000 cells respectively.

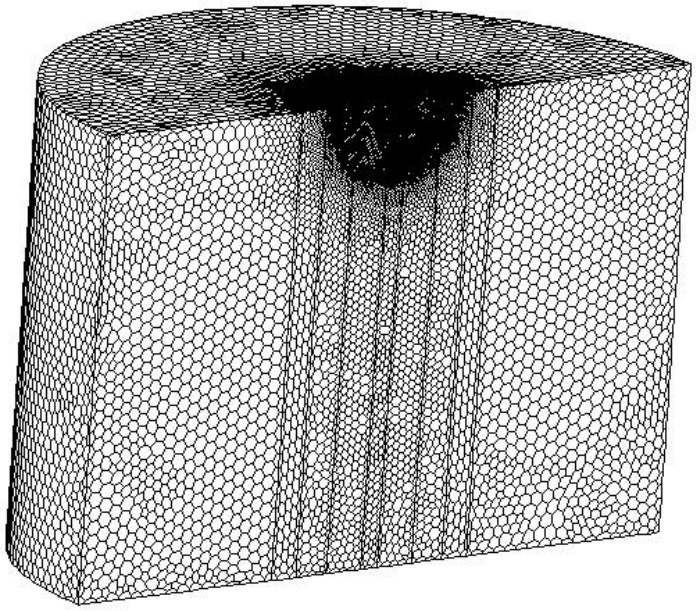

Figure 44: Model mesh consisting of approximately 300,000 cells.

A constant time step of 0.3 ms was used, and the temperature field was saved for every 30 ms (i.e. 20 times per engine cycle) starting at TDC. A monitor cell was chosen at the center of the location of the hot junction, such that the difference between the temperature of the monitor cell and the applied surface temperature could be calculated in the post processing. Thereby an estimate of the uncertainty in the measured surface temperature signal can be deduced.

Results (model 1)

The temperature maps at 12 different CA positions ranging from TDC to 198 CA are shown in Figure 45 and Figure 46. The temperature maps clearly show that the temperature field is perturbed in the vicinity of the STC due to the difference in

material properties. The degree of perturbation is highest at the periods in the cycle where the change in surface temperature is highest. However, even though the difference between the interior of the STC and the bulk of the atomizer close to the outer boundaries seems large, the temperature of the hot junction is within 0.4 K of the imposed temperature boundary condition a the top. Thus the perturbation effect induced by the presence of the STC is introducing an uncertainty in the measured signal at a maximum magnitude of 0.4 K, which is highest at the periods in

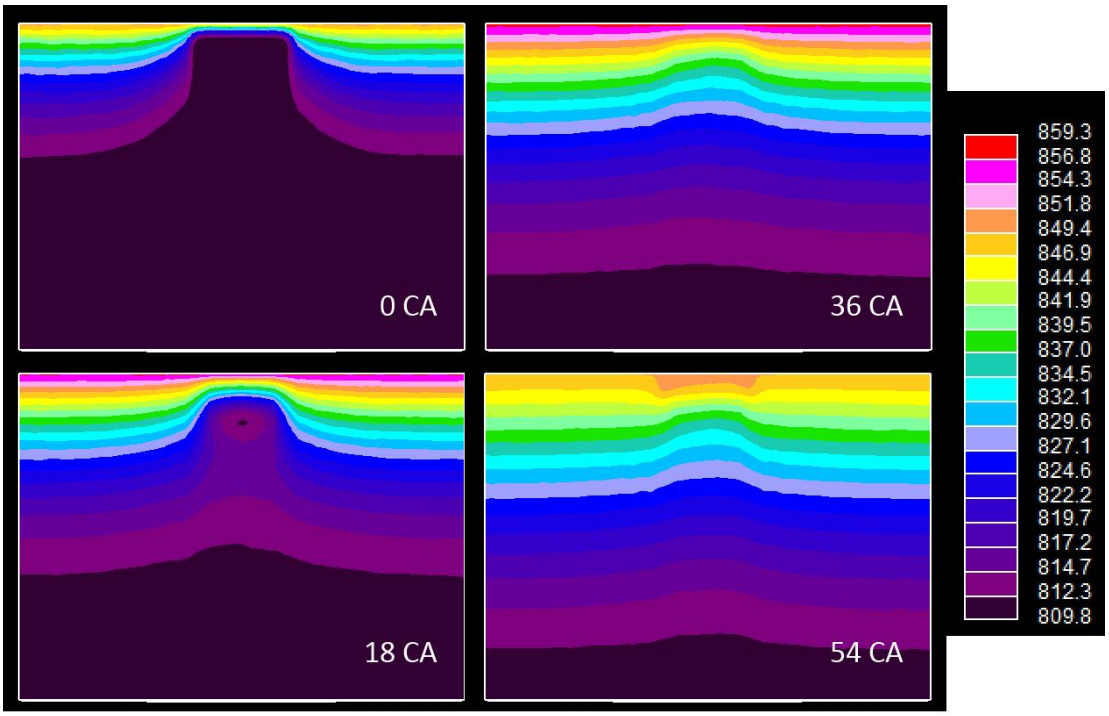

Figure 45: Temperature maps of the STC and atomizer at the symmetry plane cross-section at four different CA. The color bar to the right is showing the temperature in K.

the cycle where the surface temperature gradients are highest.

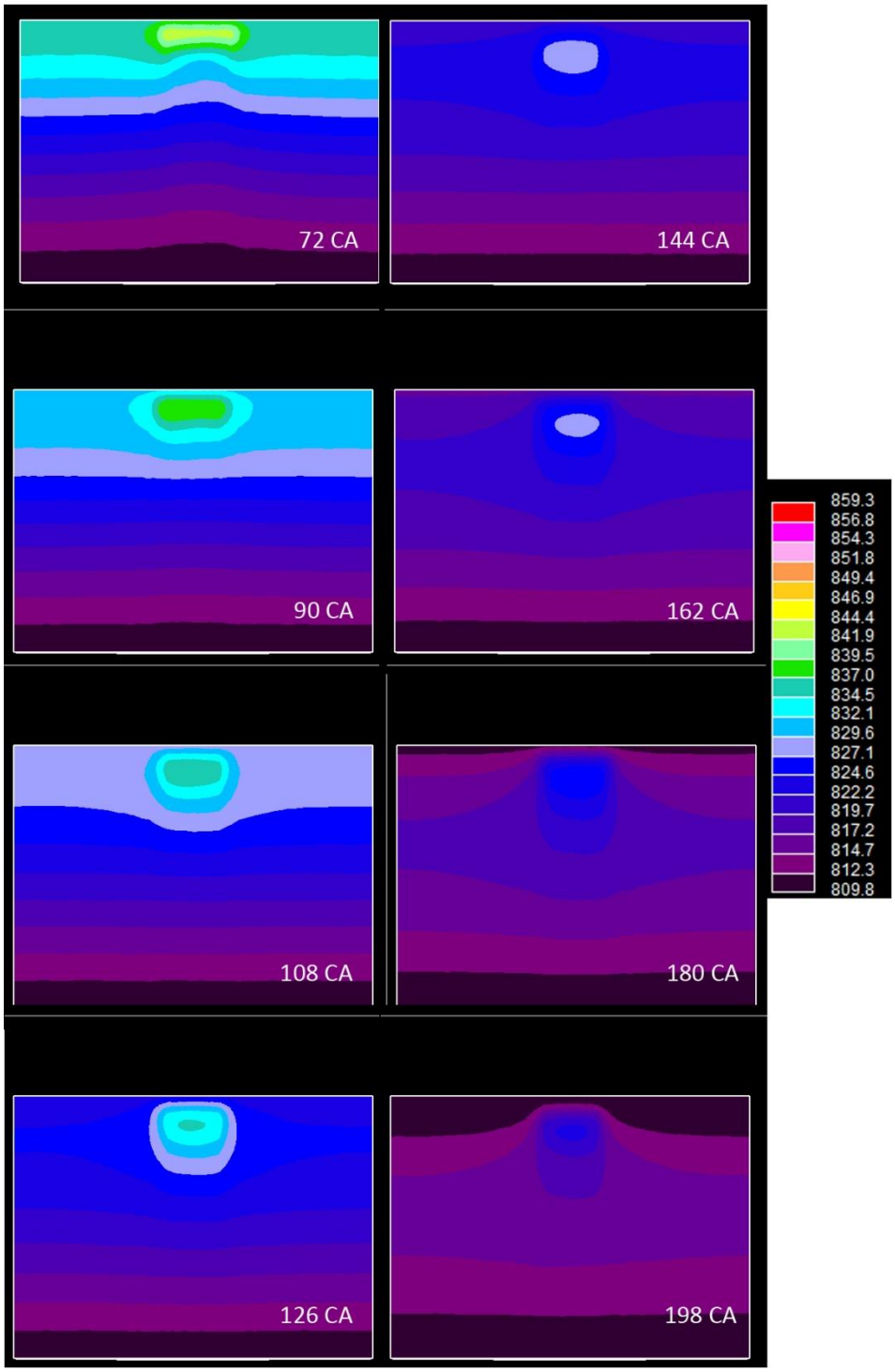

Figure 46: Temperature maps of the STC and atomizer at the symmetry plane cross-section at eight different CA. The color bar to the right is showing the temperature in K.

Geometry and boundary conditions (model 2)

To investigate the degree of perturbation at the location of the bulk thermocouple, a model was constructed based on the mesh presented in the previous section to save time. The physical scaling of the mesh was done by setting the scaling factor in STAR-CD to match the new dimensions. The outer dimension was changed from 3 mm to 19 mm (a scaling factor of around 6). The boundary condition at the bottom was changed accordingly to match the heat flux.

Results (model 2)

Two simulations were performed. One simulation where the thermocouples were present and one simulation without thermocouples (constant material properties throughout the whole domain). Thus, by subtracting these two solutions from each other, the degree of perturbation is envisaged. The result is shown in Figure 47 at around the start of combustion, where the perturbation is at its maximum value. The outer boundaries of the two thermocouples are marked by the red dashed lines.

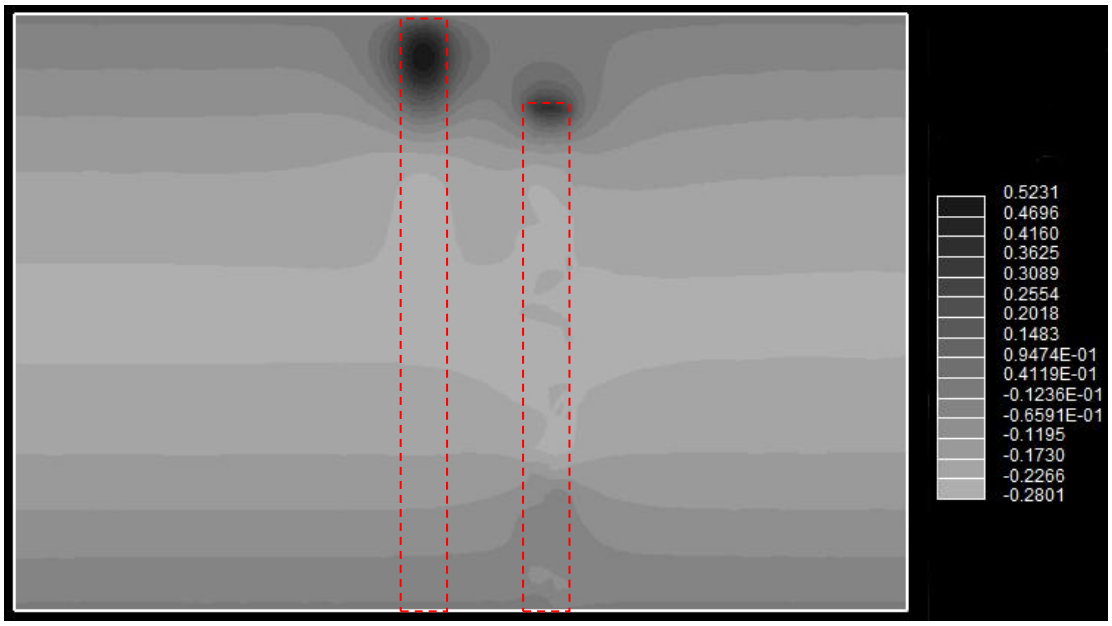

Figure 47: Subtracted temperature fields in the interior of the atomizer dummy. The red dashed lines show the location of the two thermocouples. The grayscale is in K.

The maximum value of the temperature perturbation can be seen on the grayscale next to the simulation result. The temperature perturbation is highest at the location of the BTC hot junction with a value around 0.5 K. At the location of the STC hot junction the temperature perturbation is around 0.2 K. A comparison with these values to the estimated total measurement uncertainty of a class one K-type thermocouple of around (+/-) 2.3 K shows that they are significant contributions although not the major source. To ensure that cyclic steady state was reached, the temperature difference between the peak temperatures of two consecutive cycles

were calculated for a monitor cell located in the bulk of the wall close to the top of the domain. The result is shown in Figure 48, which shows cyclic steady state after around 30 cycles. Thus the 40 cycles used for the simulation is sufficient.

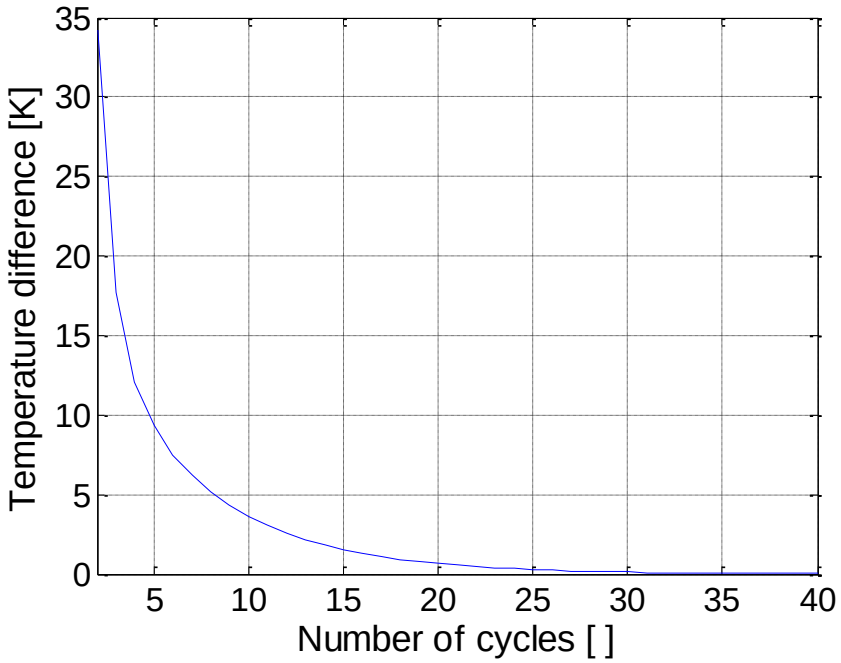

Figure 48: Temperature difference between the peak temperatures of two consecutive cycles. The graph shows how periodic steady state is reached in the numerical model after approximately 30 cycles.

Chapter 7: Suggestions for future work

In this chapter some recommendations for future work are presented:

- Since only a limited range of engine load conditions was studied in the surface temperature and heat flux measurements, it would be natural to extend this range to lower and higher load scenarios including motoring.
- Improvements in the installation technique used for mounting the surface temperature thermocouple would be necessary to completely avoid the thermocouple from breaking loose due to the elevated pressures in the engine cylinder. This is especially important at high load conditions where the peak pressure is usually around 200 bar. A possible design modification of the thermocouple that could overcome this problem is to make the outer sleeve of the thermocouple slightly conical in shape instead of the present cylindrical shape. Another solution could be to have some kind of mechanical mount on the backside of the thermocouple (the location where it enters the engine from the outside) that can prevent the thermocouple from leaving its position. Three possible thermocouple mounts are sketched in Figure 49, encompassing a cylindrical, conical and threaded mounting type.

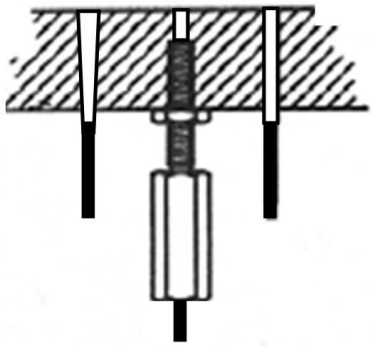

Figure 49: Different ways to mount the surface temperature thermocouple. Right: Cylindrical shape (the mounting type used in this work). Middle: Threaded thermocouple jacket with a nut welded on the backside to fix the thermocouple position. Left: Conical shape.

- Due to the complexity and high degree of variation in instantaneous heat transfer and temperature from one location to another at the surface of the cylinder head, liner, piston crown etc., it would be highly recommended to install thermocouples at multiple locations. In this way, detailed information on local instantaneous temperatures and heat fluxes could be captured simultaneously which would be of great value for computer simulation purposes, validation and for general assessment of thermal loading of engine components and the total heat loss from the engine.
- As discussed in Chapter 5, the radiation heat flux, during the period of combustion, may contribute significantly to the total amount of surface heat flux. Thus, accurate measurements of the radiation heat flux would be very useful in extracting the convective heat transfer contribution from the total surface heat flux obtained by the method described in this study. One possibility is to mount an optical fiber in the atomizer dummy with the center axis aligned orthogonally to the surface and measure the thermal

radiation guided through the fiber by using a Fourier Transform Infrared Spectrometer (FTIR). Since only the total amount of radiation per sampling time interval is needed, the spectral resolution of the FTIR measurements can be made sufficiently low such that the sampling time can be decreased to level where it match the temporal resolution of the thermocouple measurements. An alternative to this method is simply using a thermocouple similar to the one used in this study where an optical window is placed in front of the thermocouple. The material of the window should be chosen so that it does not block too much of the energy containing radiation in the infrared and visible range (Sapphire crystal might be a reasonable choice). Furthermore the thickness of the window should be sufficiently large to withstand the huge pressures and to eliminate the transient temperature fluctuations at the location of the thermocouple hot junction. Then, if the steady flux component is known (theoretically or experimentally) it can be subtracted and the remaining flux is due to radiation only. However, one has to make sure that the optical window (or the fiber) is not blocked optically by deposits building up on the surface over time.

- Further studies of the composition, thermo physical properties and thickness (as a function of engine load) of the deposit layer at the combustion chamber wall would be necessary to quantify the absorbed and emitted radiation from the surface. Furthermore, this could lead to an estimation of the

deposit layer surface temperature (at the gas side) which plays a major role in both the chemical and physical interaction between the working fluid and the deposit surface.

- Even though no drift was observed in the measured temperature signal during the course of the experiments, it is recommended that a post calibration of the thermocouples should be performed for a more rigorous confirmation of the stability of the thermocouples.

Chapter 8: Conclusion

The main focus of this study has been on the local varying temperatures and heat transfer at the in-cylinder surface in a large two-stroke diesel engine. One of the major tasks has been the development of a special surface thermocouple which was used for temperature measurements at the surface of one of the spray atomizers installed in the MAN Diesel & Turbo SE test engine in Copenhagen. Prior to these measurements a series of response time tests were carried out showing sufficiently low response time of around 0.1 ms. This response time makes it possible to resolve down to one tenth of a crank angle degree even at the highest engine speeds. In order to comply with the demands of high speed data acquisition, a custom made signal conditioner was built with a cut off frequency of 10 kHz. From the first engine test it was concluded that noise plays a large role when measuring the small voltage output signals from the thermocouples in such a noisy environment. By subsequently modifying the signal conditioner and wire extensions the noise was reduced significantly yielding a signal to noise ratio of around 250 which, by normal temperature measurement standards, is considered very good.

The robustness of the surface temperature thermocouples was studied by several hours of continuous engine operation. However, since it was only possible to run two separate engine tests due to time limitations it is not clear exactly how robust the surface thermocouple is but at least one day of experiments is possible. The first

test showed a lift off of the protective gold layer coating resulting in an abrupt change in output signal probably due to damage of the hot junction and surrounding materials. In the second engine test the thermocouple was ejected out of the atomizer after one day of testing due to the large pressure and temperature rise in the engine.

Local surface heat flux calculations were carried out based on the measured temperatures from the surface and below the surface. Two different mathematical models were used to compute the surface heat flux showing excellent agreement when comparing the results. Three different speed and load scenarios were studied, namely 25% (77 rpm), 30% (82.3 rpm) and 50% (97 rpm).

The calculated values of both peak and mean surface heat flux was of the same order of magnitude as reported elsewhere in the literature but due dissimilarities in geometry and material properties etc. between the engines a direct comparison was not possible.

The mean surface heat flux was found to vary only slightly as a function of load and speed showing a trend towards an increase in heat flux with an increase in load and speed. However, the peak surface heat flux had an unexpected trend which showed an increase in peak heat flux with a decrease in load and speed. This could be a result of the unsteady nature of the flow of the hot gases inside the cylinder creating local changes in heat transfer rates which are not representative for the general

heat transfer from gas to wall. In the meantime, estimates of the radiation heat transfer from the soot showed that it might contribute significantly to the overall heat transfer to the walls during combustion. If this is indeed the case the abrupt change in the surface temperature signal at the onset of combustion should occur at the same time independent of load. However, this was not the case and a likely explanation could be a change in the thickness of deposits at the surface of the thermocouple hot junction. This would also offer and explanation of the observed trend in peak surface heat flux which is lowered due to the dampening of the true surface temperature by the insulating layer of deposits. It should be stressed that this is still an unproven hypothesis which would require further studies of deposit layer thickness measurements as a function of load together with analysis of the composition of deposits to determine the relevant material properties like density and thermal conductivity.

Finally, a 3D numerical study was carried out to show to which degree the thermocouples perturb the temperature field around the location of the hot junctions and thus limits the measurement accuracy. For this purpose a simulation was performed solving the unsteady heat conduction problem around the location of the thermocouples. The results showed that a measurement error contribution of max 0.5 K can be attributed to the presence of the thermocouples for the specific materials used in this study. Compared to the total measurement uncertainty of

around (+/-) 2.3 K of a class one K-thermocouple the contribution is significant but not dominating.

All in all, the measurement method and equipment described in this study have proven it's capability to give added insight in the heat transfer inside large bore diesel engines. It is the hope that future studies will benefit from this work and help to create the basis for a more detailed description of heat transfer in large bore two-stroke diesel engines for ship propulsion by e.g. following some of the recommendations given in Chapter 7: Future Work.

Chapter 9: Bibliography

1. Web page for the International Maritime Organization. [Online] www.imo.org.

2. Web page for the Diesel Network Community. [Online] www.dieselnet.com.

3. *New Insights into the Mechanisms of In-Cylinder Heat Transfer In Diesel Engines.* **Boulouchos, K and al., et.** s.l. : SAE International, 1989, Vol. 890573.

4. *Internal-combustion engine heat transfer.* s.l. : Prog energy comb sci, 1987, Vols. 13, p. 1-46.

5. *Direct heat loss to combustion chamber walls in a direct-injection diesel engine: evaluation of direct heat loss to piston and cylinder head.* **Suzuki, Y and al, et.** s.l. : International Journal of Engine Research, 2005, Vols. 6, p. 119-135.

6. *Study on analysis of instantanous heat flux flowing into the combustion chamber wall of an internal combustion engine - examination in the case of consideration of heat storage term and the temperature dependency of the thermocouples thermophysical proper.* **Enomoto, Y and al, et.** s.l. : JSME International Journal Series B, 1992, Vols. 35, p. 608-615.

7. **Dam, B.** *Experimental and Numerical Investigations of Sprays in Two Stroke Diesel Engines.* s.l. : PhD Thesis, Department of Mechanical Engineering, Technical University of Denmark, 2007.

8. **Heywood, J B.** *Internal Combustion Engine Fundamentals.* s.l. : McGraw-Hill, 1988.

9. *Internal-Combustion Engine Heat Transfer.* **G, Borman and K, Nishiwaki.** s.l. : Prog Energy Combust Sci, 1987, Vols. 13, p. 1-46.

10. *Some new investigations on old combustion engine problems.* **Eichelberg, G.** s.l. : Engineering, 1939, Vols. 148,p. 547-560.

11. *A universally applicableequation for the instantanous heat transfer coefficient in the internal combustion engine.* **Woschni, G.** s.l. : SAE, pap no. 670931, 1967.

12. *Instantanous heat transfer rates to the cylinder head surface of a small compression-ignition engine.* **Annand, W J D and Ma, T H.** s.l. : Proc. Instn Mech. Engrs, 1971, Vols. 185, p. 976-987.

13. *The effects of swirl and injection parameters on diesel combustion and heat transfer.* **Gerpen, V, Huang, J H and Borman, G.** s.l. : Society of automotive engineers, 1985, Vol. pap. no. 850265.

14. *Experimental instantaneous heat fluxes in a diesel engine and their correlation.* **LeFeuvre, T, Myers, P and Uyehara, O.** s.l. : SAE, pap. no. 690464, 1969.

15. *Transient heat flux measurements in the combustion chamber of a spark ignited engine.* **Alkidas, A C and Myers, J P.** s.l. : Trans. ASME, Journal of heat transfer, 1982, Vols. 104, p. 62-67.

16. *An experimental determination of the instantaneous potential radiant heat transfer within an operating diesel engine.* **Flynn, P, et al.** s.l. : SAE, pap. no. 720072, 1972.

17. *Instantaneous Local Heat Flux Measurements in a Small Utility Engine.* **Hendricks, T, Gandhi, J and Brossman, J.** s.l. : ASME, 2009.

18. *Measurement of piston temperature of spark-ignition engines.* **Hara, M and Oguri, T.** s.l. : Bull. JSME, 1959, Vols. 2, p. 382-389.

19. **Bentley, R E.** *Theory and Practice of Thermoelectric Thermometry, volume 3 of Handbook of Temperature Measurement.* Singapore : Springer-Verlag, 1998.

20. NIST ITS-90 Thermocouple Database. [Online] National Institute of Standards and Technology, 2010. http://srdata.nist.gov/its90/main/.

21. **Elshabini-Riad, A and Barlow, F D.** *III: Thin Film Technology Handbook.* s.l. : McGraw Hill, 1998.

22. **Smith, D L.** *Thin-film Deposition: Principles and Practise.* s.l. : McGraw Hill, 1995.

23. *A special Thermocouple for Measuring Transient Temperatures.* **Bendersky, D A.** s.l. : Mech. Engr., 1953, Vols. 75, p. 117-121.

24. *Transient Temperature in Engineering and Science.* **Lawton, B and Klingenberg, G.** s.l. : Oxford University Press, 1996.

25. *Transient response of an erodable heat flux gauge using finite element analysis.* **Buttsworth, D R.** s.l. : Proc Instn Mech Engrs, J Automobile Engineering, 2002, Vol. 216 Part D.

26. *Thermocouple materials, Applied Methods and Instruments, Its Measurement and Control in Science and Industry.* **Caldwell, F R.** s.l. : Reinhold, New York, 1962, Vols. 3, p. 81-134.

27. *Advanced approaches for heat transfer calculations.* **Hohenberg, G F.** s.l. : SAE, 1979, Vols. pap. no. 790825, in SP-449.

28. *A miniature sensor for measuring heat transfer rates in engines.* **Mattavi, J N.** s.l. : SAE, 1974, Vol. pap. no. 741078.

29. *Spray and combustion characterization for internal combustion engines using optical measuring techniques - A review.* **Soid, S N and Zainal, Z A.** s.l. : Energy, 2010, Vols. 36, p. 724-741.

30. **Poulsen, H H.** *In-situ Investigations of the Combustion in Large, Two-stroke, Diesel Engines.* s.l. : Center for Energy Resources Engineering, Technical University of Denmark, 2009, PhD Thesis.

31. *A system for quantitative imaging diagnostics and its application to pyrometric in-cylinder flame-temperature measurements in large diesel engines.* **Vattulainen, J, et al.** s.l. : Measurement Science Technology, 2000, Vols. 11, p. 103-119.

32. *Optical Diagnostics for Soot and Temperature Measurements in Diesel Engines.* **Zhao, H and Ladommatos, N.** s.l. : Progress in Energy and Combustion Sciences, 1998, Vols. 24, p. 221-255.

33. **Commission, European.** Hercules Beta Project. [Online] 2010. http://www.hercules-b.com/1/article/english/1/2/index.htm.

34. *Quantitative Mixing Measurements in a Vaporizing Diesel Spray by Rayleigh Imaging.* **Idicheria, C A and Pickett, L M.** s.l. : SAE International Journal of Fuels and Lubricants, 2007, Vol. 116.

35. **Laboratories, Sandia National.** Engine Combustion Network Homepage. *Engine Combustion Network Homepage.* [Online] www.sandia.gov/ecn/.

36. *Comparison of Diesel Spray Combustion in Different High-Temperature, High-Pressure Facilities.* **Pickett, L M, et al.** s.l. : SAE International Journal of Engines, 2010, Vols. 2010-01-2106.

37. *Planar Laser Rayleigh Scattering for Quantitative Vapor-Fuel Imaging in a Diesel Jet.* **Espey, C, et al.** s.l. : Combustion and Flame, 1997, Vol. 109:65.

38. *Diagnostic Considerations For Optical Laser-Extinction Measurements Of Soot In High-Pressure Transient Combustion Environments.* **Musculus, M P B and Pickett, L M.** s.l. : Combustion And Flame, 2005, Vols. 141, p. 371-391.

39. *Thin Film Thermocouples for High Temperature Measurement.* **Kreider, K.** s.l. : NIST, 1989.

40. **ASTM.** *The Use of Thermocouples in Temperature Measurement.* s.l. : ASTM, 1993.

41. *Eroding ribbon thermocouples: impulse response and transient heat flux analysis.* **Buttsworth, D, Stevens, R and Stone, C R.** s.l. : Measurement Science and Technology, 2005, Vols. 16, p. 1487-1494.

42. **Incropera, P F and DeWitt, D.** *Introduction to Heat Transfer.* s.l. : Wiley & Sons, 2002.

43. *Assessment of effective thermal product of surface junction thermocouples on millisecond and microsecond time scales.* **Buttsworth, D R.** s.l. : Experimental Thermal and Fluid Science, 2001, Vols. 25 p. 409-420.

44. *An experimental investigation of surface thermometry and heat flux.* **Jessen, C, Vetter, M and Gronig, H.** s.l. : Z. Flugwiss. Weltraumforsch., 1993, Vols. 17, p. 73-81.

45. *On the calibration of calorimeter heat-transfer gauges.* **Sprinks, T.** s.l. : AIAA Journal, 1963, Vols. 1, p. 464.

46. *Time constant measurement of thermocouple by use of modulated laser.* **Lina, H and al, et.** s.l. : Proceedings of SPIE - the international society for optical engineering , 2010, Vol. 7658 Issue.1 .

47. *Measurement Uncertainty Models.* **Dieck, R H.** No.1 pp. 29–35, s.l. : ISA Transactions, 1997, Vol. Vol. 36.

48. *Fundamentals of Measurement Error.* **Taylor, J L.** s.l. : Neff Instrument Corporation, 1988.

49. **ASME.** *Test Uncertainty, Instruments and Apparatus.* s.l. : ASME PTC, 1998.

50. *Manual on the Use of Thermocouples in Temperature Measurement.* Revision of Special Technical Publication (STP) 470B, s.l. : ASTM, 1993, Vols. Manual Series: MNL 12, Fourth Edition.

51. **Devices, Analog.** *Thermocouple Conditioner and Setpoint Controller, AD596*/AD597*.* 1998.

52. **Pallás-Areny, R and Webster, J.** *Sensors and Signal Conditioning, 2nd Ed.* s.l. : John-Wiley & Sons, Inc., 2000.

53. *Solutions to Fourier's equation and unsteady heat flow through structures.* **Davies, M G.** s.l. : Building and Environment, Elsevier Science, 1995, Vols. 30, no. 3 p. 309-321.

54. **Burden, R L and Faires, J D.** *Numerical Analysis.* s.l. : Brooks/Cole Publishing Co., New York, 6th Ed., 1997.

55. **Kreyszig, E.** *Advanced Engineering Mathematics.* s.l. : Wiley, New York, 7th Ed., 1993.

56. **Ames, W F.** *Numerical Methods for Partial Differential Equations.* s.l. : Academic Press, Inc. Boston, 3rd Ed., 1992.

57. **Burden, R L and Faires, J D.** *Numerical Analysis.* s.l. : Brooks-Cole Publishing Co., 1997.

58. **Isaacson, E and Keller, H B.** *Analysis of Numerical Methods.* s.l. : Dover, 1994.

59. **Cooper, J.** *Introduction to Partial differential Equations with Matlab.* s.l. : Birkhäuser, Boston, 1998.

60. **Morton, K W and Mayers, D F.** *Numerical Solution of Partial Differential Equations.* s.l. : Cambridge University Press, Cambridge, 1994.

61. **Sheskin, D J.** *Handbook of Parametric and Nonparametric Statistical Procedures.* s.l. : Chapman & Hall/CRC, 2007.

62. *Radiant Heat Transfer in Diesel Engines.* **Oguri, T and Inaba, S.** s.l. : SAE, Pap. no. 720023, 1972.

63. *Convective and radiative heat transfer in a high swirl direct injection engine.* **Dent, J C and Suliaman, S J.** s.l. : SAE pap. no. 770407, 1977.

64. *Thermal analysis of cylinder head carbon deposits from single cylinder diesel engine fueled by palm oil-diesel fuel emulsions.* **Husnawan, M and al., et.** s.l. : Applied Energy, 2009, Vols. 86, p. 2107-2113.

65. *Modeling Engine Heat Transfer and Flame-Wall Interaction.* **Nishiwaki, K.** s.l. : The 4th International Symposium COMODIA 98, 1998.

66. *Determination of Thermal Conductivity and Thermal Diffusivity of S.I. Engine Combustion Chamber DepositsProperties of .* **Hafnan, M and Nishiwaki, K.** s.l. : JSME Trans., 1995, Vols. 61, No. 589, p. 292-298.

67. *Unsteady Heat Transfer in Engines.* **Overbye, V D, Bennethum, J E, Uyehara, O A and Myers, P A.** s.l. : SAE, pap. no. 201C, 1961, Vols. 69, p. 461-494.

68. **Modest, M.** *Radiative Heat Transfer, 2nd Ed.* s.l. : Academic Press, Elsevier Science, 2003.

69. STAR-CD. [Online] CD-ADAPCO. http://www.cd-adapco.com/press_room/dynamics/27/flow_thermal_stress.html.

70. *Calculating transient wall heat flux from measurements of surface temperature.* **Reichelt, L, Meingast, U and Renz, U.** s.l. : International Journal of Heat and Mass Transfer, 2002, Vols. 45, p. 579-584.

71. *Thermal diffusivity/conductivity of magnesium oxide/silicon carbide composites.* **Luo, J and Stevens, R.** s.l. : J.Am. Ceram. Soc., 1997, Vols. 80, p. 699-704.

72. Engineering Fundamentals. [Online] November 2010. http://www.efunda.com/materials/elements/TC_Table.cfm?Element_ID=Cr.

73. Cambridge University - Department of Materials Science and Metallurgy. [Online] http://www.msm.cam.ac.uk/utc/thermocouple/pages/DriftInTypeKBareWiresThermocouples.html.

74. **Burley, N A.** *Solute depletion and thermo-E.M.F. drift in nickel-base thermocouple alloys.* 1969 : Journal of the Institute of Metals, 97 p. 252-254.

75. *Errors in thermoelectric thermometers.* **Fenton, A W.** s.l. : Proceedings of the Institution of the Electrical Engineers, 1969, Vols. 116, p. 1277-1285.

76. *Fine Wire Thermocouple Measurements of fluctuating Temperature.* **Ballantyne, A and Moss, J B.** 1977, Combustion Science and Technology, pp. 63-72.

77. **Ames, William F.** *Numerical Methods for Partial Differential Equations.* s.l. : Academic Press Inc. Boston, 1992.

78. **Moran, M J and Shapiro, H N.** *Fundamentals of Engineering Thermodynamics.* s.l. : John Wiley & Sons, 1998.

79. *High T.* **Kreider, K. and Gillen, G.**

80. *High Temperature Materials for Thin-Film Thermocouples on Silicon Wafers.* **Kreider, K. and Gillen, G.** 376, s.l. : Thin Solid Films, Elsevier, 2000.

81. *Effect of surface structural modification on absorptivity of gold in multi-pulse femtosecond laser ablation.* **Vorobyev, Y A et al.**

82. *A new phenomenological heat release model for thermodynamical simulation of modern turbocharged heavy duty Diesel engines.* **Tauzia, X. et al.** s.l. : Applied Thermal Engineering 26 (2006) 1851–1857, 2006.

83. *Accurate prediction of the rate of heat release in a modern direct injection diesel engine.* **Lakshminarayanan, P A et al.** s.l. : Proc Instn Mech Engrs Vol 216 Part D: J Automobile Engineering, 2002.

84. *Soot and fueldistributions in a D.I. diesel engine via 2-D imaging.* **Dec, J and Espey, C.** s.l. : SAE Transactions, 2001, Vol. Vol. 101.

85. *Design and operation of a high pressure, high temperature cell for HD diesel spray diagnostics: guidelines and results,.* **Baert, R, et al.** s.l. : SAE International, 2009.

86. *Visualization of Diesel Spray Penetration, Cool-Flame, Ignition, High-Temperature Combustion, and Soot Formation Using High-Speed Imaging.* **Pickett, L.M, Kook, S and and Williams, T.C.** s.l. : SAE Int. J. Engines, 2009, Vols. 2:439-459.

87. *Determination of the time constant of fine-wire thermocouples for compensated temperature measurements in premixed turbulent flames.* **Miles, P C and Gouldin, F C.** s.l. : Combust. Sci. Tech., 1992, Vols. 83:1-19.

88. *Frequency response of fine-wire thermocouple.* **Petit, C, et al.** s.l. : J. Phys. E: Sci. Instrum., 1982, Vol. 15:760.

89. *Thermocouple and sample probes for combustion studies.* **Heitor, M V and Moreira, A L N.** s.l. : Prog. Energy Combust. Sci., 1993, Vols. 19:259-278.

90. *Influence of temperature on the frequency response of fine-wire thermocouples over the range (300 K-800 K) in airflows.* **Dupont, A, et al.** s.l. : J. Phys. E: Sci. Instrum., 1984, Vols. 17:808-812.

91. *Visualization of Diesel Spray Penetration, Cool-Flame, Ignition, High-Temperature Combustion, and Soot Formation Using High-Speed Imaging.* **Pickett, L M, Kook, S and Williams, T C.** s.l. : SAE Int. J. Engines , 2009, Vols. 2:439-459.

92. *Schlieren and Shadowgraph Techniques.* **Settles, G S.** s.l. : Springer-Verlag, 2001.

93. **Fletcher, C A J.** *Computational Techniques for Fluid Dynamics.* s.l. : Springer-Verlag, Berlin, 1988.

94. **Golub, G and Ortega, J M.** *Scientific Computing: An Introduction with Parallel Computing.* s.l. : Academic Press Inc., Boston, 1993.

95. **Hoffman, J D.** *Numerical Methods for Engineers and Scientists.* s.l. : McGraw-Hill, New York, 1992.

96. **Isaacson, E and Keller, H B.** *Analysis of Numerical Methods.* s.l. : Dover, New York, 1994.

97. *Three-dimensional simulation of the coupled convective, conductive, and radiative heat transfer during decay heat removal in an HTR.* **Simoneau, J P, et al.** 15-17, s.l. : Nuclear Engineering and Design, 2007, Vols. 237, p. 1923-1937.

98. **Engineers, US Army Corps of.** Engineering and Design - Lubricants and Hydraulic Fluids. *Publication Number: EM 1110-2-1424.* [Online] 1999. http://140.194.76.129/publications/eng-manuals/em1110-2-1424/.

99. *Notes on the Thermal Conductivities of Graphite and Amorphous Carbon.* **Mizushima, S and Okada, J.** 1, s.l. : Physical Review, 1951, Vol. 82.

100. *Lubricant thermal conductivity heat capacity under high pressure.* **Larsson, P.** s.l. : Proceedings of the Institution of Mechanical Engineers, Part J, Journal of engineering tribology, 2000, Vol. 214.

101. *Experimental Determination of Spontanous Diesel Flame Emission Spectra in a Large Diesel Engine Operated with Different Diesel Fuel Qualities.* **Vattulainen, J, Hernberg, R and Kytölä, J.** s.l. : SAE Technical Papers Series 981380, 1998.

102. **Barber, P W and Hill, S S.** *Light Scattering by Particles: Computational Methods, 1. Ed.* s.l. : World Scientific, Singapore, 1990.

Appendix I: Laplace transformation approach

In the chapter 3 we saw how the unsteady one-dimensional heat conduction equation could be solved using a series of trigonometric functions. Another possibility of solving the equation analytically is by the application of Laplace transformation (see [70]). In this situation it is more convenient to work with a non-dimensional form of eq. (0.6):

$$\frac{\partial\theta(x,t)}{\partial\tau} = \frac{\partial^2\theta(x,t)}{\partial\xi^2} \qquad 0 \le x \le L, \;\; \tau \ge 0 \tag{0.31}$$

Where the dimensionless time and dimensionless distance is given by:

$$\tau = \frac{t\alpha}{\delta^2} \quad \wedge \quad \xi = \frac{x}{\delta} \tag{0.32}$$

Furthermore, the temperature is described by the difference of the steady and transient temperature:

$$\theta(x,t) = v(x,t) - v_\delta \tag{0.33}$$

Assuming a constant temperature v_δ at the position $x = \delta$ and a known initial temperature distribution, the boundary conditions are defined as:

$$\theta(0,t) = v_S \; - v_\delta = \theta_S(t) \;\wedge\; \theta(1,t) = 0 \tag{0.34}$$

The mathematical derivation of the solution to eq. (0.31) using the Laplace transformation is quite long and complex and does not itself provide as much insight

to the physical aspects of the problem along the way. The derivation can be found in [70]. The instantaneous surface heat flux solution as a function of time $\tau_i = i \cdot \Delta\tau$ is:

$$\frac{dq(\tau_i)}{dt} = 2\frac{k}{\delta}\sqrt{\frac{\Delta\tau}{\pi}}\sum_{j=0}^{i-1}\left(\left(\nu'_{S,j} + \nu''_{S,j}\cdot\Delta\tau\left(i - \frac{2j+1}{2}\right)\right)\cdot R_{i,j} - \nu''_{S,j}\frac{\Delta\tau}{3}S_{i,j}\right) \tag{0.35}$$

Where the first and second order temperature gradients are given by:

$$\nu'_{S,j} = \frac{\nu_{S,j+1} - \nu_{S,j}}{\Delta\tau} \quad \wedge \quad \nu''_{S,j} = \frac{\nu_{S,j+2} - \nu_{S,j+1} - (\nu_{S,j} - \nu_{S,j-1})}{2(\Delta\tau)^2} \tag{0.36}$$

The summation constants are defined as:

$$R_{i,j} = \sqrt{i-j} - \sqrt{i-j-1} \quad \wedge \quad S_{i,j} = (i-j)^{\frac{3}{2}} - (i-j-1)^{\frac{3}{2}} \tag{0.37}$$

Notice that since the dimensionless time step $\Delta\tau$ is proportional to δ^{-2} and $\nu'_{S,j}$ and $\nu''_{S,j}\cdot\Delta\tau$ is proportional to δ^2, the instantaneous surface heat flux is not dependent on δ, as one could be led to believe due to the presence of δ in the prefactor on the RHS of eq. (0.35). The most noticeable difference between eq. (0.35) and eq. (0.15) is the direct dependence of the first and second order derivatives of the temperature in eq. (0.35). It is evident that large fluctuations in the measured temperature values can have a huge impact on the solution, and thus reducing the noise is of utmost importance. A way to avoid this could be to ensemble average the data by superimposing a number of temperature traces from different engine cycles at the same operating conditions and dividing by the total number of cycles in the

ensemble. This method is effective to reduce random uncertainties like e.g. 50 Hz noise. The application of digital low-pass filters and notch filters to the measured data before further heat transfer analysis can also be considered a useful option.

Comparison with exact analytical solution

A good way to test how well the solution (eq. (0.35)) predicts the instantaneous surface heat flux is to compare it with a hypothetic scenario which has a known analytical exact solution. Consider a semi-infinite body with a surface temperature defined as:

$$v_S(t) = \overline{v_S} + \Delta v \sin(2\pi t f) \tag{0.38}$$

Where f is the frequency, $\overline{v_S}$ is the average surface temperature and Δv the amplitude of the surface temperature oscillations. The exact analytical solution to eq. (0.14) with the surface temperature defined in eq. (0.38) is given by:

$$\frac{dq(t)}{dt} = k\Delta v \sqrt{\frac{\pi f}{\alpha}} (\sin(2\pi t f) + \cos(2\pi t f)) \tag{0.39}$$

Choosing the following realistic values: $f = 3\,\mathrm{kHz}$, $\alpha = 3.6 \cdot 10^{-6}\ \frac{\mathrm{m}^2}{\mathrm{s}}$ and $k = 15.7\,\frac{\mathrm{W}}{\mathrm{mK}}$ (for Nichrome at 650 K, see [42]) the comparison of the exact solution eq. (0.39) and the solution obtained in the previous section (eq. (0.35)) is shown in fig. 4.

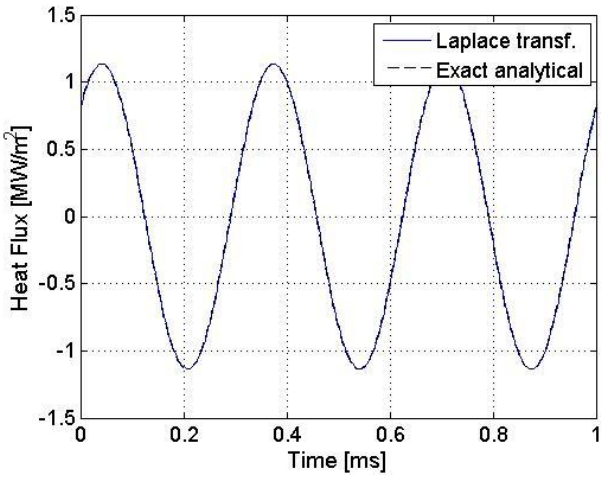

Figure 50: Comparison of the Laplace solution with the exact analytical solution.

The special case shown in Figure 50 suggests that the solution method based on the Laplace transform is performing very well for the prediction of surface heat flux in an engine type application. Additional calculations were carried out, following the same comparative methodology, to investigate the frequency domain from 1 Hz to 3 kHz. Of the 100 different discrete frequencies analyzed, no break down or significant deviations were found. The only peculiar thing that was observed was a slight deviation of the solution at the first couple of time steps (also reported in [70]). However, this deviation is very small and has no significant impact on the solution. For the case shown in fig. 1 the initial deviation was 0.022 $\frac{\mathrm{MW}}{\mathrm{m}^2}$ corresponding to an error of less than 5% (even too small to see on the figure). After a short settling time of around 3 μs the error is diminished to less than 0.1 %.

This special case of a sinusoidal temperature variation at the surface is of course not the situation in a real engine. However, it builds some confidence in the usefulness of the method since it was successfully applied to a case very similar in nature to the engine heat flux scenario.

Appendix II: Material Properties

Linear and quadratic fits of thermal conductivities, specific heat capacities and thermal diffusivities have been computed for various materials:

Material	Reference
Nichrome	[42]
Chromel	[43], [26]
Alumel	[43], [26]
Inconel	[42]
Magnesium Oxide	[71]
Gold	[42]
Chromium	[72]

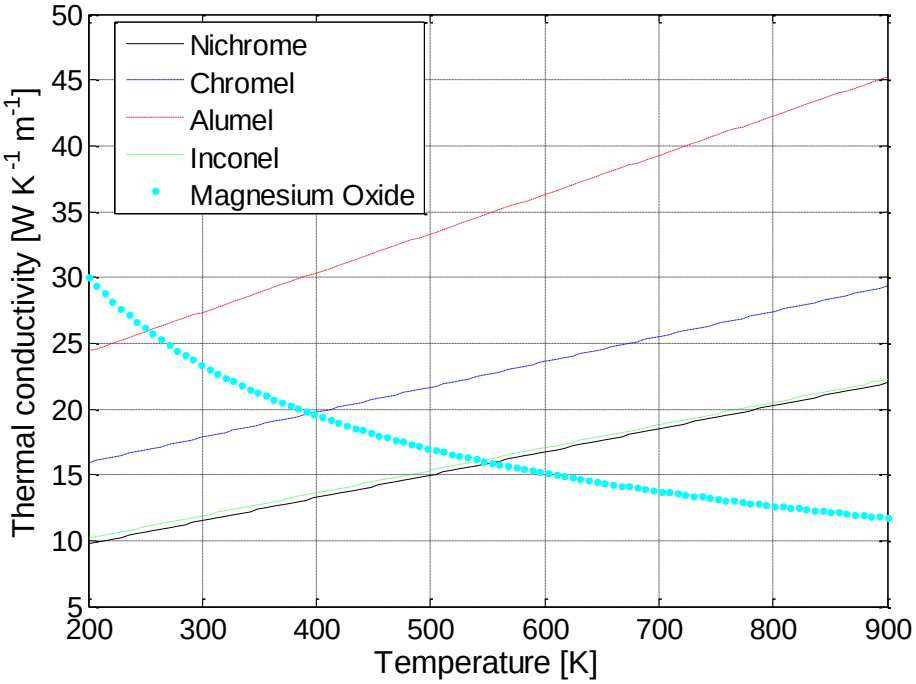

Figure 51: Thermal conductivity for various materials.

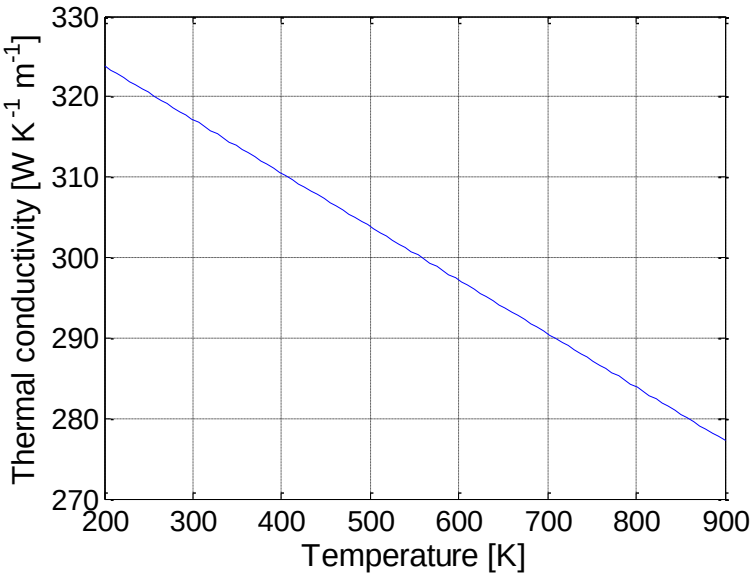

Figure 52: Thermal conductivity for Au.

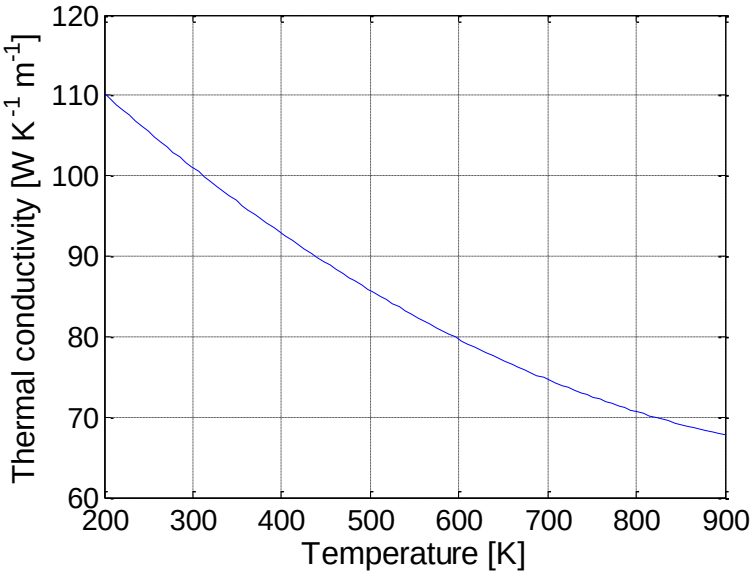

Figure 53: Thermal conductivity for Cr.

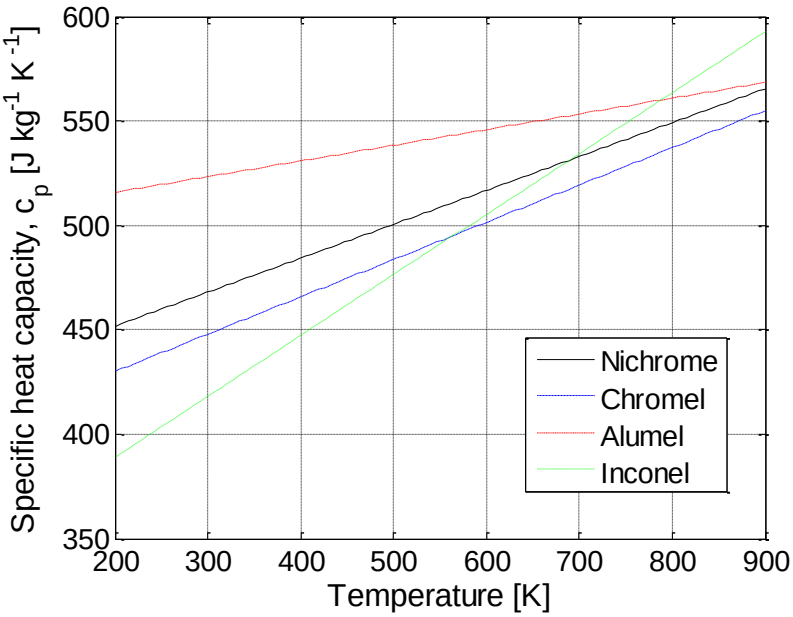

Figure 55: Specific heat capacity for varoius materials.

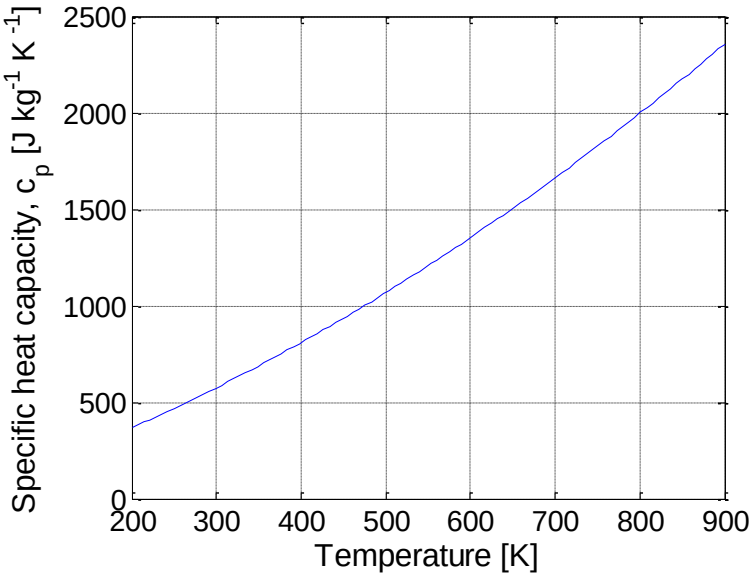

Figure 54: Specific heat capacity for MgO.

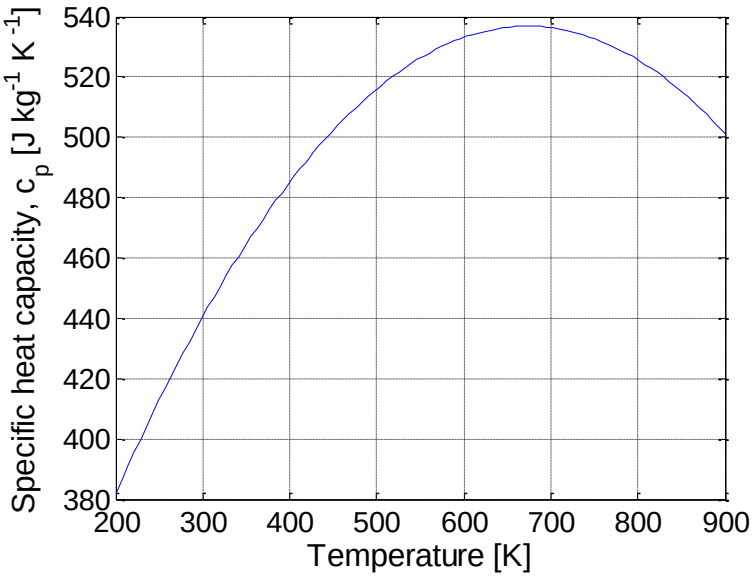

Figure 56: Specific heat capacity for Cr.

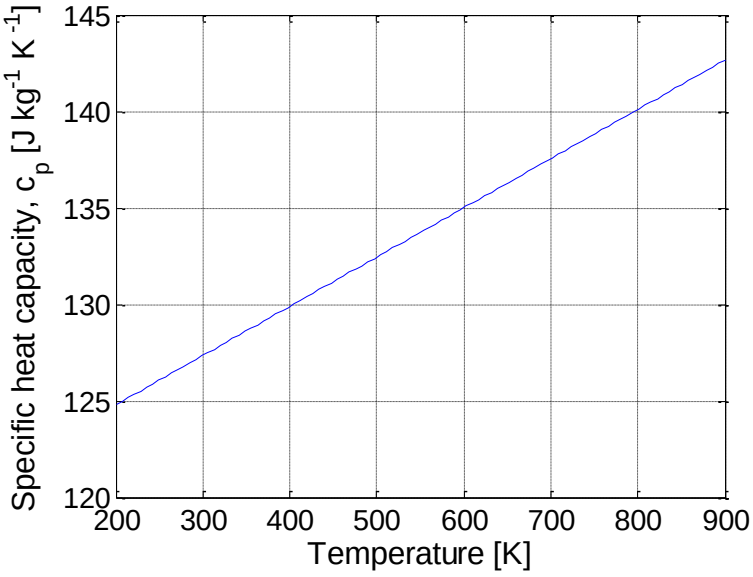

Figure 57: Specific heat capacity for Au.

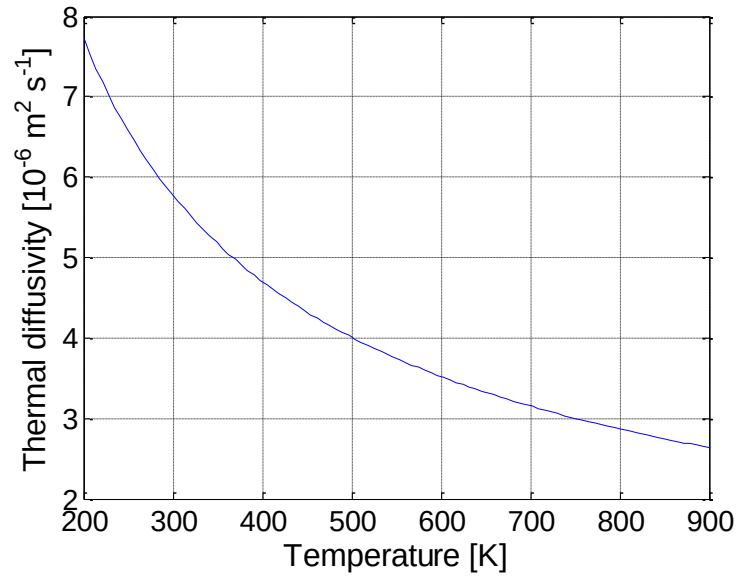

Figure 58: Thermal diffusivity for MgO.

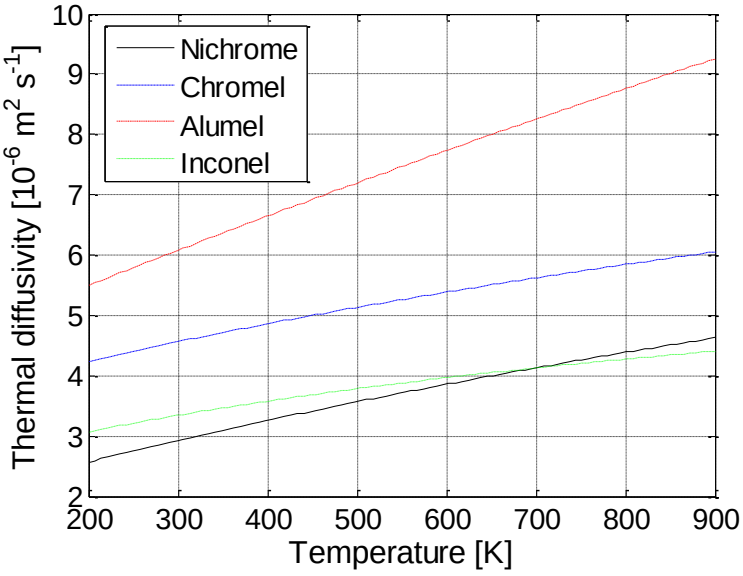

Figure 59: Thermal diffusivity for various materials.

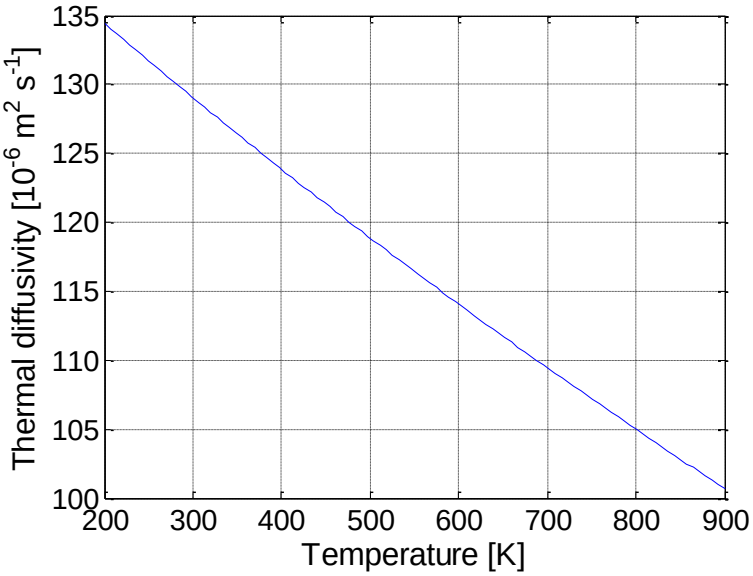

Figure 61: Thermal diffusivity for Au.

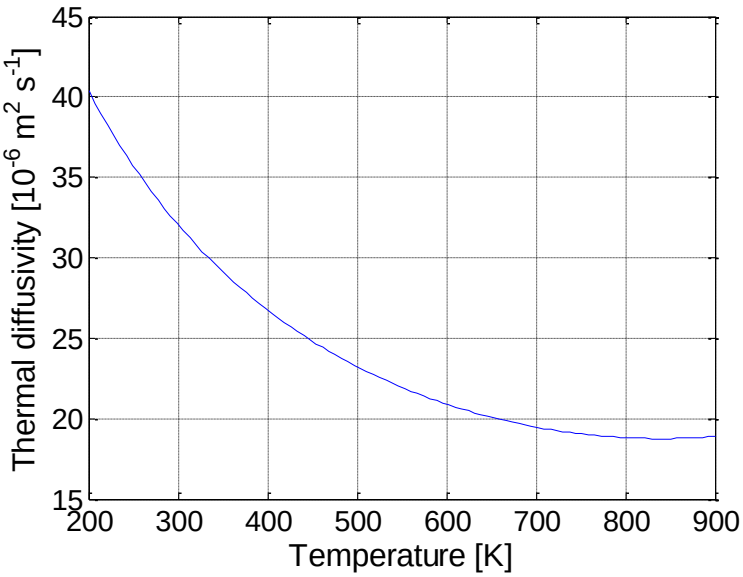

Figure 60: Thermal diffusivity for Cr.

Appendix III: Thermocouple drift

Thermocouple drift is mainly caused by a change in material composition comprising the thermocouple, e.g. by oxidation [73]. In the figures below are shown the depletion of Chrome and the short range order transformation of Chromel which are some of the most limiting factors with regard to drift. Note that for short hours of operation the Seebeck coefficient is not changed appreciably in the temperature range of 400-900 K for the time spans considered.

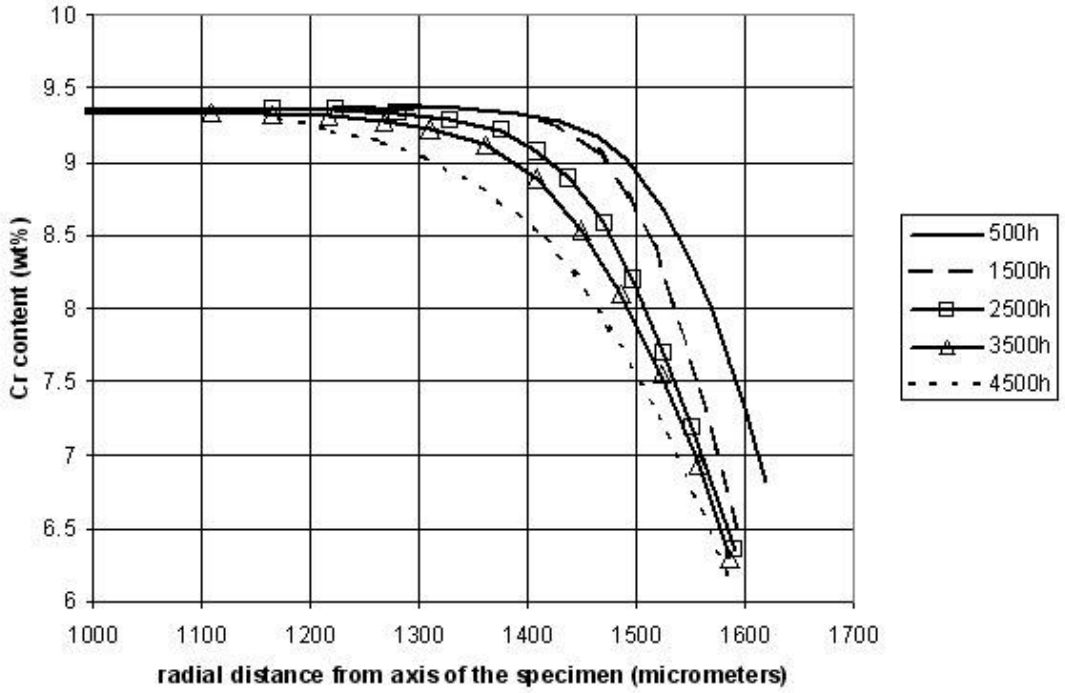

Figure 62: Cr depletion in a Chromel wire as a result of oxidation in air. (Data from [74])

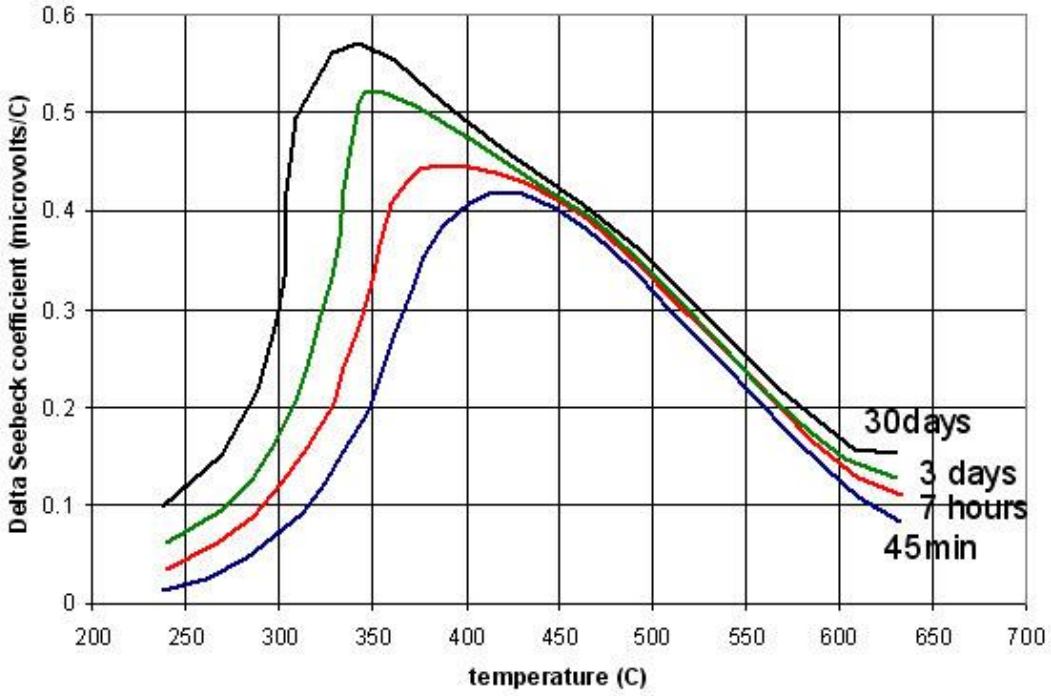

Figure 63: Short range order transformation in Chromel [75].

Appendix IV: Paper I

Proceedings of the ASME 2012 Internal Combustion Engine Division Fall Technical Conference
ICEF2012
September 23-26, 2012, Vancouver, BC, Canada

ICEF2012-92076

SIMULTANOUS TRANSIENT SURFACE TEMPERATURE AND HEAT FLUX MEASUREMENTS IN A LARGE BORE TWO-STROKE DIESEL ENGINE

Caspar Ask Christiansen
Technical University of Denmark,
Kgs. Lyngby, Denmark

Stefan Mayer
MAN Diesel & Turbo SE
Copenhagen, Denmark

Jesper Schramm
Technical University of Denmark,
Kgs. Lyngby, Denmark

ABSTRACT

Surface temperature measurements were performed in a large bore two-stroke diesel engine used for ship propulsion. A specially designed fast-response surface thermocouple was used together with an embedded standard K-type thermocouple to measure surface temperature and heat flux with high temporal resolution.

Heat flux calculations were carried out both analytically and numerically showing good agreement between the results. Measurements were carried out at three different engine load conditions (25%, 30% and 50% load) in one of the fuel atomizers in the cylinder head. Cyclic surface temperature variations of up to approximately 80 K with a peak temperature of 860 K were observed.

The magnitude of the perturbation of the temperature field due to the presence of the thermocouples was investigated by three dimensional CFD simulations.

INTRODUCTION

In recent years, there has been an increased focus on environmental issues especially with regard to CO_2 emissions. In the context of internal combustion engines examples of such hazardous emissions are sulphur oxides (SOx) and nitrous oxides (NOx). Since the vast majority of the worlds goods are transported around the globe by means of large container ships it is clear that these contribute in large part to the total amount of human-caused emissions. Thus, even small improvements in the efficiency and engine operating conditions will have a significant impact on both fuel consumption and emissions.

Since it is extremely costly to build engines just for test purposes, the recent year's progress in computer technology and software simulation tools has opened a possibility for simulating and predicting the performance of new engine designs and concepts. However, experimental validation is very important to test new models describing e.g. fluid flows, combustion and heat transfer mechanisms in the engine. An especially important factor in this context is the knowledge of temperature distributions in and around the combustion chamber. Temperature gradients are what drives the heat transfer and play a big role in the reaction kinetics in the gases primarily during and shortly after the combustion. All these are factors that affect the engine performance and emission level.

However, the information available from the literature is very limited when it comes to measured surface temperature in large bore two-stroke diesel engines [1] and is typically not directly measured but derived from sub-surface measurement locations [2]. Measuring below the surface often has the advantage of easier instrumentation using commercial available off the shelf equipment but lacks in the level of detail of the true instantaneous surface temperature and heat transfer. This is due to the dampening of the surface temperature signal by the wall material between the thermocouple hot junction and the in-cylinder surface to a level where the signal to noise ratio becomes too low to capture the smallest fluctuations.

Fortunately, there has been significant progress in the automotive industry within the field of heat transfer in the last couple of decades. As a result, a lot of valuable information exists in the literature with regard to temperature measurement techniques and data acquisition systems for small engines (see e.g. [1], [3] and [4]). However, since pressures and

temperatures often reach higher values in the large engines, it is not obvious if the measuring equipment used in small engine research can withstand the tough thermo physical conditions of the large engines. Furthermore, it is not unlikely that the significantly different timescales, geometry etc. which are influencing the nature of the heat transfer in the large engines can result in some effects not present, or at least of the same importance, as in the small engines.
In this work, a special designed thermocouple is presented for measuring the dynamic surface temperature. The sensor is tested at different part load conditions in a MAN Diesel & Turbo SE test engine.

EXPERIMENTAL SETUP

A four cylinder uni-flow scavenge two-stroke diesel engine of the type 4T50ME-X was used in this study. The engine was originally build for ship propulsion but is now used as a test engine at the MAN Diesel and Turbo SE facilities in Copenhagen, Denmark. The engine specifications are given in Table 1.

Table 1: Engine Specifications

Cycle	Two-stroke
No. of cylinders	4
Bore, [m]	0.50
Stroke, [m]	2.20
Max. power, [MW]	8
Max. speed, [rpm]	123
Max. pressure, [bar]	200

Surface temperature was measured with a modified standard K-type thermocouple with a pair wire configuration [1]. This was done by drilling a hole through a spray atomizer dummy and mounting the thermocouple through the hole in a way so that the thermocouple hot junction was protruding from the surface. A spray atomizer dummy is essentially a spray atomizer but without any fuel nozzles, i.e. a solid body. Furthermore, the length of the atomizer dummy was adjusted so it was flush with the inner surface of the cylinder head when mounted in the fuel injector. Afterwards, the thermocouple was cut off flush with the surface of the atomizer dummy and a 0.5 mu layer of chrome and a 0.5 layer of gold were then deposited in a Chemical Vapor Deposition chamber. The fabrication steps are shown in Figure 1.

The chrome layer serves as an adhesive and conducting layer whereas the gold layer prevents oxidation of the newly created hot junction.

The location of the atomizer dummy mounted with the surface temperature thermocouple is shown in Figure 2.

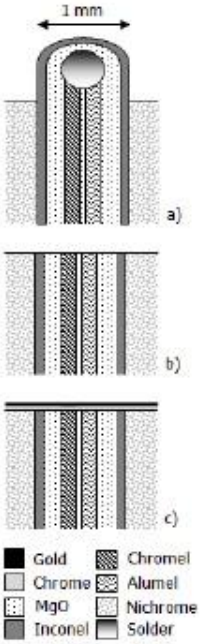

Figure 2: Sketch showing the steps involved in the fabrication process of the surface temperature thermocouple: a) Thermocouple mounted in the nichrome atomizer dummy b) Thermocouple hot junction is cut off flush with the surface c) deposition of chrome and gold

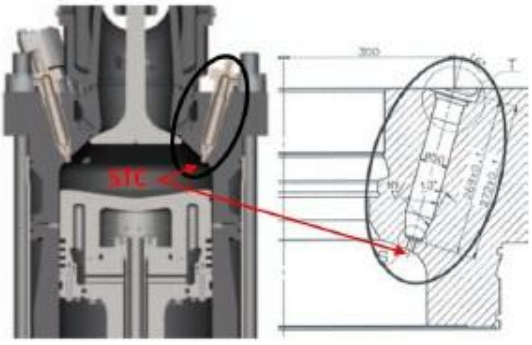

Figure 1: To the left is shown a sketch of the engine cylinder cross-section and the location of the surface thermocouple (STC). The picture to the right shows a zoom in on the fuel injector.

A second K-type thermocouple was mounted 1.5 mm beneath the surface and 2 mm off axis from the surface thermocouple.

A custom made signal conditioner based on the Analog Devices monolithic amplifier AD597A was used for amplification of the thermocouple outputs. The amplifier had a built in cold junction compensation pretrimmed for K-type thermocouples and a cut off frequency around 10 kHz. The extension cables and the signal conditioner box were electrically shielded to reduce noise. Furthermore, each thermocouple had a separate amplifier with a separate 9 V DC voltage supply to reduce noise.

The data acquisition system used in all the experiments was controlled through a custom made program build in LabView and a shaft encoder to determine the crankshaft position.

Thermocouple Response Test

The response time of the STC was tested prior to the engine experiments following the procedure described in [5,6]. The technique is called the water droplet response test and is suited for proving response times down to around 0.1 ms. The basic principle of the test is to release a water droplet at room temperature and let it impact on the hot junction of the STC which is initially at 373 K. During impact the hot junction and the water droplet will reach a quasi equilibrium state with a temperature of around 358.5 K. The temperature of the STC is shown in Figure 3 around the time of impact.

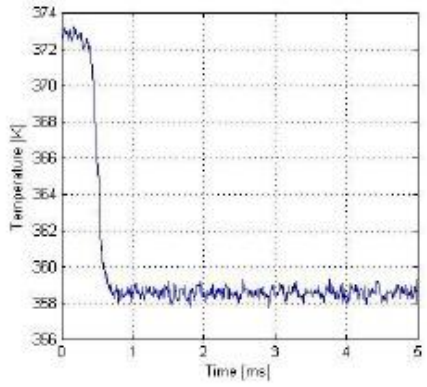

Figure 3: STC response test. The graph shows the temperature of the hot junction as a function of time around the time when the water drop impacts on the STC

The response time of the STC is around 0.1 ms which is more than sufficient for the engine tests.

Surface Heat Flux Computation

Two different approaches were used to calculate the surface heat flux from the measured temperatures in order to validate the computation routine. However, both models are relying on the 1D assumption and hence are not taken into account any 3D effects that might be present due to nonuniformity in the material properties and the geometry of the STC.

The first method is the widely used analytical solution to the 1D unsteady heat conduction problem of a semi-infinite body utilizing Fourier series [7,8], leading to the surface heat flux given by:

$$q_s''(t) = \frac{k}{L}(\bar{T}_s - \bar{T}_b) + k\sum_{n=1}^{N}\sqrt{\frac{n\omega}{2\alpha}}[A_n\cos(n\omega t) + B_n\sin(n\omega t)] \quad (1)$$

with the two boundary conditions:

$$T(x\to\infty) = \bar{T}_b \quad \wedge \quad T(x=0,t) = T_s(t) \quad (2)$$

The first term on the right hand side of equation (1) is the steady heat flux contribution which depends on the average surface temperature and the average bulk temperature measurement. The second term is the unsteady heat flux contribution determined from the time-varying surface temperature.

The second model used for computing the surface heat flux is a numerical approach based on finite differences in a Crank-Nicholson time scheme [9,10]. In this model the surface node of the 1D mesh is reflecting the measured surface temperature trace and the backside node is the measured bulk temperature 1.5 mm below the surface. After a certain number of iterations a cyclic steady state solution is reached and the routine is stopped. The time-varying surface heat flux can then be computed on the basis of the obtained temperatures at the node just below the surface and the surface node.

RESULTS

Surface Temperature Measurements

Surface temperatures were measured at three different load and speed conditions: 25% (77 rpm), 30% (82 rpm) and 50% (97 rpm). 500 consecutive cycles were recorded at each load case and then ensemble averaged. The results are shown in Figure 4 along with the in-cylinder pressure in arbitrary units.

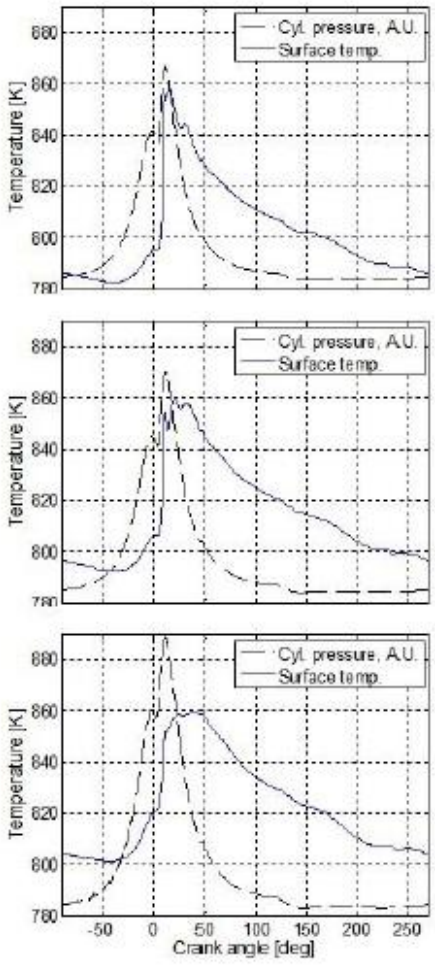

Figure 4: Measured surface temperature for three different load and speed conditions. Top: 25% (77 rpm), middle: 30% (82 rpm) and bottom: 50% (97 rpm). TDC is at 0 crank angle degrees.

It is clear that the surface temperature and cylinder pressure increase during the compression stroke and reaches a local maximum just around top dead center (TDC). At the onset of combustion shortly after both the cylinder pressure and the surface temperature rise very fast and reaches a peak value. The peak temperature is almost the same in all three cases whereas the temperature variation is decreasing with increasing engine speed and load. Usually, an increase in load at a fixed speed would lead to a higher peak temperature of the gas and flame temperature and thus result in a larger temperature variation. However, when the engine speed is increased the time available for transferring heat between gas and wall is decreased and results in a decrease in temperature variation.

It is not clear why the peak temperature is more or less unaffected by the variation in speed and load. It is possible that the aforementioned two effects counter each other. Another effect that could influence the peak temperature is the amount of deposits on the surface of the STC which would most likely vary with load. A thicker deposit layer will act as a thermal insulator and lower the peak temperature registered by the STC.

After the onset of combustion it is clearly seen that the surface temperature stays at a high value for a longer part of the cycle when the load is increased. This is also expected since the amount of fuel injected and the injection period is increasing with an increase in load.

It is interesting to note that a small change in surface temperature is observed at the time of exhaust valve opening (starting at 120 CA) and at the time where the scavenging ports are opened (starting at 140 CA). Furthermore, a bump in the temperature trace is also observed around the time of exhaust valve closing and intake port closing (starting at 220 CA).

Surface Heat Flux

The surface heat flux was computed using both an analytical and numerical approach yielding identical results. The computed surface heat flux is shown in Figure 5 for all three load conditions at the time around combustion.

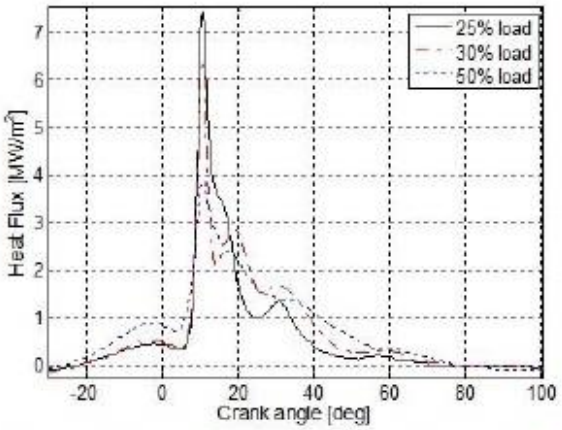

Figure 5: Surface heat flux for three different load conditions.

During the compression stroke the surface heat flux is positive and increasing. The flux is highest for the high load condition and lowest for the low load condition at this point in the cycle. In the time period between TDC and start of combustion the surface heat flux is slightly decreasing. At the start of combustion a steep rise in the surface heat flux is observed reaching the peak surface heat flux value shortly after. The peak values are highly dependent on the load ranging from 3.9 $\frac{MW}{m^2}$ at 50% load up to 6.3 $\frac{MW}{m^2}$ at 30% load and 7.4 $\frac{MW}{m^2}$ at 25% load. The mechanisms causing this trend are not clear. From a literature review of research related to heat transfer in small engines it seems that the majority of studies show the opposite trend, i.e. that the peak surface heat flux is increasing with an increase in load [1]. However, some studies also show the trend observed in this study [11]. A possible explanation for this trend could be that the amount of deposit on the surface of the STC hot junction changes with load as discussed briefly in the preceding section. Furthermore, it is important to remember that the surface heat flux is only measured at one location and is thus not necessarily representative for the peak surface heat flux in general.

The mean surface heat flux was found to be: 99 $\frac{kW}{m^2}$ at 25% load, 105 $\frac{kW}{m^2}$ at 30% load and 111 $\frac{kW}{m^2}$ at 50% load. These are relatively low mean heat flux values compared to other reported values for engines similar in size where values are up to four times higher [2]. This could indicate that the cooling of the backside of the atomizer is low. The measured high surface temperature values support this theory. Normally, there is a certain cooling effect from the fuel when it is injected through the nozzles. In these tests the whole fuel supply was demounted for the atomizer with the STC and the backside of the solid atomizer was only cooled by natural convection.

DISCUSSION: TEMPERATURE PERTURBATION

The presence of the thermocouples introduces nonuniformity in the material properties in and around the thermocouples. This leads to a perturbation of the original temperature field in the atomizer dummy which can result in erroneous results. To investigate the magnitude of this perturbation and how it affects the temperature reading at the location of the thermocouple hot junctions a numerical solution to the heat conduction problem was carried out by means of the commercial Finite Volume Solver StarCD for two distinct cases.

In both cases a polyhedral 3D mesh consisting of approximately 300,000 nodes was constructed around the location of the thermocouples. In the first case the material properties for the atomizer dummy and the thermocouples were used and only one half of the cylindrical atomizer was modeled to reduce computational time. The latter was done by cutting the cylinder in half at the symmetry plane so that no information was lost. Symmetry plane boundary conditions were imposed at all boundaries except at the surface with the

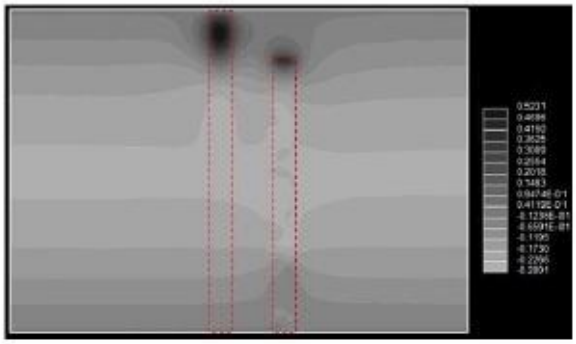

Figure 6: Result of 3D numerical simulations at the time of highest temperature field perturbation. A cross-section (at the symmetry plane) of the atomizer dummy with the two mounted thermocouples is shown. The grey tone scale unit is in K. The red dashed squares show the location of the thermocouples.

STC hot junction. At this boundary the measured transient surface temperature was used. Cyclic steady state was assured before the simulation stopped (after 40 engine cycles).

Mesh independency was assured by carrying out simulations with a coarser mesh (fewer nodes) showing no change in the result.

In the second case the mesh and the procedure was identical to the first case but only the material properties for the atomizer material were used so that the temperature field in the absence of thermocouples was computed.

The two results computed for each case were then subtracted giving the local temperature perturbations. The point in the cycle where the perturbation was highest was identified at the time slightly after the start of combustion. The result is shown in Figure 6.

The maximum value of the temperature perturbation can be seen on the grayscale next to the simulation result. The temperature perturbation is highest at the location of the BTC hot junction with a value around 0.5 K. At the location of the STC hot junction the temperature perturbation is around 0.2 K. A comparison with these values to the estimated total measurement uncertainty of a class one K-type thermocouple of around 2.5 K shows that they are significant contributions to the overall uncertainty although not the major source.

It is worth noting that is unlikely that the imposed boundary condition at the top surface is reflecting the true surface temperature of both the STC hot junction and the atomizer surface. In reality there would probably be a slight temperature difference across the surface and thus the temperature perturbation might also be slightly higher than 0.2 K reported here.

CONCLUSIONS

Transient surface temperature and heat flux measurements were carried out on a large two-stroke diesel engine at the location of an atomizer in the cylinder head. Three different load and speed conditions were studied.

The surface temperature measurements showed temperature variations in the range of 60-80 K. The temperature variation was found to decrease with an increase in engine load and speed. The peak temperature was around 860 K and did not change significantly when the load and speed was varied.

Surface heat flux was computed using both an analytical and a numerical solution to the 1D semi-infinite unsteady heat conduction problem giving identical results.

The peak surface heat flux was found to decrease with an increase in load and speed which is in contrast to what is usually observed in small engines. However, it is important to remember that measurements were only carried out at one location in the engine and thus not necessarily representative for the peak surface heat flux in general.

The mean surface heat flux was found to increase with load and speed which is in agreement with most other studies on both small and large bore engines.

Finally, the perturbation of the temperature field around the location of the thermocouple hot junctions was investigated by means of 3D numerical simulation using finite volumes. The simulation results showed that the presence of the thermocouples result in a measurement uncertainty up to around 0.5 K.

NOMENCLATURE

1D	one dimensional
3D	three dimensional
α	thermal diffusivity (m^2/s)
A_n	Fourier cosine series coefficient
B_n	Fourier sine series coefficient
BTC	embedded thermocouple
k	thermal conductivity (W/m K)
L	BTC distance from surface (m)
N	number of harmonics
$q_s''(t)$	surface heat flux (W/m^2)
rpm	revolutions per minute
STC	surface temperature thermocouple
t	time (s)
$\bar{T}_s$	average surface temperature (K)
$\bar{T}_b$	average BTC temperature (K)
x	surface normal coordinate direction
ω	angular velocity (1/s)

REFERENCES

[1] Borman, G. and Nishiwaki, K., 1987, "Internal-Combustion Engine Heat Transfer", Prog Energy Combust Sci, Vol. 13, p. 1-46.

[2] Boulouchos, K. ., Eberle, M., Ineichen, B., and Klukowski, C., 1989, "New Insights into the Mechanisms of In-Cylinder Heat Transfer In Diesel Engines", SAE Technical Paper 890573.

[3] Suzuki, Y., Shimano, K., Enomoto, Y., Emi, M., Yamada, Y., 2005, "Direct heat loss to combustion chamber walls in a direct-injection diesel engine: evaluation of direct heat loss to piston and cylinder head", International Journal of Engine Research, Vol. 6, p. 119-135.

[4] Enomoto, Y., Ohya, T., Ishii, M., Enomoto, K., Kitahara, N., 1992, "Study on analysis of instantanous heat flux flowing into the combustion chamber wall of an internal combustion engine - examination in the case of consideration of heat storage term and the temperature dependency of the thermocouples thermophysical properties", JSME International Journal Series B, 1992, Vol. 35, p. 608-615.

[5] Buttsworth, D., Stevens, R. and Stone, C. R., 2005, "Eroding ribbon thermocouples: impulse response and transient heat flux analysis", Measurement Science and Technology, Vol. 16, p. 1487-1494.

[6] Buttsworth, D., 2001, "Assessment of effective thermal product of surface junction thermocouples on millisecond and microsecond time scales", Experimental Thermal and Fluid Science, Vol. 25, p. 409-420.

[7] Overbye, V.D., Bennethum, J.E., Uyehara, O. A. and Myers, P. A., 1961, "Unsteady Heat Transfer in Engine", SAE, pap. no. 201C, Vol. 69, p. 461-494.

[8] Beck, J. V., Blackwell, B., St. Clair, C. R., 1985, "Inverse Heat Conduction: Ill-Posed Problems", Wiley Interscience, New York.

[9] Ames, W. F., 1992, "Numerical Methods for Partial Differential Equations", Academic Press Inc., Boston, 3rd Ed.

[10] Morton, K. W. and Mayers, D. F., 1994, "Numerical Solution of Partial Differential Equations", Cambridge University Press, Cambridge.

[11] Dent, J. C. and Suliaman, S. J., 1977, "Convective and radiative heat transfer in a high swirl direct injection engine", SAE pap. no. 770407.

Appendix V: Paper II

SAE International

2010-01-2106
Published
10/25/2010

Comparison of Diesel Spray Combustion in Different High-Temperature, High-Pressure Facilities

Lyle M. Pickett and Caroline L. Genzale
Sandia National Laboratories

Gilles Bruneaux, Louis-Marie Malbec and Laurent Hermant
IFP

Caspar Christiansen and Jesper Schramm
Technical Univ. of Denmark

ABSTRACT

Diesel spray experimentation at controlled high-temperature and high-pressure conditions is intended to provide a more fundamental understanding of diesel combustion than can be achieved in engine experiments. This level of understanding is needed to develop the high-fidelity multi-scale CFD models that will be used to optimize future engine designs. Several spray chamber facilities capable of high-temperature, high-pressure conditions typical of engine combustion have been developed, but because of the uniqueness of each facility, there are uncertainties about their operation. For this paper, we describe results from comparative studies using constant-volume vessels at Sandia National Laboratories and IFP. Targeting the same ambient gas conditions (900 K, 60 bar, 22.8 kg/m ^{3} , 15% oxygen) and using the same injector specifications (common rail, 1500 bar, KS 1.5/86 nozzle, 0.090 mm orifice diameter, n-dodecane, 363 K), we describe detailed measurements of the temperature and pressure boundary conditions at each facility, followed by observations of spray penetration, ignition, and combustion using high-speed imaging. The spray diagnostics show reasonable similarity despite the challenges of providing matched boundary conditions at these unique facilities. Performing experiments at the same high-temperature, high-pressure operating conditions is an objective of the Engine Combustion Network (http://www.ca.sandia.gov/ECN/), which seeks to leverage the research capabilities and advanced diagnostics of all participants in the ECN. Thus, in addition to the presentation of a comparative study, this paper demonstrates steps that are needed for other interested groups to participate in ECN spray research. We expect that this collaborative effort will generate a high-quality dataset to be used for advanced computational model development at engine conditions.

INTRODUCTION

The Engine Combustion Network (ECN) is an experimental and modeling collaboration dedicated to the improvement of engine CFD modeling. The ECN contains an internet data archive library (http://www.ca.sandia.gov/ECN/) with well-documented diesel spray experiments at engine conditions. Quantitative comparisons of spray evaporation and mixing at high-temperature, high-pressure conditions are now possible, providing new opportunities for CFD model improvement at realistic engine conditions. The dataset also currently includes reacting and non-reacting data such as the liquid and vapor penetration versus time, liquid length, ignition delay and pressure-rise rate, lift-off length, quantitative soot volume fraction, and various high-speed movies of combustion. Several research groups have used the dataset for model validation (e.g. [1, 2, 3, 4, 5, 6, 7, 8]).

Until recently, the ECN data archive was derived from a single spray chamber facility at Sandia National Laboratories. However, many ECN users responded favorably to this initiative and are now working collaboratively to create future datasets of interest, utilizing multiple facilities throughout the

world. In particular, IFP is now an active participant and is working together with Sandia National Laboratories to structure and initiate the international collaboration. This collaboration has led to an ECN working group on spray combustion. The working group has identified a few experimental conditions that could become the focus of those who wish to voluntarily participate in the ECN. The experimental collaboration is made possible by the donation of "identical" injection systems by Robert Bosch, LLC. The ECN group has agreed to experiment at the same injector and ambient conditions, thereby leveraging the expertise of each participant, and enabling direct comparison between different facilities. Significant effort is being made to verify the boundary conditions at each facility, as well as to measure the rate of fuel delivery and internal movement of the injector. In the end, all participants will benefit by sharing information at the same operating conditions. This is the same vision guiding the Turbulent Non-premixed Flame (TNF) workshop [9], where years of quantitative experimental effort on a particular flame (e.g. "Flame D") have created a standard library for computational comparison. The ECN seeks to generate a similar database at engine conditions. We expect that the dataset developed will become a serious focal point for model validation and further advanced diagnostics.

Following the tradition of the TNF workshop, the ECN group has chosen to name the first target condition "Spray A" [10]. Specifications for the injector and ambient operating conditions for this condition are given in Table 1. Spray A is a low-temperature combustion condition relevant to engines that use moderate EGR and have minimal NOx emissions. The injector specifications pertain to modern advanced injection systems with high pressure capability. Bosch donated 10 different injectors for the initiative, including 5 single-hole injectors with an orifice on the axis of the nozzle, as well as 5 three-hole injectors with the same orifice size and an 145° included angle. Single, axial-hole injectors will be used for Spray A, while the multi-, side-hole injectors will be used at the same "Spray A" conditions, but with a "Spray B" designation. A comparison between single and multi-, side-hole injectors is therefore the objective of Spray A/Spray B experiments. Using the same injector body, the common rail and injector tube length are also specified to ensure consistent hydraulic effects on injection. A single-component fuel, n-dodecane, is chosen to enable a complete specification of the chemical and physical properties of the fuel. Detailed chemical kinetic mechanisms exist for n-dodecane [11, 12], allowing full treatment of the combustion chemistry. Although the boiling point temperatures of n-dodecane are lower than that of diesel fuel, n-dodecane has boiling point temperatures that are sufficiently high to emphasize spray mixing processes, n-dodecane is also compatible with production fuel pumping systems.

Spray data of the caliber needed for detailed model development and validation requires extensive characterization of all of the boundary conditions that will be used as model inputs. Two types of controlled spray chambers that are capable of operation at high-temperature, high-pressure conditions typical of engine combustion have been developed: (1) heated flow chambers and (2) constant-volume chambers that employ a preburn and cool down to the desired pressure and temperature. These facilities were recently reviewed by [13]. Although there are a growing number of these facilities throughout the world, uncertainties about their operation exist because of the uniqueness of each facility. To our knowledge, there has never been a direct comparison of spray combustion at two different facilities of this type.

The objective for this paper is to present concurrent measurements of Spray A boundary conditions and spray penetration and combustion data from combustion vessels at IFP and at Sandia National Laboratories. This work represents a collaborative effort to facilitate research at Spray A conditions, and other conditions that will be chosen as part of the ECN. ECN participants are expected to measure the boundary conditions (e.g., the parameters specified in Table 1) for the ambient and injector, and to state uncertainties associated with the boundary conditions and other data. However, some uncertainties are not recognized until there is repeat and duplicate experimentation. Our approach to better understand each facility, and to minimize uncertainties, is to directly compare results at these standardized experimental conditions. Once these boundary conditions are better understood, variation in parameters beyond those of Spray A can proceed with higher confidence. Accordingly, this paper demonstrates steps that are needed for other interested groups to participate in ECN spray research.

As opposed to a traditional paper, we have grouped the experimental setup and results together into individual sections that correspond to various phases of the research. These sections include (1) combustion vessel operation, (2) ambient gas characterization, (3) injector characterization, (4) spray liquid and vapor penetration, and (5) combustion characterization.

COMBUSTION VESSEL OPERATION

IFP and Sandia use a preburn-type combustion vessel to generate high-temperature, high-pressure gases. The ambient pressure, temperature and species at the time of injection are varied by igniting a premixed combustible-gas mixture that burns to completion. Following the spark-ignited, premixed combustion, the combustion products cool over a relatively long time due to heat transfer to the vessel walls and the vessel pressure slowly decreases. When the desired pressure and temperature is reached, the diesel fuel injector is triggered and fuel injection occurs. A detailed description of this type of facility is found in [10].

Table 1. Spray A Operating Conditions.

Ambient gas temperature	900 K
Ambient gas pressure[§]	near 6.0 MPa
Ambient gas density[§]	22.8 kg/m^3
Ambient gas oxygen (by volume)	15% O_2 (reacting); 0% O_2 (non-reacting)
Ambient gas velocity	Near-quiescent, less than 1 m/s
Common rail fuel injector	Bosch solenoid-activated, generation 2.2
Fuel injector nominal nozzle outlet diameter	0.090 mm
Nozzle K factor	$K = (d_{inlet} - d_{outlet})/10$ [use μm] = 1.5
Nozzle shaping	Hydro-eroded
Mini-sac volume	0.2 mm^3
Discharge coefficient	C_d = 0.86, using 10 MPa pressure drop and diesel fuel
Spray full included angle	0° (single axial hole)
Fuel injection pressure	150 MPa
Fuel	n-dodecane
Fuel temperature at nozzle	363 K (90°C)
Common rail volume/length	22 cm^3/ 28 cm (Use GM rail model 97303659)
Distance from injector inlet to common rail	24 cm
Fuel pressure measurement	7 cm from injector inlet / 24 cm from nozzle
Injection duration	1.5 ms
Injection mass	~3.5 mg
Approximate injector driver current	18 A for 0.45 ms ramp, 12 A for 0.345 ms hold

§This exact combination of ambient pressure and density corresponds to a particular set of gases for a 0%-O_2 condition with 89.71% N_2, 6.52% CO_2, and 3.77% H_2O by volume and a compressibility factor, Z = 1.01. When different gases are used, the pressure must vary to maintain the same density.

Photographs of each facility are given in Fig. 1. Each vessel has full optical access for line-of-sight or orthogonal diagnostics. The vessels are cube-shaped, measuring greater than 100 mm on each side, and allowing extensive visualization of the spray prior to wall impingement. Vessel dimensions and other characteristics are given in Table 2. The vessels are heated to mimic engine surface temperatures and to prevent condensation of combustion products onto windows. Multiple spark plugs are utilized to provide consistent ignition of fuel-lean mixtures. A mixing fan stirs the gases during intake filling and afterwards in order to prevent mixture and temperature non-uniformities. Corner ports of the vessel are used for the mixing fans, intake and exhaust valves, high-speed pressure transducers, or other instrumentation.

Since a prebum-method is used to generate high-temperature, high-pressure conditions, the composition of the initial fill reactants determines the combustion product mixture that exists at the time of injection. Product mixtures may be made inert (0% O_2), to simulate air (21% O_2), or to simulate air-EGR mixtures as is the case for Spray A (15% O_2). While only the target oxygen mole fraction is listed for the Spray A condition, the reactant mixture that is used will also affect the concentration of other combustion products, which in turn affects the molecular weight and other thermodynamic properties. IFP and Sandia traditionally use different reactant gases. The composition of the reactant and product mixtures that simulate Spray A conditions are given in Table 3 for 0% O_2 and 15% O_2 conditions. Product compositions are calculated based on the stoichiometry of the reactant mixture and the assumption of complete combustion. Other experimental conditions for the reactants and combustion products at the time of injection are also given in the table. These quantities will be explained and referred to throughout the paper.

The reactant mixtures differ between the two facilities in several ways. First, IFP used ethylene C_2H_4 as the hydrocarbon reactant as opposed to acetylene C_2H_2 at Sandia. In addition, IFP used a significantly higher percentage of hydrogen compared to Sandia. As a result, the molecular weight of the reactants and products is lower for IFP compared to Sandia, accompanied by a higher H_2O concentration and lower CO_2 concentration in the products. Because of the differing molecular weights (as much as 8%), the ambient gas pressure and density varies slightly between facilities, or between inert (0% O_2) and reacting (15% O_2) experiments. IFP chose to operate with an ambient gas

density 2% lower than Sandia in order to maintain ambient pressure near 6.0 MPa. Although operating with different ambient density, IFP and Sandia chose to keep the ambient gas density constant between inert and reacting experiments at their own facilities, thereby attempting to minimize differences in mixing and momentum exchange for the reacting and non-reacting experiments. Since other facilities plan to operate with pure nitrogen (inert) or nitrogen-diluted air (reacting), producing yet another ambient gas composition, we sought to understand how the different ambient gas composition might affect results in these preburn-type environments.

Sandia Combustion Vessel

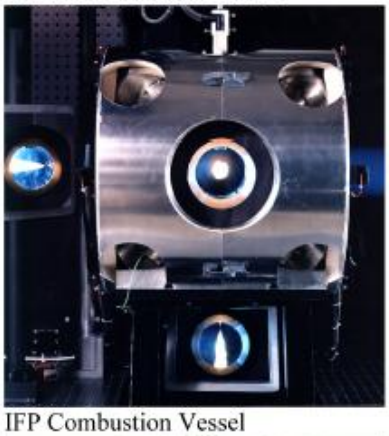

IFP Combustion Vessel

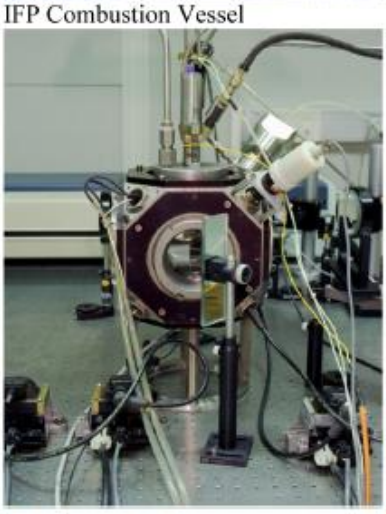

Figure 1. Constant-volume spray chambers at Sandia (top) and IFP (bottom).

Table 2. Combustion vessel characteristics for Spray A experiments.

	IFP	Sandia
width of cube	125 mm	108 mm
window aperture	80 mm	100 mm
chamber volume	1400 cm^3	1150 cm^3
injector mounting	center side window	center side window
injector tip protrusion from wall	3 mm	14.4 mm
injector serial #	210676	210677
mixing fan location	upper corner, near injector	upper corner, opposite injector
fan speed	3140 rpm	1000 rpm
# of spark plugs	4	2
spark plug position	lower corners	top window
body temperature	473 K	461K
combustible gas fill	sequential	premixed

Table 3. Reactant (at the time of spark) and product (at the time of injection) gas composition and properties.

	0% O_2 conditions		**15% O_2 conditions**	
	IFP	Sandia	IFP	Sandia
Reactant / Conditions at Spark				
%vol C_2H_4	0.780	-	0.816	-
%vol C_2H_2	-	3.20	-	3.06
%vol H_2	9.20	0.50	9.39	0.50
%vol N_2	83.00	88.05	68.36	73.82
%vol O_2	7.00	8.25	21.43	22.63
Mol. Weight MW	25.88	28.14	26.42	28.71
Compress. Fac. Z	1.00	1.010	1.00	1.009
Pressure [MPa]	3.42	3.30	3.35	3.23
Temperature [K]	453	445	453	445
Bulk density [kg/m^3]	23.50	24.79	23.5	24.85
$T_{ad,equil.}$ [K]	1762	2008	1772	1925
$P_{ad,equil.}$ [MPa]	12.44	13.97	12.45	13.78
Product / Conditions at Injection				
%vol O_2	0.00	0.00	15.00	15.00
%vol CO_2	1.68	6.52	1.71	6.20
%vol N_2	87.01	89.71	71.73	75.10
%vol H_2O	11.32	3.77	11.56	3.60
Mol. Weight MW	27.14	28.68	27.72	29.25
Compress. Fac. Z	1.010	1.016	1.010	1.015
Set pressure [MPa]	6.14	6.04	6.02	5.92
Act. pressure [MPa]	6.12	5.96	6.01	5.91
Set T_{bulk} [K]	853	826	853	826
Act. T_{core} [K]	897	873	900	888
Set ρ_{core} [kg/m^3]	22.06	22.80	22.06	22.8
Act. ρ_{core} [kg/m^3]	22.05	23.15	22.05	23.06

AMBIENT GAS CHARACTERIZATION

An accurate understanding of the ambient gas properties at the time of injection requires knowledge and control of the gas properties inducted into the chamber prior to spark-ignition, as well as during the premixed flame and combustion product cool down periods. The properties of these gases affect every aspect of spray combustion, including penetration, mixing, vaporization, ignition, and so

forth. In this section, we discuss measurement techniques and methods to produce consistent ambient gas distribution in the region of the vessel in front of the injector.

To provide an overview of the premixed burn and cool down processes, we performed high-speed imaging of the vessel gases during these time periods. Figure 2 shows schlieren and luminosity imaging for Spray A conditions in the vessel at Sandia. The optical setup is discussed in more detail below in Fig. 14. Briefly, the schlieren images were taken through the side of the vessel while, simultaneously, unfiltered luminosity was collected by a second high-speed camera from below. Schlieren imaging provides a measurement of density (or temperature) gradients, while luminosity imaging will show line-of-sight chemiluminescence or thermal emission. The images show premixed flames propagating from a pair of spark plugs at the top of the vessel. The injector tip is located in the cone-shaped feature at the left, and the mixing fan is at the top right in both the side and bottom views. The flames propagate down through the chamber, reaching the chamber walls and merging together as they move through the charge towards the bottom of the vessel. The flame nearest the mixing fan propagates more quickly. At 200 ms, the flame envelope is midway through the combustion chamber, and transparent zones are found on the top and the bottom of the schlieren images. The bottom transparent zone is fresh reactants that have yet to burn. The top zone (about −10 to −40 mm) contains combustion products that are no longer burning across the entire span of the chamber. Lacking strong gradients in temperature that are characteristic of a premixed flame (the flame has passed), the top zone also appears transparent, at least at first. With increasing time, however, schlieren disturbances appear at the top and move throughout the chamber. These schlieren effects are caused by heat transfer to the cooler vessel walls, which forms temperature gradients in boundary layers near the walls [25].

The schlieren images show complete combustion by approximately 400 ms after the time of spark, at which time the bright luminosity completely saturates the luminosity-imaging camera. As gases cool down after the premixed burn, luminosity from hot gases decreases but thermal radiation from hot metal surfaces is notable. The mixing fan glows red hot at the upper right, a bare-wire thermocouple radiates at the bottom right, and spark plug ground straps are visible near the middle. In the next sections, we discuss measurements of gas temperature and pressure corresponding to these image sequences.

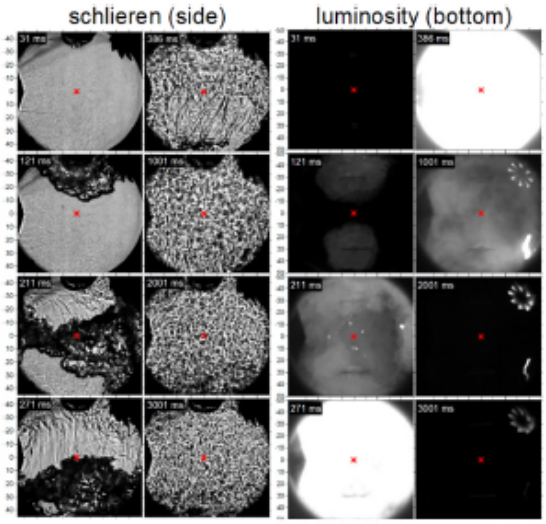

Figure 2. Schlieren (left) and luminosity (right) imaging of preburn and cool down for Spray A conditions. Flame begins at two spark plugs at the top. Injector is at left, distances are relative to injector in mm. Red x's are the position of a thermocouple measurement that will be discussed. Sandia vessel.

GAS TEMPERATURE

Gas temperature measurements were performed during the preburn and cool down to understand the temperature distribution of gases that will mix with the spray upon injection. Fine-wire thermocouples were used at both IFP and Sandia, consisting of two different setups as discussed below.

Platinum (type-R) thermocouple probe

A schematic of an adjustable probe with fine wire (50-µm diameter) platinum/platinum-rhodium (type-R) thermocouples is shown in Fig. 3. Five thermocouple probes are mounted on a rotational and traversable shaft, allowing for spatially-resolved temperature measurements within the volume in front of the injector. The dimensions of the thermocouple were chosen to minimize several sources of error, while also surviving repeated premixed burn and cool down periods in the combustion vessel. Small diameter wires are needed to minimize errors caused by thermal inertia, radiation, and conduction [15-16]. As is common for thin-wire thermocouples [17], the thermocouple is supported by larger wires of the same material, in this case 250-µm wires that extend approximately 10 mm from an insulated sheath. The thin-wire thermocouple is suspended between the two prongs, separated by approximately 8 mm.

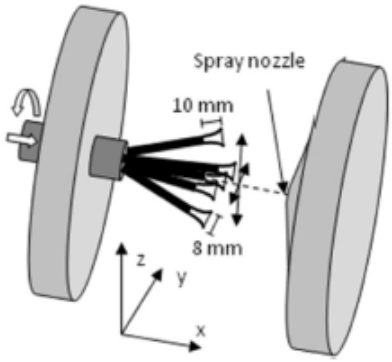

Figure 3. Schematic of adjustable probe with five fine-wire, type-R thermocouples.

Investigations (see e.g. [15, 16, 18]) show that the errors due to conduction heat exchange between wire and prongs can be neglected when the prong separation length, l, is,

$$l > 10 \cdot \sqrt{\alpha \tau} \tag{1}$$

In Eq. (1), a is the thermal diffusivity, and the time constant is

$$\tau = \frac{\rho_t c_t d_t}{4h} \quad , \tag{2}$$

using the thermocouple density ρ_t, specific heat c_t, diameter d_t, and the convective heat transfer coefficient h. Evaluation of these properties gives a value of 7 mm for right-hand-side term in Eq. (1), which is shorter than the prong separation distance. Therefore, conduction errors can be neglected for this thermocouple design.

Performing an energy balance at the location of the thermocouple junction it can be shown [15] that the actual temperature of the gas T_g is related to the junction temperature T_j in the following way:

$$T_g = T_j + \tau \frac{d}{dt} T_j + \frac{\varepsilon \sigma}{h} (T_j^4 - T_{sur}^4) \tag{3}$$

The second term is the convective heat transfer contribution and the third term is the radiation heat transfer contribution, including temperature-dependent emissivity ε. Note that the radiation correction will always be positive when the surroundings temperature T_{sur} (in this case, the vessel wall temperature) is lower than the junction temperature, as will be the case during the entire cool down period. Since the convective term strongly depends on the gradient of the junction temperature trace, the measured temperature is filtered to lower frequencies to avoid amplification of noise. The signals were low pass filtered to 100 Hz, which is more than 15 times greater than the −3 dB cutoff frequency of the thermocouple ($1/2\pi\tau \approx 7$ Hz) [15]. Smoothing prior to calculation of the derivative therefore has negligible effects on the frequency response of the system.

The R-type adjustable probe design was implemented in experiments at both Sandia and IFP. The experiments were successful at Sandia. However, IFP encountered difficulties that prevented use of the probe in their combustion vessel. During the filling of premixed combustible gases, IFP found that the mixture ignited when pure oxygen was being inducted into the chamber. The cause of the pre-ignition is almost certainly a catalytic response induced by the platinum thermocouple wires. In one event, uncontrolled ignition destroyed (melted) the thermocouple wires. We believe that the different outcomes at Sandia and IFP are related to the gas fill sequences at each institution. As shown in Table 2, IFP fills combustible gases sequentially into their chamber, which exposed high oxygen concentrations at elevated temperature and pressure to the platinum probe. However, Sandia fills its chamber with combustible gases that are already premixed. Although there is still potential for ignition, the diluted mixture of fuel and oxidizer was inducted without catalytic ignition. We recommend that caution be exercised when using catalytic thermocouple material for these types of heated, pre-burn combustion vessels.

Type-K thermocouple probe

As an alternative to the platinum thermocouple probe, IFP used a type-K thermocouple to measure gas temperatures. Unlike the type-R probe, the type-K probe consisted of only one thermocouple junction in a single location as shown in Fig. 4. The probe is a prototype designed by Thermo Est, which consists of progressively reduced diameter wire, terminating with a 25 µm diameter thermocouple to ensure fast response and minimum radiation and conduction error as discussed above.

Due to the limited temperature range of type-K thermocouples compared to the peak pre-combustion temperature, however, the thermocouples were operated at the limits of their design, causing failure and limiting the number of measurements carried out during the experimental campaign. Failed runs were removed from the dataset and the thermocouple probes were frequently replaced by new probes.

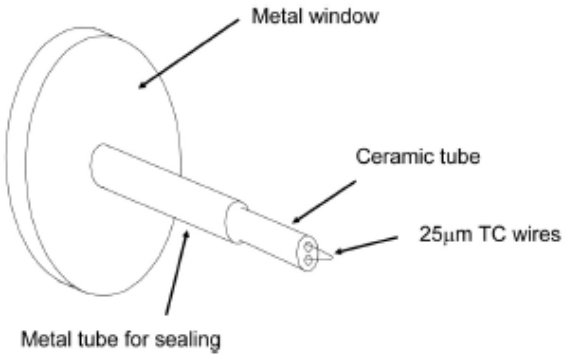

Figure 4. Schematic of thin-wire thermocouple. Type-K setup at IFP.

Gas temperature results

Figure 5 shows a sample measurement of gas temperature in the Sandia vessel from a single thermocouple 40 mm in front of the injector for 0%-O_2 conditions.

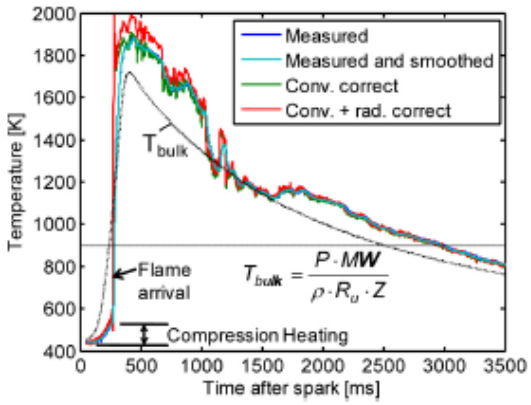

Figure 5. Measured gas temperature during the premixed burn and cool-down period. Sandia vessel. Type-R TC position is 40 mm directly in front of injector (x =40 mm, y = 0 mm, z = 0 mm). 0% O_2 combustion products and 24.8 kg/m^3 bulk density.

For reference, this position is also indicated by a red marker in the images shown in Fig. 2. The measured temperature is corrected for radiation and heat transfer transients after low-pass filtering as described above.

The bulk temperature (T_{bulk}) is also shown, as determined from the real-gas equation of state using the measured pressure and initial mass-averaged bulk density as indicated in the figure. Since the total mass within the chamber is constant, the bulk density is constant for an experiment and T_{bulk} depends only on the measured pressure. For calibration purposes, T_{bulk} can be related to the actual temperature of the gases that will mix with the spray, which is called the core gas temperature (T_{core}).

The gas temperature measurements show an initial rise caused by compression heating of unburned mixtures ahead of the flame. The flame arrives at the thermocouple at approximately 250 ms, whereupon there is a rapid increase in temperature. The corrected temperature appears to track the transient of the flame, rising quickly as would be expected for a premixed flame front. The temperature continues to rise due to compression heating as the vessel pressure (or bulk temperature) increases, reaching a peak temperature slightly lower than the adiabatic, constant-volume temperature given for 0%-O_2 conditions in Table 3. After the time of peak pressure, the gases slowly cool by heat transfer with the surrounding walls. The images in Fig. 2 exhibit evidence of this heat transfer as the schlieren disturbances grow along the windows and exposed surfaces (like the fan blades) begin to glow. Significant fluctuations in gas temperatures occur for temperatures higher than approximately 1200 K and time less than 1 s, with dips that even approach the bulk temperature. These early fluctuations are repeatable, and location-specific, indicating that they are most likely caused by large-scale movement of the product gases. The large-scale convection does tend to settle with increasing time. Note, for example, the overall similarity in the schlieren images at 2 s and 3 s with a darker zone near the bottom of the vessel, compared to that at 1 s. The gas temperature eventually cools to the Spray A temperature (900 K) at approximately 3 s. During most of the cool down, the measured temperature in the core zone right in front of the injector is higher than the bulk temperature because cooler, higher density gases exist in boundary layers and in the bottom of the vessel. Temperature gradients in these locations appear in the schlieren visualization.

Heat transfer corrections for convective response and radiation are shown to be significant during the early, high-temperature period of the cool down. However, the corrections are small, producing only a 2 K mean decrease, when the temperature decreases to 900 K. This is partly because of offsetting corrections during the cool down. Addressing the time period when gas temperatures are near 900 K, the convective heat transfer corrections lower the temperature by 5 K, but radiation corrections raise the temperature by 3 K. The heat transfer corrections do show more fluctuation in temperature, as would be expected because the corrections attempt to account for the thermal inertia of the thermocouple. An accurate measurement of the fluctuation in temperature, as well as the mean value, will be important as one tries to describe the initial boundary conditions as completely as possible. The average often different cool-down events is shown in Fig. 6. In this case, we

show measurements taken at both IFP and Sandia at the same position, 40 mm in front of the injector. IFP's measurements were made using the type-K setup, while the Sandia measurements were from the type-R probe, as above. IFP's data are also corrected for heat transfer as discussed above, but similar to the Sandia data, the correction is minimal. The bulk temperature history for each facility is also shown for comparison with the measured temperatures.

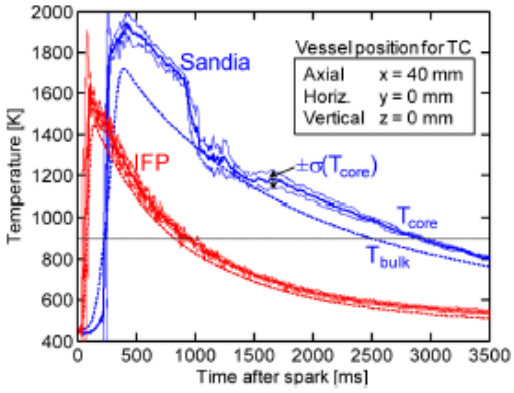

Figure 6. Average core gas temperature 40 mm directly in front of injector (x =40 mm, y = 0 mm, z = 0 mm) for IFP and Sandia vessels. 0% O_2 combustion products and 25 kg/m³ bulk density.

An obvious difference between IFP and Sandia is the faster premixed flame and cool down at IFP. This difference is related to the operation of the mixing fan. The fan speed is higher at IFP (see table 2), causing higher velocities and a higher rate of heat transfer. Increasing or decreasing the fan speed at either facility permits adjustment of the cool down rate to be faster or slower than either curve given in Fig. 6. In this case Sandia purposefully slowed the fan speed in order to make the environment more suitable for schlieren visualization of the vaporizing spray, as will be shown.

Another difference between IFP and Sandia data is the lower peak temperature measured at IFP. A lower peak temperature is actually expected, based on the initial reactants used at IFP. Table 3 shows that the adiabatic temperature at these conditions is only 1762 K at IFP, compared to 2008 K at Sandia. A faster rate of heat transfer during the premixed combustion event at IFP is also a likely contributing factor.

Gas temperature measurements at both institutions show higher core gas temperatures compared to the bulk temperature. However, the ratio of T_{core}/T_{bulk} is higher at Sandia, approaching ratios of 1.08 at the Spray A temperature. Our experience shows that this finding is once again related to the slower gas velocities, which leaves large zones of cool fluid at the bottom of the vessel. Increasing the fan speed tends to lower T_{core}/T_{bulk}. For example, an 8000 rpm fan speed produces T_{core}/T_{bulk} values of only 1.03 in the Sandia vessel [10].

The particular relationship between T_{core}/T_{bulk} is not important, as long as the temperature distribution is consistent from run to run. To indicate the variance in temperature, we show thin dotted lines at ± one standard deviation during the cool down period surrounding the mean. The variance in temperature tends to decrease during the cool down, and at the target temperature of 900 K, is ±10 K for the IFP measurements and ±10 K for the Sandia measurements at the target time of injection. Considering the resolution of the experiment, and the need to make corrections for heat transfer, these variances are similar to the expected uncertainty in gas temperature. Analysis of the temperature histograms shows that the temperature fluctuations are normally distributed, implying that 70% of the temperature fluctuations fall within these limits. The variance statistics do not improve when collapsing the data to T_{core}/T_{bulk} which one might suppose would account for different cool down timings because of variation in wall temperature, for example. Since the experimental method requires heat transfer to cool combustion product gases, temperature fluctuations are natural and expected. The local temperature fluctuations are one likely explanation for any variation in system performance from injection to injection.

Spatial variation in temperature was addressed by movement of the thermocouple probe to different positions within the chamber at Sandia. Figure 7 shows the average gas temperature at various positions in this "core" region of the vessel, relative to predictions based on a single relationship between T_{core} and T_{bulk} (i.e., using only the measured pressure to predict T_{core}). Along the axis of the spray, the gas temperature is uniform within 1%, except for a measurement point in the boundary layer only 1 mm in front of the injector tip. This spatial variation in mean temperature is similar to the instantaneous fluctuation shown above. Temperature is also uniform along the same horizontal plane (z = 0, y = ±15 mm) outside of the spray. The most significant variation is in the vertical direction (z = ±15 mm, y = 0) where the temperature varies by ± 4% for a vertical change of ± 15 mm. This vertical stratification is obviously caused by buoyancy effects. Despite the vertical variations in temperature, systematic combustion asymmetries in the vertical direction (i.e., ignition site, or liftoff length) have not been found, as will be shown later.

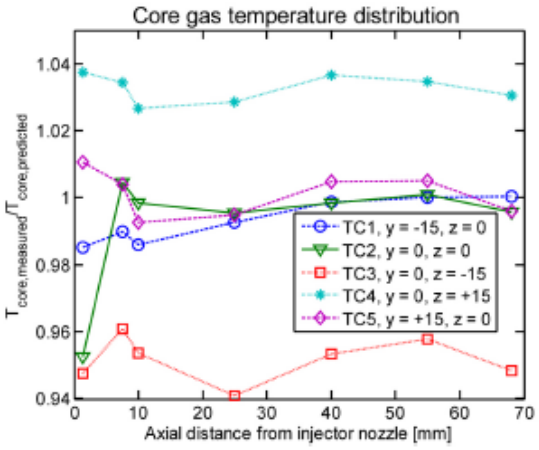

Figure 7. Average gas temperature in the "core" region of the Sandia combustion vessel at Spray A conditions, 0% O_2.

Overall, the results show that a fairly uniform core temperature can be produced for gases that will mix with the spray upon injection. Furthermore, measured T_{core} values are higher than T_{bulk} but it is possible to relate the two in a manner that will accurately predict T_{core} for a given facility. The significant difference between measured T_{core} and T_{bulk} is a point that is often overlooked in engine or combustion vessel experiments. Direct measurement of gas temperature provides a relationship between the core and bulk temperatures so that the core temperature surrounding the fuel spray can be predicted from the pressure measured during subsequent experiments.

GAS PRESSURE

Gas pressure is measured by standard piezoelectric transducers located in the corners of the vessel. The transducers are water cooled (IFP) or shielded with a perforated ceramic sleeve (Sandia) to prevent thermal drift after the premixed flame reaches the transducer [14]. The transducers have been calibrated against NIST-traceable sources at the operating temperature of the vessel, and have an accuracy of ±1%.

COMBUSTION PRODUCT GAS COMPOSITION

The ambient gases listed in Table 3 are assumed to consist of only complete-combustion products. Of course, this assumption will not be entirely true. As is well-known in spark-ignition combustion, unburned reactants can persist in crevice regions along the walls or sealing rings where reaction is quenched by the cool surfaces. Lack of complete combustion is one explanation for non-attainment of the constant-volume adiabatic temperature or pressure during the premixed burn, along with heat transfer to the vessel walls during combustion as explained above. Measurement of unburned hydrocarbons in the vessel exhaust at Sandia confirms that trace hydrocarbons exist, however no other species were directly measured at this time and we are not yet prepared to give an experimental report of the combustion product composition.

Modeling studies have been performed, however, to assess the likelihood of the persistence of minor species in addition to the major species listed in Table 3. The modeling studies show that the minor species mole fraction decreases during the cool down [10]. For temperatures near that of the Spray A conditions, the minor species are predicted to be less than 0.02% of all combustion products-indicating that the product compositions given in Table 3 for major species are likely close approximations for boundary conditions at the time of diesel injection. Further study using fast sampling valves is planned to assess the formation of minor species during the premixed burn, and its potential affect on the subsequent diesel combustion.

GAS VELOCITY

Velocities induced by the mixing fan are small in comparison to that of the spray, producing a near-quiescent environment for mixing with the spray. Spray velocities are expected to exceed 600 m/s at the nozzle exit, while velocities measured in the ambient are required to be less than 1 m/s for Spray A conditions. Prior to injection, the ambient gas velocity depends upon the fan speed and shape, as well as convective activity induced by the premixed burn. For the Sandia vessel at the conditions listed in Table 2, particle tracking velocimetry shows random velocities less than 0.1 m/s exist within the chamber. However, detailed velocity and turbulence measurements have not yet been performed. The mean velocities are used for the prediction of convective heat transfer coefficients that are needed to perform heat transfer corrections to the measured thermocouple data.

PIV measurements performed within the IFP vessel show mean velocities on the order of 2 m/s, corresponding to the higher fan speed used in this study. However, as has been mentioned, the fan speed can be adjusted to reduce the velocity and rate of cool down within the chamber, allowing attainment of the Spray A ambient velocity for future research. In fact, the mixing fan was shut off completely to make accurate measurements of the ambient velocities surrounding the spray in a recent study [20]. As has already been mentioned, the higher velocities cause a faster rate of cool down at IFP compared to Sandia. The effect of the ambient gas velocity on the spray, and other diagnostics, will be discussed.

INJECTOR CHARACTERIZATION

A detailed understanding of the injector operation is needed in order to provide sufficient boundary conditions for spray modeling. Future measurement plans include metrology of the internal shape of the nozzle, as well as the movement of the needle. In this section, we show measurements of the rate of injection and methods for control of the fuel temperature according to the Spray A specification.

For the experiments at IFP and Sandia shown in this paper, two different injectors were used because the experimental campaigns occurred at the same time. For future reference, the injector serial numbers are listed in Table 2. Since different injectors were in use, the results address questions about repeatability from injector to injector. There may be an opportunity to repeat the experiments after switching injectors, thereby addressing variability caused by the injector, versus that of the facility.

To promote repeatability at different facilities, the Spray A condition specifies the common rail, and rail-to-injector tube length (see Table 1). Figure 8 shows a labeled photograph of the rail and injector setup at IFP. A tube length from the rail to injector of 24 cm provides some flexibility for adoption to a particular experimental setup, while also being representative of the length used in engines. A larger rail volume is utilized to minimize pressure drop in the fuel supply during injection. The particular rail outlet is intended to isolate fuel pressure fluctuations from the fuel pump as much as possible.

As high-speed measurement of fuel pressure can add much information about the hydraulics within the fuel system, and their impact on rate of injection, the location of this fuel pressure measurement is also specified for Spray A. The photograph shows a flush-mounted pressure transducer 7 cm from the injector inlet. This position is approximately 26 cm along a hydraulic path away from the injector nozzle sac volume.

PRESSURE AND RATE OF INJECTION

Figure 9 shows the mass flow rate of injection for the injector used at Sandia (mass flow rate was not measured at IFP), along with fuel pressure and injector driver current at both Sandia and IFP. The mass flow rate is calculated by measurement of the spray momentum using a force sensor, combined with separate cumulative mass measurement [21]. The rate of injection exhibits a fairly top-hat shape and the total mass injected quantity is 3.5 mg.

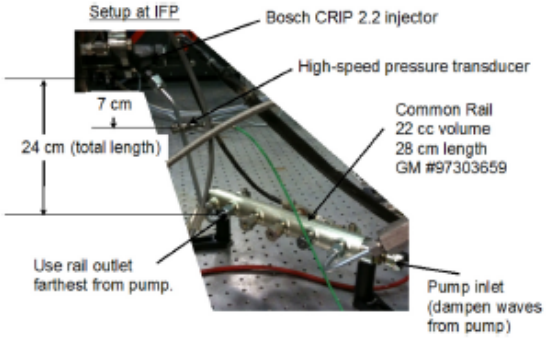

Figure 8. Photograph of common rail, tube leading to injector, and pressure transducer mounting at IFP.

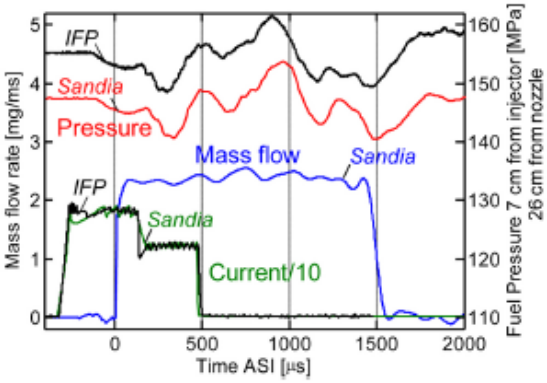

Figure 9. Spray A mass flow rate of injection and comparison of measured fuel pressure and injector driver current at IFP and Sandia.

The measured hydraulic fluctuations in fuel pressure are shown to be similar at each institution, even when using different injectors. In addition, the pressure transducer used at Sandia is not flush-mounted like the one shown in Fig. 8 for IFP. The transducer at Sandia is mounted on the side after a T-fitting. The fluctuations in fuel pressure appear to coincide with measured fluctuations in the rate of injection, with a phase shift consistent for the fuel speed of sound (approximately 1600 m/s) and the length between the nozzle and the pressure measurement location. Despite some differences in the absolute fuel pressure (caused by limitations with the fuel pressure control systems), the similarity in measured fuel pressure fluctuations means that subtle changes in fueling rate during the course of injection will likely be represented at each institution. The injector driver current is also reasonably similar, even though different custom drivers are used at each institution.

INJECTOR TIP TEMPERATURE

The Spray A operating condition designates the fuel temperature to be 90°C. As we will discuss in this section, quantifying and controlling this fuel temperature is not trivial due to the temperature transients that occur as a part of the operation of these facilities. In addition, as discussed in the previous section, these temperature transients occur differently at each facility. As we will show, differences in the fuel temperature at the time of injection can influence the spray penetration and vaporization characteristics and thus need to be carefully controlled at the specified Spray A condition. The Spray A specification requires that the sac volume upstream of the orifice should be 90°C, as shown in Fig. 10. Specifying the fuel temperature upstream of the orifice where velocities are low is more straightforward compared to designating the fuel properties inside the orifice. Steep gradients in pressure and velocity, which cause thermodynamic state changes [22], as well as the potential for energy transfer and friction heating by the surrounding walls make it preferable to specify the fuel temperature upstream of the orifice. Determining the actual injected fuel temperature at the orifice exit is a difficult task that would require specific developments that are well beyond the objectives of the present work.

Figure 10 shows that the fuel is in close contact with the needle and injector tip surfaces, so a reasonable approach is to control the entire injector nozzle temperature. However, achieving this temperature control is not straightforward for several reasons. First, the chamber walls of facilities at IFP and Sandia are pre-heated to nearly 200°C, as given in Table 2. A method for isolation and cool down of the injector is therefore required to avoid excess heating of the injector and fuel. Second, premixed combustion within the vessel creates elevated gas temperatures that may heat up the tip of the injector during cool down. We therefore have a need to understand the degree of tip heat up, and to minimize this temperature rise.

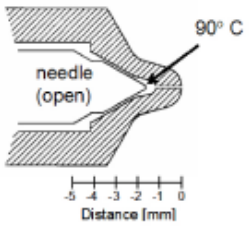

Figure 10. Schematic of Spray A axial-hole injector nozzle in the fully open-needle position. Fuel temperature is specified upstream of the orifice, where fluid is expected to be near stagnant.

Sandia and IFP both use a liquid flow to cool down the injector. The control systems are shown in Figs. 11-12. Sandia uses a water cooling jacket, insulated by teflon from the heated metal housing, with a mounting piece at the center of the cooling jacket that can be adapted to hold different injectors. In the IFP system, cooling water flows inside the injector mounting piece close to the injector nozzle. In both facilities a ceramic insulator is used to cover the injector's tip to prevent over heating by the hot combustion product gases during cool down. The schematics are shown with measured temperatures in various positions during steady-state conditions, prior to pressurization or premixed combustion.

One approach for fuel temperature control is to simply adjust the cooling (or heating) rate to achieve a nozzle temperature of 90°C, assuming that the fuel temperature in the sac volume during injection will be close. This assumption might not be completely true, and in addition, it is possible that the fuel temperature is not uniform throughout injection. Fuel temperature in the sac volume may be different than that upstream in the injector body. Possible deviations from the assumption will be taken into account when analyzing results in the next sections.

In order to measure the nozzle temperature, three methods were considered and tested:

- Holding a thermocouple probe in close contact with the surface of the nozzle tip.
- Measuring the temperature in the sac of a dummy injector with a thermocouple. It consisted of a nozzle for which the needle was removed and replaced by a thermocouple.
- Laser-induced phosphor thermometry (LIP) on the surface of the nozzle tip during actual premixed burn and cool down events.

The first method is the simplest but it has two important limitations. The first is that it cannot be carried out during a pre-combustion event and therefore it can only give access to the nozzle tip temperature during steady-state conditions (no pre-combustion). A nozzle tip temperature increase is expected during premixed combustion and cool down, which may cause the temperature at injection timing to differ significantly from that at steady state. The second limitation is that the surrounding gases can heat the thermocouple probe and cause conduction errors at the thermocouple, particularly since it is difficult to ensure perfect contact between the probe and the nozzle tip surface.

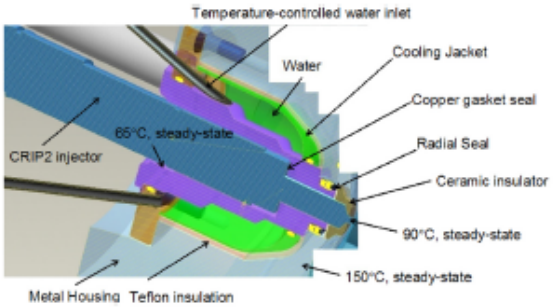

Figure 11. Schematic of injector temperature control system at Sandia, along with measured temperatures prior to the premixed burn.

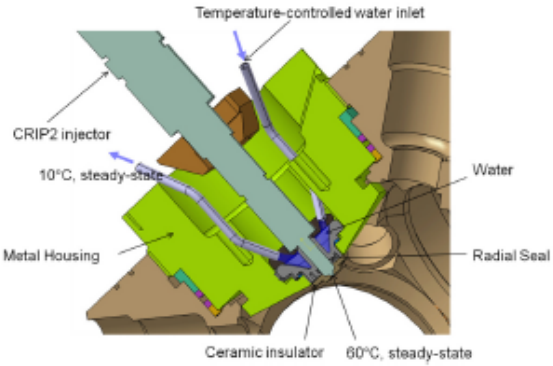

Figure 12. Schematic of injector temperature control system at IFP, along with measured temperatures prior to the premixed burn.

Because the installation of a thermocouple in the injector may interfere with needle operation, the temperature inside the sac requires the installation of a dummy injector in the mounting. It also suffers from the limitation that measurements cannot be carried out during the premixed combustion event unless a specific system is built to ensure high pressure sealing; which was not the case in the present work. However, the internal temperature of the nozzle is less ambiguous than the first method since surrounding gas temperature effects are removed. This method also cannot provide dynamic temperature measurements during injection since no fuel flows within the injector.

The third method requires application of a specific optical technique. LIP is a non-intrusive method capable of measuring surface temperatures with a high time resolution [23]. A thin phosphor layer is deposited on the surface of the nozzle tip. This layer is then excited by a UV laser beam and the resulting phosphorescence is recorded by a photomultiplier. The signal is analyzed to obtain the phosphorescence decay time which is related to the phosphor temperature, hence the surface temperature, providing that the phosphor layer is thin. The difficulty of this technique lies in the calibration and in the data processing. The advantage is that it is a non-intrusive technique giving access to the nozzle tip surface temperature during the cool down.

The first two methods were employed at Sandia and IFP to determine the steady-state temperatures given on the schematics in Figs. 11 and 12. As IFP has developed an expertise in the application of LIP [24], nozzle tip surface temperature measurements by LIP were carried out at IFP to access the time evolution of the nozzle tip temperature during the cool down, and also to determine the effect of the ceramic insulator. The 514-nm band of La_2SO_2:Eu phosphorescence, excited at 266 nm, was used to measure surface temperatures in the range of 40 to 110°C. During setup, it was shown that the internal sac temperature of the dummy injector and the nozzle tip surface temperature by LIP gave similar results. Having performed this calibration check, LIP was then attempted during the premixed burn and cool down.

Measurements of the nozzle tip surface temperature during the premixed burn and cool down are shown in Fig. 13, both with and without the ceramic insulator. The measurements correspond to a circular area of approximately 1 mm in diameter right at the nozzle tip. For these measurements, the steady state nozzle tip temperature prior to the premixed combustion event was regulated at 60°C (using the thermocouple measurement in the dummy injector). The LIP measurements confirm that before premixed combustion (before 0s) the nozzle tip temperature is about 60°C. During combustion (between 0 and 0.5 s) no temperature measurements are available because combustion luminosity interferes with the phosphorescence collection by the photomultiplier. After premixed combustion (after 0.5 ms) the LIP measurements show that the nozzle tip temperature rises to about 100°C without a ceramic insulator. With the ceramic insulator covering the tip, the nozzle tip surface temperature increases to only about 80-90°C, showing that the ceramic insulator is effective in limiting the heating by the hot gases during cool down. These results also show that in order to obtain a nozzle tip surface temperature of about 90°C in the IFP vessel at injection timing (about 1 s after premixed combustion ignition-see Fig. 6), it is necessary to regulate the temperature to approximately 60°C in the steady state. This setting was therefore used for all the experiments carried out in the IFP facility presented in this paper

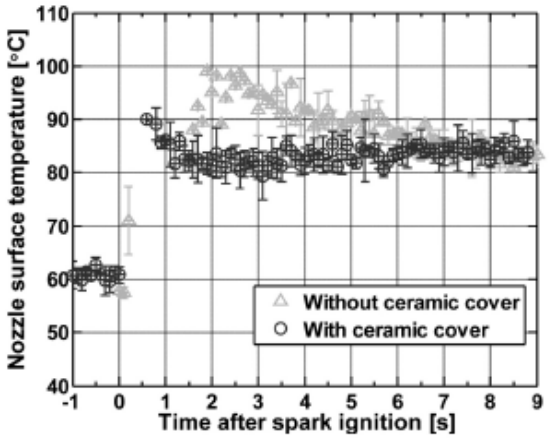

Figure 13. Nozzle tip surface temperature measurements by laser-induced phosphorescence. IFP.

Referring again to Fig. 10, we note that these LIP temperature measurements correspond to the outer surface of the nozzle. The internal temperatures are not known, but we can expect them to be in between the nozzle surface temperature and the steady-state temperature inside the nozzle. Fuel that is initially upstream of the needle will most likely be cooler, towards the steady-state temperature, but it will be heated as it flows towards hotter surfaces at the nozzle tip.

In the absence of nozzle tip surface temperature measurements at the timing of injection in the Sandia facility, and considering that internal nozzle temperature will be cooler than the surface temperature, the nozzle temperature was set to a steady-state operation of 90°C at Sandia. The nozzle temperature increase during premixed combustion in the Sandia facility is not known. It may be of the same order as that at the IFP facility, reasoning that similar cooling is necessary to reach the target temperature at the time of injection. However, recall that the cool down is much longer (Fig. 6) at Sandia, which allows more time for heat transfer. Regardless, the nozzle tip at Sandia is surely higher than 90°C at the start of injection because of heat transfer. This fact, combined with the higher steady-state setting (90°C compared to 60°C) means that the fuel temperature was higher at Sandia compared to IFP. The difference in nozzle tip temperature at injection timing between the two facilities will be taken into account when analyzing results in the next sections.

SPRAY LIQUID AND VAPOR PENETRATION

Care taken in the establishment of injector and ambient boundary conditions is necessary before one can expect similarity in the vaporization and mixing processes of the spray. In this section, we present liquid-phase and vapor-phase visualization of the penetrating spray. It is well known that both the liquid penetration and vapor penetration rate [27] depend strongly upon ambient gas temperature and density, as well as injection pressure, orifice diameter, and so forth. The maximum liquid penetration length during the steady-state also depends upon ambient gas temperature and density [21].

EXPERIMENTAL SETUP

Mie-scatter and schlieren imaging were performed using high-speed imaging systems to track both the liquid and vapor phases of the spray. These are convenient diagnostics for assessing the similarity in spray mixing, and are recommended for Spray A experiments prior to the implementation of more complicated diagnostics. Setups at IFP and Sandia are briefly described below.

Mie-scatter and schlieren setup- Sandia

Scattered light from fuel-spray liquid droplets was imaged using a high-speed CMOS camera and a continuous-wave laser. As shown in Fig. 14, a schlieren system was operated simultaneously using a second high-speed CMOS camera, similar to the setup reported in [25]. The time-resolved pair of schlieren and Mie-scatter images identifies the instantaneous position of both the vapor and liquid phases of the fuel spray, respectively.

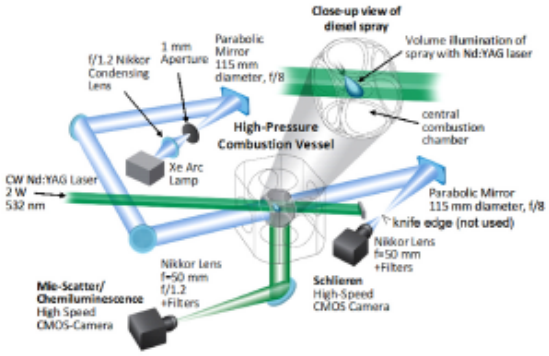

Figure 14. High-speed imaging setup used at Sandia (not to scale).

The continuous-wave laser source was formed into a volume to illuminate the liquid-phase region of the spray. A volume-illumination method, rather than a laser sheet, was utilized to ensure that all droplets spreading from the nozzle were illuminated to identify the maximum axial and radial distances of any liquid-phase fuel. The input beam was directed at a slight angle to avoid interference with the schlieren setup.

A high-speed CMOS camera, fitted with a 532-nm bandpass filter (10-nm FWHM) and a 50-mm focal length f/1.2 lens, was used to image Mie-scattered light at a near-right angle to the laser source. The camera was operated at reduced resolution (48 × 256 pixels) to allow fast framing periods (11.25 µs) and short exposure times (7.75 µs) in a setup intended to capture dynamics of very fast fuel sprays. The lens was set to the maximum aperture (f/1.2) to intentionally saturate the camera in the dense region of the spray while leaving sufficient dynamic range to identify regions of the spray where liquid completely evaporates.

Schlieren imaging was performed simultaneously using a second lighting and imaging arrangement. Light from a mercury-xenon arc lamp was collimated to pass through the combustion vessel. The collimated beam was then re-focused before entering a high-speed CMOS camera equipped with a lens and a 532-nm 0°-incidence laser mirror, which acted to block Mie-scattered light from spray droplets. The camera was operated at a resolution of 128 × 256 pixels, allowing for framing periods of 21.25 µs with an exposure duration of 2 µs.

Previous studies in the Sandia facility utilized several different schlieren stops at the collection focal point shown in Fig. 14, including a knife edge, aperture (bright-field), cutoff disk (dark-field), or no stop [25]. The sensitivity of the system to refractive index gradients can be adjusted by the use of different cutoffs [26]. However, for the setup of Fig. 14 there is adequate sensitivity at Spray-A ambient densities with no stop at the focal point. For example, the images of the premixed flame and cool down shown in Fig. 2 have no stop, other than the lens aperture, but yet the density gradients are clearly shown. In addition, this setup produced superior performance when post-processing the images to detect the vapor boundary [25]. We will show results of this post-processing below.

Mie-scatter and schlieren setup- IFP

Similar to the Sandia setup, a high-speed CMOS camera was used to image scattered light from fuel-spray liquid droplets or, in separate experiments, to image the spray vapor boundary by a schlieren method. The setup is shown in Fig. 15.

A Xenon arc lamp was used to illuminate the liquid-phase region of the spray, with the light directed head-on to the penetrating spray. The high-speed CMOS camera, unfiltered and fitted with a 105-mm focal length lens at f/2.8, was used to image Mie-scattered light at a near-right angle to the laser source. The camera was operated at higher resolution (400 × 640 pixels), but with slower framing period (50 µs) and exposure time (18 µs) than the Sandia setup.

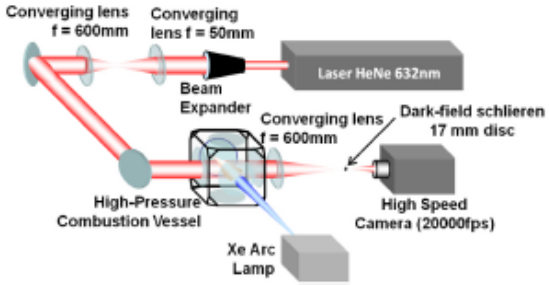

Figure 15. High-speed imaging setup used at IFP.

Schlieren imaging was performed using a HeNe laser light source as shown in Fig. 15. The laser beam was expanded and collimated with lenses, passed through the chamber, and then re-focused with a collection lens. As the schlieren sensitivity depends upon the distance from the spray to the collimating lens and camera [26], IFP found the best performance using a dark-field setup with a 17 mm disc placed at the focal point of the schlieren setup. A lens with a 105-mm focal length was fitted on the CMOS camera. For reacting experiments (15% O_2) a 633-nm bandpass filter, 2-nm FWHM centered at the laser wavelength, was installed to reject combustion luminosity. The camera was operated at the same resolution and speed as the Mie-scatter setup, except that the exposure duration was 5.6 µs.

LIQUID AND VAPOR PENETRATION RESULTS

Liquid penetration

We first compare the liquid spray penetration at each facility. Mie-scatter image sequences from single injection events at IFP and Sandia are shown at similar times after the start of injection (ASI) in Fig. 16. After the initial penetration period, the maximum liquid penetration stabilizes at approximately 11 mm. Analysis of the ensemble-average liquid penetration during this quasi-steady period from multiple injections shows a mean liquid length of 10.6 mm at Sandia, and 10.9 mm at IFP (reference Fig. 21, shown later), when processing the images using 3% of the maximum signal upstream in the spray as was used by Siebers [21]. These differences are within the experimental uncertainty of each facility, given 95% confidence intervals for the repeatability in liquid length from injection to injection. The sprays therefore appear to have similar vaporization distances at each facility, once reaching the steady state.

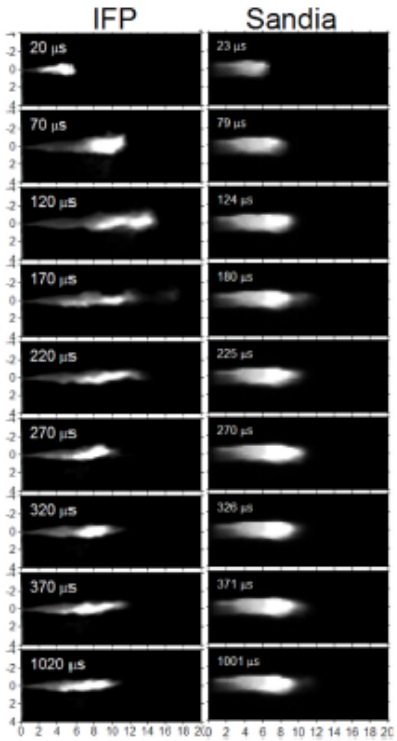

Figure 16. Mie-scatter imaging sequence at IFP and Sandia, each for a single injection. Spray A conditions, 0% O_2.

However, differences in the spray appearance are definitely manifest. Some of these differences are likely related to the optical setup. Recall that the light source is opposite the direction of the spray at IFP (head-on), whereas the spray is side-illuminated at Sandia. Head-on illumination should mark the longest liquid penetration zone, but it may not illuminate the near-nozzle region as well because of light attenuation at the head of the spray. Also, the IFP imaging setup has higher resolution and larger depth of focus, which makes the spray appear more in focus. This comes at the expense of a slower rate of image acquisition (approximately 5 times slower) compared to Sandia. Finally, the illumination intensity may not be the same in the two setups.

Despite some differences in spray appearance caused by the optical setup, the maximum distance of the liquid penetration is clearly not the same during the initial transient development of the spray, an effect that is over and above the effects of optical setup (or other experimental uncertainties). The IFP spray shows liquid penetration downstream to about 14-16 mm during a period between 120-220 µs ASI, before relaxing to the quasi-steady value near 11 mm. In contrast, the Sandia spray does not substantially penetrate past the quasi-steady liquid length at 11 mm during startup of injection. The cause of this difference during the transient is not known, but there are several considerations.

As discussed previously, the fuel was controlled to a higher temperature at Sandia compared to IFP. Liquid penetration would be expected to be lower when the fuel temperature is higher. Temperature not only changes the sensible energy of the fuel, but it also affects density and viscosity as shown in Fig. 17. To demonstrate the cumulative effect of fuel temperature, in Fig. 18 we show predictions of maximum liquid penetration length based on the mixing-limited vaporization model of Siebers [21]. Predictions are shown for the Spray A experimental conditions while varying fuel temperature. We also demonstrate the effect of ambient temperature by showing a second curve at a lower ambient temperature of 875 K. The figure shows that liquid penetration is expected to decrease by approximately 1 mm for a 30°C increase in fuel temperature, a temperature difference that is of the order expected between setups at IFP and Sandia.

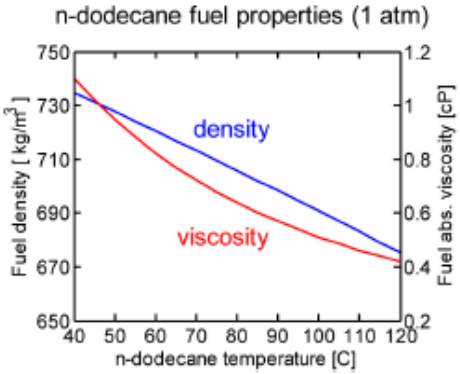

Figure 17. Fuel temperature effect on density and absolute viscosity for n-dodecane (atmospheric pressure).

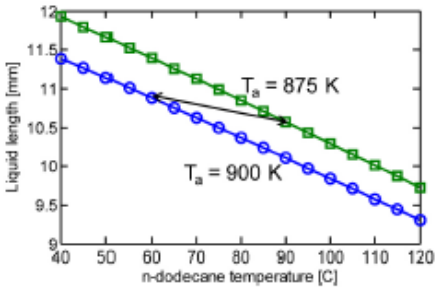

Figure 18. Predicted liquid length from Siebers' model [21] as a function of fuel temperature. Spray A conditions, including one curve at 875 K ambient temperature.

Figure 18 also shows that a reduction in ambient temperature increases liquid length, as expected. As shown, the quasi-steady liquid length may not change if there are offsetting effects of increased fuel temperature and decreased ambient temperature. This may be one explanation why the liquid lengths match closely between IFP and Sandia, even though the fuel temperature was different. Table 3 shows that the Sandia experiments (0% O_2) fell below the target Spray A ambient temperature by 25°C. Reasons for this deviation include an oversight in control to match the set pressure at the time of injection, as well as a later, more detailed evaluation of the measured ambient temperature to draw a relationship between T_{core} and T_{bulk} that was discussed above. Although there are natural fluctuations in temperature that are of the same order as 25°C, which may cause variation from injection to injection, an average temperature decrease will, of course, increase the average liquid length. Figure 18 shows that 25°C ambient temperature decrease, combined with a fuel temperature increase of 30°C produces predicted liquid lengths that are of the right order as of the experimental quasi-steady liquid lengths for which the model is based. For example, we show a connecting arrow for the 30°C fuel temperature difference measured in the steady-state at each facility. The experimental values for liquid length at IFP and Sandia are in good agreement at these two endpoints. However, the experimental differences in transient penetration at the start of injection between IFP and Sandia are larger than the several mm shift predicted by either fuel or ambient temperature changes depicted in Fig. 18. Therefore, we believe that other considerations are needed to explain differences during the startup period.

There is a possibility that the transients in liquid penetration are simply caused by different injector and injector driver configurations. Figure 9 showed that the measure injector ramp current is initially slightly higher for IFP compared to Sandia. Different injector temperatures may also affect the start-of-injection transient. Perhaps the IFP injector opens more quickly, causing a slug of fuel to accelerate and penetrate for a moment past the quasi-steady liquid length. Another possibility is that the sac volume of the Sandia injector becomes increasingly emptied of liquid fuel when the injector is heated. Hot combustion product gas will flow into the sac volume during the premixed burn in the combustion vessel (or during compression in an engine). The heated gas, as well as depressurization towards the time of injection, can vaporize and push liquid out of the sac volume prior to the time of injection. Consequently, a fuel/gas mixture (rather than pure fuel) may be present within the sac volume at the time of injection, producing shorter liquid spray penetration during the start-of-injection transient. Evaporation of fuel in the injector sac is expected to happen to a certain degree in both Sandia and IFP injectors, but it should occur to a greater degree for the Sandia injector since the steady-state temperature is 30 K higher. Another possibility is that there is a significantly colder pocket of ambient gas very near the injector for IFP, which is rapidly entrained and replaced by hotter ambient gas as the spray penetrates. This hypothesis is supported by the fact that the IFP injector protrudes less from the wall compared to the Sandia injector (Table 2). The above ideas are clearly speculative but they may form the basis for further investigation that can explain the differences in spray penetration between the two injection systems. For example, further gas temperature measurements at IFP can prove or disprove the theory about a cold pocket of ambient gas. Purposeful variation of injector temperature is another idea for testing these theories.

Considering these unknowns, one way to address the initial state (i.e. temperature) of the injector tip is to study the liquid penetration during time, for example, using long injection durations where the injected fuel temperature is expected to cool the injector tip and more closely approximate the steady-state temperature. Figure 19 compares the maximum liquid penetration for a Spray A injection duration (1500 µs), and a very long injection duration with the same ambient conditions. Performed at Sandia, the liquid lengths are processed the same way using a 3% threshold. Measured liquid lengths are shown on a tight y-axis scale to demonstrate the effect. The figure shows that liquid length increases by approximately 0.5 mm before stabilizing at approximately 2000 µs ASI. Using the predicted liquid lengths given in Fig. 18, we observe that a change in liquid length of 0.5 mm corresponds to a fuel temperature change of approximately 20°C. Interestingly, this is approximately the same temperature increase measured by LIP for the nozzle tip surface temperature during the premixed burn and cool down (Fig. 13).

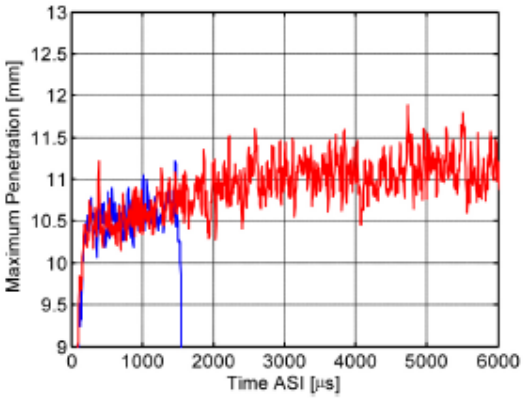

Figure 19. Maximum liquid penetration versus time ASI. Single injections at the Sandia facility.

As the Spray A injection concludes at 1500 μs ASI, prior to the liquid stabilization point at 2000 μs ASI, the implication is that Spray A is not completely steady, even though the injection duration is long by engine standards. As background information about what may cause the spray to become steady, we note that the fuel volume injected (5 mm^3, 3.5 mg mass) corresponds to about 25 times the injector sac volume. Sufficient mass and volume moving through the internal passages of the injector is apparently needed to stabilize the injector and fuel temperature.

Vapor penetration

A sequence of schlieren images from single injection events at Sandia and IFP are shown in Fig. 20. The schlieren images are shown with computer-processed boundaries in green. The boundary is determined by analysis of the difference between successive images, which are shown at the bottom of the figure (raw schlieren at top). This method for image processing and display removes schlieren effects that exist in the ambient gases in order to more easily visualize the actual jet structure [25]. For example, if schlieren effects from the ambient were non-existent, the dark-field schlieren images of IFP would be completely dark in the background and the vaporizing spray would generate light regions that may be convenient for image processing. However, the schlieren disturbances in the ambient make this impossible, generating the requirement to use an alternative image processing method. In addition to the schlieren boundary, blue lines are also overlaid on the Sandia images to indicate the border of simultaneously acquired Mie-scatter (liquid) [25].

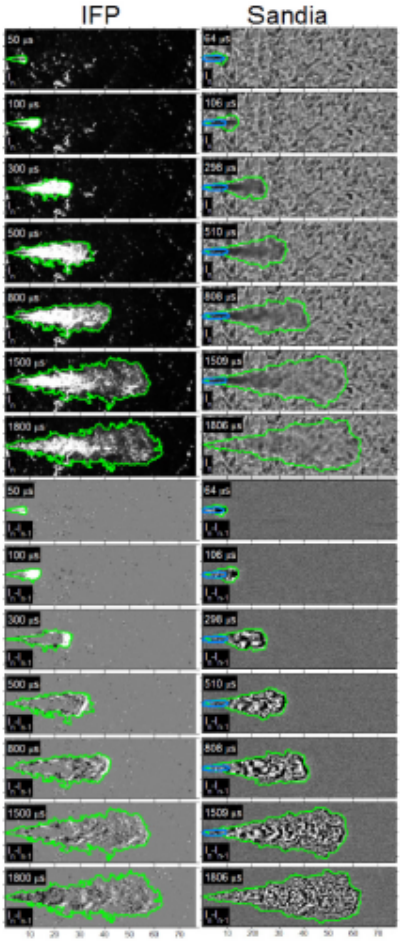

Figure 20. Schlieren imaging with the computed vapor boundary shown in green. Spray A conditions with 0% O_2 (non-reacting). Image pairs are shown without (top, I_n) and with (bottom, I_n-I_{n-1}) background correction. Sandia images also show the simultaneous liquid border in blue.

The schlieren images show reasonable similarity for vapor penetration and dispersion for sprays at IFP and Sandia at similar times ASI. Some image processing issues for detection of the true edge of the jet persist, but detection of the penetrating head is less ambiguous. To more directly compare the penetration, we have processed the spray border at the jet head in the same manner as Naber and Siebers [27], which uses a 50% probability criterion for penetration within the inner half-angle of the spray. The ensemble-average penetration from a set of ten different injections is shown in Fig. 21. We include penetration of the liquid phase, as well as reacting vapor penetration (15% O_2).

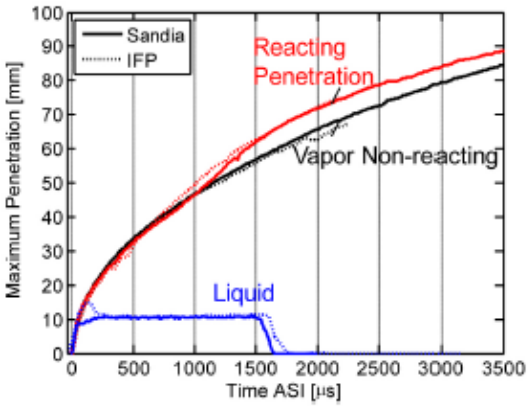

Figure 21. Comparison of liquid, vapor, and reacting flame penetration at IFP and Sandia. Liquid length threshold is 3% of maximum. Vapor penetration was determined as in Naber and Siebers, 1996.

Considering the complexities of the experiment, the good agreement between the liquid, vapor, and reacting flame penetration at each facility is quite remarkable. Both facilities show that reacting penetration exceeds the non-reacting penetration, and there is similar liquid penetration during the steady period of injection. Differences between facilities fall within a 95% confidence interval for repeatability in the average vapor penetration at each facility (error bands are provided with the data on the ECN website). The remaining differences, in fact, may be caused by artifacts from image processing rather than any real, measureable difference. Dominant structures from background schlieren effects are difficult to completely remove and the image processing routines are still being improved.

Concerning the liquid penetration, the IFP data shows the overshoot in liquid penetration during the start of injection that was discussed above (Fig. 16). Importantly, however, the initial rate of liquid (or vapor) penetration is not higher at IFP compared to Sandia. This is supporting evidence that the initial rate of injection, or the spray spreading angle, is not substantially different between the facilities, despite the fact that different injectors are in use, as well as the fuel temperature differences discussed above.

The liquid penetration curves do show that the injection duration appears slightly longer at IFP. The Sandia liquid length begins to recede towards the injector [28] at approximately 1500 μs, compared to approximately 1600 μs for IFP. This difference is not surprising, given that different injectors were in use and only the *electronic* injection duration was prescribed. For future research, the actual injection duration can be controlled easily by trimming the injector driver hold current duration.

The liquid- and vapor-phase visualization shown above is intended to be a first step towards the characterization of the spray mixing and vaporization. We recommend that other groups participating in Spray A research start with Mie-scatter and schlieren visualization to characterize the global behavior of the fuel spray. For future research, more quantitative diagnostics, such as droplet sizing or mixture fraction measurement, can be added to the dataset to attain a more complete understanding of the spray mixing processes.

COMBUSTION CHARACTERIZATION

Matching performance of the combustion characteristics of a spray at two different facilities is expected to require increasing levels of control of the boundary conditions. Ignition and combustion depend upon vaporization and mixing steps discussed in the previous sections, of course. However, ignition has an even higher sensitivity to temperature (exponential) [30] than does liquid-phase penetration [21], for example. Combustion experiments are therefore expected to provide increased scrutiny about the similarity in operation between different facilities.

EXPERIMENTAL

The high-speed CMOS cameras shown in Figs. 14-15 were operated filtered or unfiltered to detect chemiluminescence and soot luminosity for reacting, 15%-O_2 experiments. In some cases, laser sources were also utilized as described above so that Mie-scatter and flame luminosity were simultaneously collected, or so that schlieren images could be acquired under reacting conditions. Together, these diagnostics allow determination of the timing and position of cool-flame first-stage ignition, second-stage, high-temperature ignition, transient flame lift-off length, and soot formation [25].

In addition to high-speed imaging, IFP used an intensified camera fitted with a UV lens and 310-nm centered bandpass filter to detect OH chemiluminescence. Images were time-averaged over the steady period of combustion, similar to Siebers [29], to attain the quasi-steady lift-off length.

Also, the measured pressure within the chamber was analyzed to determine ignition timing and the overall heat release from diesel combustion. For this analysis, the pressure decay during the cool down was removed (subtracted) to yield the pressure rise caused only by diesel combustion [10]. The data are normalized by the adiabatic pressure rise expected for complete combustion of the fuel energy injected into a particular chamber. In this manner, we compare the combustion efficiency of the spray in each facility.

RESULTS

Ignition

Figure 22 (top) shows direct imaging of combustion luminosity relative to the start of injection by high-speed luminosity. The IFP images were obtained unfiltered, while the Sandia set had a 600 nm short-pass filter installed. By continuing to use the 532-nm and arc lamp illumination shown in Fig. 14, the Sandia setup allowed visualization of ignition location, as well as the Mie-scatter and schlieren regions similar to the non-reacting (0%-O_2) conditions already shown above. Schlieren images were obtained simultaneously, and are shown at the bottom right of Fig. 22 in their raw, unprocessed form.

The ignition delay to high temperature combustion is marked by the first combustion luminosity, which appears at 400 µs ASI at IFP, and at 450 µs ASI at Sandia. The ignition delays are therefore similar, but slightly less at IFP compared to Sandia. Later analysis will show that this first luminosity is high-temperature chemiluminescence, rather than cool flame chemiluminescence or soot luminosity. The location of ignition is approximately 15-25 mm from the injector at each institution. Note that the ignition location is downstream of the region of liquid penetration. It is therefore not surprising that the measured liquid lengths in this reacting environment are essentially the same as the non-reacting conditions shown above (i.e. 11 mm), because heat release does not directly affect the liquid vaporization region.

To aid in visualization, we have marked the border of the high-temperature chemiluminescence in blue and overlaid it on the simultaneously-acquired schlieren images for the Sandia dataset. The threshold for this border is 0.1% of full scale. Overlaid on the schlieren images, we observe that the onset of chemiluminescence corresponds to a change in refractive index gradient in the schlieren images and a radial expansion as would be expected by high-temperature heat release. The effects of heat release on the schlieren effect are best visualized by comparison to the non-reacting images, which are given at lower left. These results show that the timing and location of high-temperature combustion is consistent by either direct chemiluminescence imaging or schlieren imaging. Similar results were shown in [25].

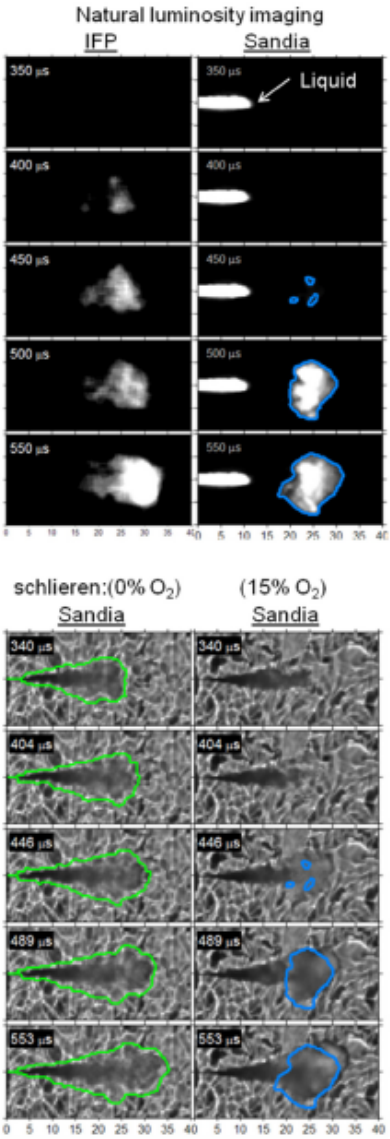

Figure 22. Upper: Natural luminosity high-speed imaging for detection of ignition delay (left, IFP; right, Sandia). Lower: Schlieren images taken simultaneously with Sandia luminosity (right), luminosity border overlaid in blue; and non-reacting (0% O_2) schlieren with vapor border overlaid in green (left).

The schlieren visualization also provides an opportunity to assess the ignition stages leading up to high-temperature combustion. As discussed in Ref [25], the schlieren images tend to show a "disappearance" of the vaporized fuel jet during the first cool-flame stages of combustion. The "disappearance" of the jet is believed to be caused by fuel breakdown and mild heat release that makes the refractive index of the cool-flame region match that of the ambient gases, hence becoming less sensitive to schlieren effects. Such effects are noticeable in Fig. 22, particularly comparing the reacting and non-reacting schlieren. For example, the darker portion of the schlieren effect does not extend as far away from the injector in the reacting jet at 404 μs compared to 340 μs, despite the increased time ASI that should cause the jet to penetrate more, not less, and the obvious increased penetration for the non-reacting spray. Comparing to the non-reacting spray, the cool flame looks as if it has "eroded" the head and sides of the spray. Then at the time of high-temperature ignition (446 μs), the head of the jet suddenly reappears as low-density zones make the schlieren effect reappear. Meanwhile, the chemiluminescence from the cool flame is not bright enough for detection by the non-intensified, high-speed cameras. For example, there is no measureable chemiluminescence at 400 μs. Only after the temperature of the igniting zone increases, as confirmed by the sensitivity of schlieren to temperature, is the chemiluminescence bright enough for detection. For these reasons, we know that the first appearance of signal on the high-speed cameras is caused by high-temperature chemiluminescence.

Image processing to define the border of the spray can be used as an indication of the onset of the cool flame. Figure 23 shows the maximum penetration of the reacting spray near the time of high-temperature ignition for an ensemble-average often injections at Sandia. The reacting penetration has been calculated with high-sensitivity for jet edge detection to measure the true jet penetration, or with lower sensitivity to indicate the cool flame timing. The non-reacting vapor penetration is also shown as a reference. The non-reacting spray uses the same low-sensitivity parameters used to indicate the cool flame. Therefore, the cool-flame penetration curve is not an image processing artifact, but rather, is definitively the result of heat release. When processed with the appropriate sensitivity, the figure shows that the reacting spray appears to stall at 250 μs, eroding the head of the jet to a minimum by 300 μs before returning to the same curve at 450 μs, the time of ignition. Therefore, the time period between 250 - 450 μs ASI is one of apparent cool flame activity.

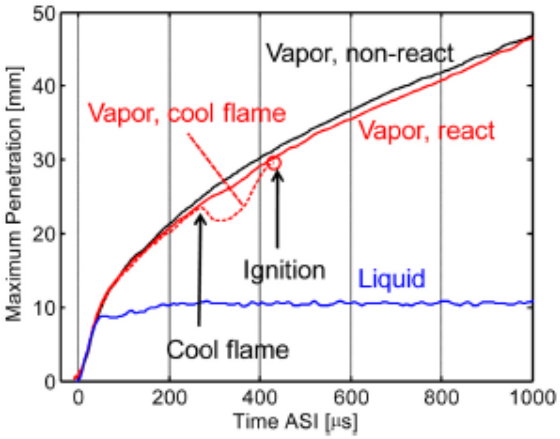

Figure 23. Processed ensemble-average spray penetration from schlieren imaging at Sandia. Image processing with high or low sensitivity allows detection of a cool flame region that appears to stall the penetration. Non-reacting vapor and liquid penetration is shown for reference.

The cool flame and high-temperature heat release also appears to modify the rate of penetration of the spray, as the reacting penetration is less than the non-reacting penetration. The lower rate of penetration is statistically significant when considering the repeatability of the penetration from injection to injection. (Accompanying penetration uncertainty is available on the ECN website.) The slower penetration is short-lived, however. Figure 20 shows that the reacting spray penetration catches, and exceeds, the non-reacting spray penetration at approximately 1000 μs ASI. A faster rate of penetration for a reacting jet can be explained by such things as thermal expansion dilation caused by heat release [25,29], but it is less clear why there are differences shortly after cool flame and high temperature ignition. Reasons for these transient heat release effects on penetration (and mixing) will be explored as part of future Spray A research.

Lift-off length

Following ignition delay, the reacting zone stabilizes into a quasi-steady lifted flame [29]. To image the lift-off stabilization period, and perform a measurement of the steady lift-off length, Sandia utilized several different low-pass filters to block bright soot luminosity downstream. As explained above, IFP performed OH chemiluminescence imaging. Figure 24 shows high-speed imaging using a 450-nm short-pass filter at Sandia. The IFP result, which is a time-average of OH chemiluminescence from 1100-1800 μs ASI, is also shown at the bottom right. The minimum distance of the reaction zone relative to the injector was calculated as in Ref [29].

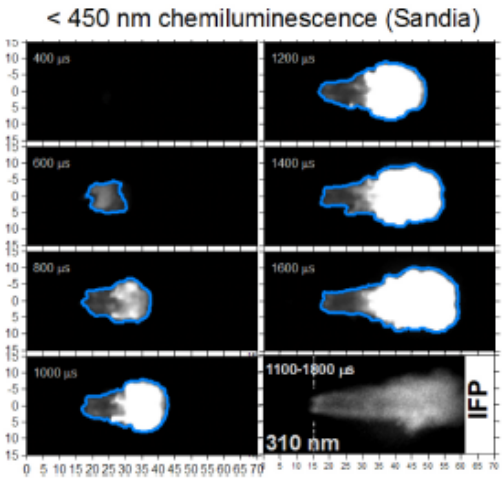

Figure 24. Measured chemiluminescence at Sandia and IFP (lower right) during injection. Sandia: 450-nm short-pass filter, 197 µs exposure duration. IFP: 310-nm filter, 1100-1800 µs gate open period.

Figure 24 shows that chemiluminescence begins downstream of the injector, rises sharply, then levels off at a higher value. The threshold for the lift-off length is defined as 50% of this leveling-off value. This threshold border is depicted in blue lines on the high-speed sequence of Fig. 24. Note that bright soot luminosity causes another substantial increase in luminosity farther downstream, but this zone can still be distinguished from the upstream chemiluminescence zone when filtering to shorter wavelengths. This is particularly true when using 310-nm collection, because of the weaker soot emission at shorter wavelengths [29].

The images show that the flame stabilizes between 15-20 mm shortly after autoignition, and the lift-off length remains in this position during the rest of injection. The tendency for flame lift-off to stabilize at the upstream region of autoignition has been demonstrated for many different operating conditions [30, 31, 32]. The Spray A results are therefore consistent with these previous observations. An ensemble-average of lift-off length versus time ASI is given in Fig. 25. The figure shows results at Sandia using several different short-pass filters, as well as the average lift-off length measured at IFP for multiple injections using imaging at 310 nm. The stabilization of lift-off length shortly after autoignition is apparent, regardless of the collected wavelength. Lift-off for the Spray A injection duration of 1500 µs is also compared to that of a longer injection duration. These results show that lift-off during the Spray A injection (i.e. prior to 1500 µs) is essentially the same as that if injection were to continue, showing that the lift-off length is quasi-steady. However, after the end of injection, reaction tends to propagate back towards the injector, momentarily, at approximately 300 µs. Afterwards, the reaction zone drifts downstream towards more fuel-rich mixtures, as expected based on the fuel-air mixing dynamics after the end of injection [34].

The average lift-off length during the 1100-1800 µs ASI period is shown to be very close, as measured by either IFP or Sandia. Once again, we consider this a significant accomplishment considering the complexities of the experiments. The average lift-off length is 1.4 mm less at IFP compared to Sandia. A shorter lift-off length is consistent with the shorter measured ignition delay at IFP (Fig. 22), as studies show that sprays with shorter ignition delay tend to have a shorter lift-off length [30,32]. In addition, ignition delay and lift-off length are known to be highly sensitive to ambient temperature [29,30], which implies that there is a temperature difference between the two facilities. Based on measured lift-off length and ignition delay trends for a fuel with a cetane number of 80 (similar to n-dodecane that has a cetane number of 87) [10], we expect that a temperature difference as small as 20 K could explain the differences between the two facilities. Table 3 shows that the actual core temperature at Sandia was already 12 K lower than the target 900 K temperature, which is consistent with the measured trend. The indication that temperature is slightly cooler at Sandia compared to IFP is also consistent with observations of the non-reacting spray penetration (e.g. Fig. 17). As has already been mentioned, continued interrogation of the temperature distribution, particularly closer to the injector at IFP, will be explored in the future.

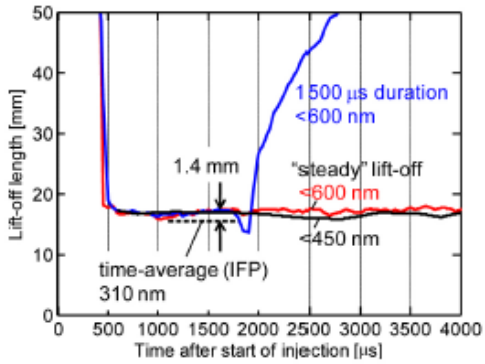

Figure 25. Ensemble-average lift-off length versus time after the start of injection.

Soot luminosity

As mentioned above in conjunction with Fig. 24, soot forms after high-temperature ignition. The soot formation is not immediate after ignition, however. Figures 22 and 24 show that high-temperature chemiluminescence is active by 450 µs,

but increased soot luminosity that actually saturates the camera does not begin until approximately 800-1000 μs ASI. Resetting the camera exposure duration to be short (1 μs), we can prevent camera saturation and study the evolution of the soot luminosity. Figure 26 shows an image time sequence taken at IFP using these camera settings.

With reduced camera sensitivity, the chemiluminescence is no longer visible at 600 μs ASI even though this is well after ignition. Natural soot luminosity appears by 700 μs and continues to grow in size and intensity. Peak soot luminosity occurs at 1200-1600 μs. The region of soot luminosity moves downstream and shrinks as soot oxidation dominates after the end of injection. Similar soot formation processes and timings are suggested by noting the saturation regions of the images taken at Sandia in Fig. 24. However, further comparison is needed because of the image saturation.

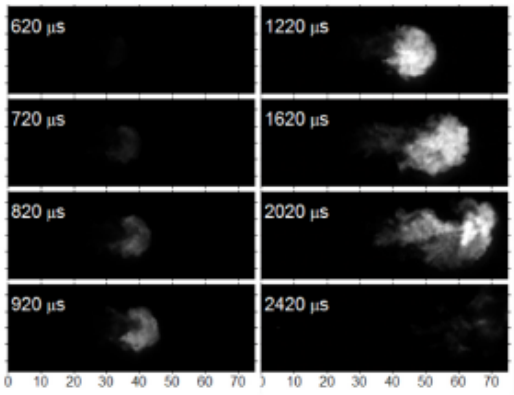

Figure 26. Natural soot luminosity time sequence taken at IFP.

Our method for comparison is to integrate the total luminosity in the images, and normalize the result by the maximum intensity during injection. Figure 27 is an ensemble-average of the total soot luminosity at IFP and Sandia. For the Sandia data, two different datasets are shown. The first has higher sensitivity to detect ignition and chemiluminescence, but the detector saturates during the intense soot formation. The other has lower sensitivity and does not saturate during soot formation, but it has less ability to detect chemiluminescence. By joining the two datasets, the dynamic range of the measurement is increased. Figure 27 shows that luminosity increases after the time of ignition (400-500 μs), which results above have shown is initially caused by an increased area and intensity of chemiluminescence. But as soot forms, the luminosity intensity increases by orders of magnitude. The soot luminosity rise does occur earlier at IFP compared to Sandia. In addition, the timing of peak soot luminosity, and the decrease in luminosity because of soot oxidation, occur earlier at IFP compared to Sandia.

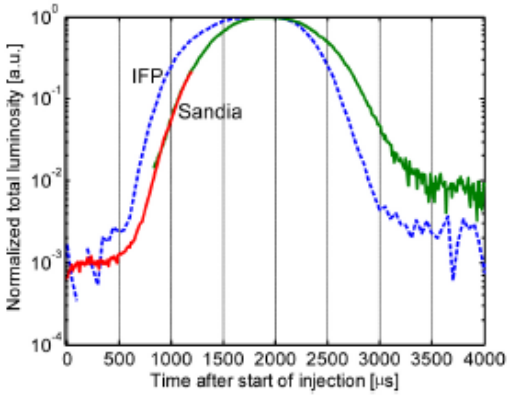

Figure 27. Normalized total luminosity for Spray A conditions at IFP and Sandia.

An earlier timing of soot formation is consistent with measurements of an earlier ignition delay and shorter liftoff length, perhaps caused by a slight temperature difference between the two facilities as noted above. Soot formation is also strongly temperature dependent, even when mixing delay times are the same [35]. Therefore, the soot luminosity results are in agreement with expectations based on earlier measurements. We are less certain about the causes for the apparently faster soot oxidation at IFP compared to Sandia. Higher ambient gas velocities at IFP could explain the faster oxidation after the end of injection, particularly when the soot cloud is quite stagnant after the end of injection, and therefore more sensitive to subtle movement of the ambient. However, we also need to consider that regions of downstream soot luminosity may be blocked by a smaller window aperture at IFP (see Table 2), thereby causing an earlier decrease in soot luminosity.

Pressure rise

Figure 28 shows the ensemble average of pressure rise at both IFP and Sandia. As explained above, the pressure decay during the cool down was subtracted to yield the pressure rise caused only by spray combustion. The data are then normalized by the adiabatic pressure rise expected at each facility, which accounts for different chamber volumes, bulk density, and ambient gas properties, and the energy content of the injected fuel. The raw pressure data is quite noisy, owing to the large chamber volume and mass. Low-pass filtering was performed to smooth the data shown in the figure, but some noise remains.

The pressure traces at both facilities show a rapid increase at approximately 0.5 ms ASI, which corresponds to the ignition

delay timing visualized by high-temperature chemiluminescence. The pressure rise continues to increase, reaching a 50% burn point near the end of injection at 1.5 ms ASI, and end of combustion (maximum pressure rise) at approximately 3.0 ms ASI. The pressure analysis shows that a significant portion of combustion actually occurs after the end of injection, despite the fairly long injection duration.

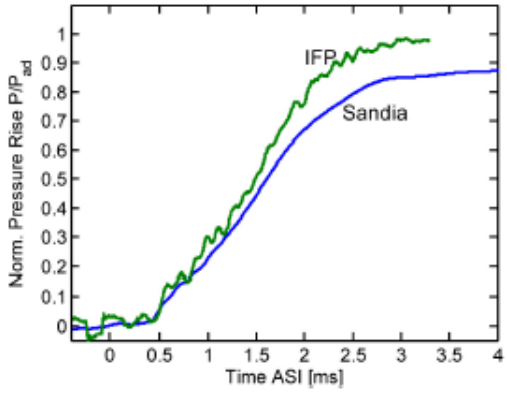

Figure 28. Normalized total pressure rise for Spray A conditions at IFP and Sandia.

Analysis of the maximum pressure rise shows that the heat-release efficiency is high at each facility, near 90% or higher of the adiabatic limit. We expect that the pressure rise should fall lower than the adiabatic limit, even if the combustion efficiency (conversion of fuel to complete-combustion products) is perfect, because the spray combustion has several sources of heat transfer. For example, the luminosity shown in Fig. 27 will transfer energy away from the flame and act as a heat loss term by radiation. In addition, the high-velocity spray induces a higher rate of convective heat transfer once the spray interacts with combustion vessel walls. Both of these effects will lower the energy transfer to the ambient gases, and reduce the pressure rise to be lower than the adiabatic limit.

Based on the close similarity of the combustion process, we expect that the combustion efficiency should be similar in each facility. Therefore, differences in the final pressure rise are most likely due to systematic effects of heat transfer or other uncertainties associated with each facility. For example, crevice volumes near window sealing surfaces create uncertainties about the total chamber volume, as well as the initial bulk density. In addition, the bulk density is calculated assuming a uniform gas temperature at the start of premixed combustion. Temperature non-uniformities of the premixed reactant mixture create additional uncertainties about the initial bulk density. Also, effects of heat transfer to the injector tip create uncertainties about the actual mass of injection. Calibrations for injected mass (3.5 mg, Table 1) were performed at steady-state injector temperatures. However, a heated fuel tip will lower fuel density and injected mass, which might partially explain the lower pressure rise at Sandia compared to IFP.

SUMMARY/RECOMMENDATIONS

The Engine Combustion Network has established a standardized set of test conditions (Spray A) for future experimental research as a pathway for CFD model improvement and validation. Initial results obtained at two different facilities, IFP and Sandia National Laboratories, show reasonable similarity despite the challenges of providing matched boundary conditions at these unique facilities. These encouraging findings suggest that parallel research, and leveraging experimental work at different facilities, can accelerate the development of a high-quality dataset and improved understanding of spray combustion. To facilitate this dataset development and exchange, we will make the data from this paper available on the ECN website, together with the total uncertainty and experimental variance for each measured quantity.

The investigation addressed control of vessel and fuel injector boundary conditions, as well as the first detailed measurements of Spray A mixing and combustion. Significant findings from the study include:

- Direct measurement of gas temperature in the region in front of the injected spray can be performed using fine-wire thermocouples, with accompanying corrections for thermal radiation and convective heat transfer. The average temperature distribution of a "core" region of gases in front of the injector is spatially uniform within 10 K at the Sandia facility, but the instantaneous variance in temperature is ±10K (± one standard deviation). The core temperature is higher than the bulk temperature derived from the measured pressure.

- By specifying the same common rail, and rail-to-injector tube length, the measured hydraulic fluctuations in fuel pressure are similar at each institution, even when using different injectors. The fluctuations in fuel pressure coincide with measured fluctuations in the rate of injection.

- Although the injector tip can be controlled to a steady-state temperature of 90°C, the premixed burn and cool down heat up the injector tip above this Spray A-specified temperature. Laser-induced phosphorescence measurements show that the nozzle surface temperature increases by 20-30°C during the cool down at IFP, which may necessitate control to a lower steady-state temperature in order to achieve a 90°C fuel temperature, at the time of injection

- Quasi-steady liquid lengths for Spray A measure approximately 11 mm at either Sandia or IFP. The agreement in liquid length is most likely aided by a combination of lower ambient temperature and higher fuel temperature, or

vice versa, at each facility. Sandia operated with a higher fuel temperature, but also had a lower ambient gas temperature. These variables can offset to produce the same liquid length.

• Despite the agreement in quasi-steady liquid length, the IFP spray shows liquid penetration during injector startup that is approximately 5 mm longer than the quasi-steady liquid length. The Sandia spray does not show this effect. Reasons for this difference are currently unknown, but will be explored by further fuel and ambient temperature characterization.

• The vapor penetration of both non-reacting and reacting sprays at IFP and Sandia shows agreement that is within experimental uncertainty. This is a significant finding, considering the complexities of the experiment, and the fact that two different injectors were in use. The reacting penetration is affected by heat release, at first slowing compared to the non-reacting spray, but then eventually overtaking and exceeding the non-reacting spray.

• Ignition delay and quasi-steady lift-off length are shorter at IFP compared to Sandia. Differences are slight, however, only 50 μs and 1.4 mm, respectively. A shorter ignition delay and shorter lift-off length are consistent with ambient gas temperatures that are higher at IFP compared to Sandia. We estimate that a temperature difference of only 20 K could explain the differences. Higher ambient temperature can also explain the faster soot formation at IFP compared to Sandia.

The comparative study between different facilities has offered new information about uncertainties associated with the boundary conditions for Spray A operation. The paper also provides guidance for other interested parties in ECN spray research. Based on this experience, we offer the following recommendations for additional specification and control of Spray A operation:

• Ambient gas density, rather than ambient gas pressure, should be maintained when switching between reacting and non-reacting Spray A experiments. Momentum transfer between the spray and ambient, which ultimately affects mixing, is expected to be best-matched when controlling ambient gas density. Ambient gas pressure cannot be matched because of varying molecular weights (see Table 3). The Spray A ambient density is 22.8 kg/m^3, producing ambient pressures that are *near*, but not exactly, 6 MPa.

• Until further information comes forth about the actual fuel temperature, the *steady-state* injector nozzle tip temperature shall be 90°C. As tip heat up transients will be different at each facility, we feel this is the best way to maintain uniformity of upstream fuel and injector components. Further experimental and modeling efforts are encouraged to understand the actual wall temperature of the nozzle sac and orifice, which can then be supplied as an additional boundary condition.

• The recommended method for steady-state injector nozzle tip temperature is a dummy injector equipped with a thermocouple probe positioned in the sac volume. The fuel temperature for Spray A is also specified within the sac volume, and this method avoids problematic measurements of temperature by thermocouples outside of the nozzle that can be affected by contact and conduction errors. Further measurements of the nozzle tip surface temperature and internal wall boundary conditions are encouraged to provide precise information of the steady-state and transient temperature distribution of the nozzle.

• Mie-scatter and schlieren visualization are recommended to characterize the global behavior of the fuel spray, prior to more detailed experimentation of the spray.

• Rate of injection information should be obtained with the injector control solenoid, as well as the injector tip, controlled to the same temperature as that used in actual spray visualization experiments. Ideally, these measurements could be made with the injector mounted in the same chamber where spray visualization is performed. If rate of injection information is unavailable, the injection duration hold current time should be adjusted while performing Mie-scatter visualization until the maximum liquid penetration at the end of injection matches the Sandia result given in Fig. 21. The liquid length recedes back towards the injector shortly after 1500 μs, the specified injection duration of Spray A. This data will be available on the ECN website. We provide this recommendation because rate of injection (Fig. 9) was performed using the spray-chamber setup at Sandia.

REFERENCES

1. Vishwanathan, G. and Reitz, R.D., "Numerical Predictions of Diesel Flame Lift-off Length and Soot Distributions under Low Temperature Combustion Conditions," SAE Technical Paper 2008-01-1331, 2008, doi:10.4271/2008-01-1331.

2. Campbell, J.W., Gosman, A.D., and Hardy, G., "Analysis of Premix Flame and Lift-Off in Diesel Spray Combustion using Multi-Dimensional CFD," *SAE Int. J. Engines* **1**(1): 571-590, 2008, doi:10.4271/2008-01-0968.

3. Kärrholm, F.P., Tao, F., and Nordin, N., "Three-Dimensional Simulation of Diesel Spray Ignition and Flame Lift-Off Using OpenFOAM and KIVA-3V CFD Codes," SAE Technical Paper 2008-01-0961, 2008, doi: 10.4271/2008-01-0961.

4. D'Errico, G., Ettorre, D., and Lucchini, T., "Simplified and Detailed Chemistry Modeling of Constant-Volume Diesel Combustion Experiments," *SAE Int. J. Fuels Lubr.* **1**(1):452-465, 2008, doi:10.4271/2008-01-0954.

5. d'Errico, G., Lucchini, T., Montenegro, G., Onarati, A., and Etorre, D., "Fundamental and applied studies of detailed chemistry based models for diesel combustion," THIESEL 2008, Valencia, Spain.

6. Lucchini, T., D'Errico, G., Etorre, D., and Ferrari, G., "Numerical Investigation of Non-Reacting and Reacting

Diesel Sprays in Constant-Volume Vessels," *SAE Int. J. Fuels Lubr.* **2**(1):966-975, 2009, doi:10.4271/2009-01-1971.

7. Vishwanathan, G. and Reitz, R., "Modeling soot formation using reduced polycyclic aromatic hydrocarbon chemistry in n-heptane lifted flames with application to low temperature combustion," J. of Engineering for Gas Turbines and Power, pp. 032801, 2009.

8. Abraham, J. and Pickett, L.M., "Computed and Measured Fuel Vapor Distribution in a Diesel Spray," Atomization and Sprays 20:241-250, 2010.

9. Turbulent Nonpremixed Flame Workshop. <http://www.ca.sandia.gov/TNF/abstract.html>.

10. Engine Combustion Network data archive. <http://www.sandia.gov/ECN/>.

11. JetSurF - A Jet Surrogate Fuel Model. <http://melchior.usc.edu/JetSurF/>.

12. Lawrence Livermore National Laboratory, Physical and Life Sciences Directive. <https://www-pls.llnl.gov/?url=science_and_technology-chemistry-combustion-mechanisms>.

13. Baert, R.S.G., Frijters, P.J.M., Somers, B., Luijten, C.C.M. et al., "Design and Operation of a High Pressure, High Temperature Cell for HD Diesel Spray Diagnostics: Guidelines and Results," SAE Technical Paper 2009-01-0649, 2009, doi:10.4271/2009-01-0649.

14. Siebers, D.L., "Liquid-Phase Fuel Penetration in Diesel Sprays," SAE Technical Paper 980809, 1998, doi:10.4271/980809.

15. Miles, P.C. and Gouldin, F.C., "Determination of the time constant of fine-wire thermocouples for compensated temperature measurements in premixed turbulent flames," Combust. Sci. Tech. 83:1-19, 1992.

16. Petit, C., Gajan, P., Lecordier, J.C., and Paranthoen, P., "Frequency response of fine-wire thermocouple", J. Phys. E: Sci. Instrum., 15:760, 1982.

17. Heitor, M. V. and Moreira, A.L.N., "Thermocouple and sample probes for combustion studies," Prog. Energy Combust. Sci. 19:259-278, 1993.

18. Dupont, A., Paranthoen, P., Lecordier, J.C. and Gajan, P., "Influence of temperature on the frequency response of fine-wire thermocouples over the range (300 K-800 K) in airflows", J. Phys. E: Sci. Instrum., 17:808-812, 1984.

19. Paranthoen, P., Petit, C. and Lecordier, J.C., "The effect of the thermal prong-wire interaction on the response of a cold wire in gaseous flows (air, argon and helium)", J. Fluid Mech., 124:457-473, 1982.

20. Malbec, L.-M. and Bruneaux, G., "Study of Air Entrainment of Multi-hole Diesel Injection by Particle Image Velocimetry - Effect of Neighboring Jets Interaction and Transient Behavior After End of Injection," *SAE Int. J. Engines* **3**(1):107-123, 2010, doi:10.4271/2010-01-0342.

21. Siebers, D.L. "Scaling Liquid-Phase Fuel Penetration in Diesel Sprays Based on Mixing-Limited Vaporization," SAE Technical Paper 1999-01-0528, 1999, doi:10.4271/1999-01-0528.

22. Giannadakis, E., Gavaises, M., and Theodorakakos, A., "The Influence of Variable Fuel Properties in High-Pressure Diesel Injectors," SAE Technical Paper 2009-01-0832, 2009, doi:10.4271/2009-01-0832.

23. Allison, S.W. and Gillies, G.T. "Remote thermometry with thermographic phosphors: Instrumentation and applications", Review of Scientific Instruments 68(7): 2615-2650, 1997.

24. Kashdan, J.T. and Thirouard, B., "A Comparison of Combustion and Emissions Behaviour in Optical and Metal Single-Cylinder Diesel Engines," *SAE Int. J. Engines* **2**(1): 1857-1872, 2009, doi:10.4271/2009-01-1963.

25. Pickett, L.M., Kook, S., and Williams, T.C., "Visualization of Diesel Spray Penetration, Cool-Flame, Ignition, High-Temperature Combustion, and Soot Formation Using High-Speed Imaging," *SAE Int. J. Engines* 2(1): 439-459, 2009, doi:10.4271/2009-01-0658.

26. Settles, G.S., *Schlieren and Shadowgraph Techniques*, Springer-Verlag, 2001.

27. Naber, J.D. and Siebers, D.L., "Effects of Gas Density and Vaporization on Penetration and Dispersion of Diesel Sprays," SAE Technical Paper 960034, 1996, doi:10.4271/960034.

28. Kook, S., Pickett, L.M., and Musculus, M.P.B., "Influence of Diesel Injection Parameters on End-of-Injection Liquid Length Recession," *SAE Int. J. Engines* **2**(1): 1194-1210, 2009, doi:10.4271/2009-01-1356.

29. Desantes, J.M., Pastor, J.V., Garcia-Oliver, J.M., and Pastor, J.M., "A 1D model for the description of mixing-controlled reacting diesel sprays," Combust. Flame 156:234-249, 2009.

30. Siebers, D. and Higgins, B., "Flame Lift-Off on Direct-Injection Diesel Sprays Under Quiescent Conditions," SAE Technical Paper 2001-01-0530, 2001, doi:10.4271/2001-01-0530.

31. Pickett, L.M., Siebers, D.L., and Idicheria, C.A., "Relationship Between Ignition Processes and the Lift-Off Length of Diesel Fuel Jets," SAE Technical Paper 2005-01-3843, 2005, doi:10.4271/2005-01-3843.

32. Bruneaux, G., "Combustion structure of free and wall-impinging diesel jets by simultaneous laser-induced fluorescence of formaldehyde, poly-aromatic hydrocarbons, and hydroxides," Int. J. Engine Research 9:249-265, 2008.

33. Pickett, L.M., Kook, S., Persson, H., and Andersson, O., "Diesel fuel jet lift-off stabilization in the presence of laser-induced plasma ignition," Proc. Combust. Inst. 32:2793-2800, 2009.

34. Higgins, B. and Siebers, D., "Measurement of the Flame Lift-Off Location on DI Diesel Sprays Using OH Chemiluminescence," SAE Technical Paper 2001-01-0918, 2001, doi:10.4271/2001-01-0918.

35. Musculus, M.P.B., Lachaux, T., Pickett, L.M., and Idicheria, C.A., "End-of-Injection Over-Mixing and Unburned Hydrocarbon Emissions in Low-Temperature-Combustion Diesel Engines," SAE Technical Paper 2007-01-0907, 2007, doi:10.4271/2007-01-0907.

36. Pickett, L.M. and Siebers, D.L., "Soot in diesel fuel jets: effects of ambient temperature, ambient density, and injection pressure," Combust. Flame 138:114-135, 2004.

CONTACT INFORMATION

Lyle M. Pickett
LMPicke@sandia.gov

Caroline L. Genzale
clgenza@sandia.gov

Gilles Bruneaux
gilles.bruneaux@ifp.fr

Louis-Marie Malbec
louis-marie.malbec@ifp.fr

ACKNOWLEDGMENTS

Support for this research was provided by the U.S. Department of Energy, Office of Vehicle Technologies and the French Ministry of Ecology, Energy, Sustainable Development and Sea (project CANDLE). The research at Sandia National Laboratories was performed at the Combustion Research Facility, Livermore, California. Sandia is a multiprogram laboratory operated by Sandia Corporation, a Lockheed Martin Company, for the United States Department of Energy's National Nuclear Security Administration under contract DE-AC04-94AL85000.